ENHANCEMENT OF POOL BOILING HEAT TRANSFER USING THERMALLY-CONDUCTIVE MICROPOROUS COATING TECHNIQUES

by

JOO HAN KIM

Presented to the Faculty of the Graduate School of
The University of Texas at Arlington in Partial Fulfillment
of the Requirements
for the Degree of

DOCTOR OF PHILOSOPHY

THE UNIVERSITY OF TEXAS AT ARLINGTON

December 2006

Copyright © by Joo Han Kim 2006

All Rights Reserved

ACKNOWLEDGEMENTS

I would like to express my most sincere appreciation to Dr. Seung Mun You who served as my advisor and counselor through my doctoral research. His dedication to high ethical standards and great challenge has been a cornerstone for my life as an engineer. I also would like to acknowledge the friendship and technical support of my fellow lab members.

Most of all, I gratefully acknowledge the support and encouragement of my wife, Youn Mi Kim, who continuously have been supporting my study and life. Finally, I want to thank my children, Lina and Janet, for their existence during this effort. Without my family, this accomplishment would not have been possible. I dedicate this thesis to them.

September 30, 2006

ABSTRACT

ENHANCEMENT OF POOL BOILING HEAT TRANSFER USING THERMALLY-CONDUCTIVE MICROPOROUS COATING TECHNIQUES

Publication No. ______

Joo Han Kim, PhD.

The University of Texas at Arlington, 2006

Supervising Professor: Seung Mun You

The present research is an experimental study of the enhancement of boiling heat transfer using microporous coating techniques. The current research is divided into four major phases. During the first phase, the effects of different metal particle sizes in the coating compound for thermally non-conductive microporous coating on pool boiling performance of refrigerants and water are investigated. The test surfaces were solid copper blocks with 1-cm² base at atmospheric pressure in saturated FC-72, R-123, and water. Results showed that the surface treatment by non-conductive microporous coating significantly enhanced both nucleate boiling and critical heat flux of FC-72 and R-123. However, the enhancement of boiling performance for water was merely shown.

In the second phase, thermally conductive microporous coatings to enhance boiling performance of water were developed. The first phase motivated efforts to fabricate microporous coatings with conducting binder options. The second phase was stemmed from an effort to combine the advantages of both a mixture batch type (inexpensive & easy process) and sintering/machining method (low thermal resistance of conduction). Two categories of surface treatment processes were considered in the current research. The first can be achieved by a chemical process, Multi-Staged Electroplating (MSE), which uses electricity in a chemical bath to deposit a microporous structure on the surface. The second is a soldering process, Multi-Temperature Soldering Process (MTSP), which binds the metal particles to generate optimum microporous cavities. Scanning Electron Microscope (SEM) and optical microscope images were obtained for thermally conductive microporous coated surfaces.

During the third phase, the pool boiling performance of developed MSE and MTSP from second phase was confirmed for water. Results showed that the MSE and MTSP augmented the boiling performance not only for refrigerants but also for water significantly compared to non-conductive microporous coatings. Further investigation for possible future industrial applications of microporous coatings, such as indirect cooling for electronic chips, nanofluids for high power generation industries, and freezing problem of water, were conducted in the final phase.

TABLE OF CONTENTS

Chapter

Appendix

LIST OF ILLUSTRATIONS

LIST OF TABLES

NOMENCLATURE

c_p	specific heat capacity, [J/kg-K]
d	diameter of bubbles [m]
g	gravitational acceleration, [m/s²]
h_{lv}	latent heat of vaporization, [J/kg]
Nu	Nusselt number
P_l	absolute liquid pressure, [kPa]
Pr	Prandtl number
q''	heat flux, [W/cm²]
Ra	Rayleigh number
T	temperature, [°C]
V	volume of bubbles [m^3]

Greek Symbols

ΔT_{sat}	wall superheat, T_w-$T_{sat}(P_{sys})$
ρ	density, [kg/m³]
σ	surface tension, [N/m]

Subscripts

b	bubble
bulk	bulk quantity
CHF	critical heat flux

crit	critical
inc	incipience
l	saturated liquid
LH	latent heat
max	maximum
sat	saturated conditions
v	saturated vapor
w	heater surface (wall)
z	CHF prediction of Zuber

CHAPTER 1

INTRODUCTION

1.1 Two-phase Cooling

The restless development of high-speed microelectronic chip designs in the electronic devices has been creating the cooling requirement of higher heat dissipation than conventional cooling devices (forced convection by single-phase) can handle. Many different cooling schemes have been studied, and the utilization of nucleate boiling in cooling schemes (two-phase, liquid to vapor) is a viable alternative that has received much attention recently.

During the last several decades, numerous research [1,2,3] has been performed on the boiling phenomena as a mode of heat transfer. Based upon previous efforts to understand the fundamentals of boiling heat transfer, many researchers have recently commenced studies of the application of the boiling heat transfer to minimize the surface temperature of heated objects at given heat loads, and to maximize the dissipation heat energy at given operating temperature.

Two-phase cooling (liquid to vapor) for electronics can be categorized as indirect or direct. For indirect cooling, the coolants do not contact the microelectronic chips whereas direct cooling involves direct contact of the coolants with the microelectronic chips. Figure A.1 illustrates two-phase cooling modules that utilize direct and indirect pool boiling. In figure A.1, a heat source is immersed in the coolant directly to boil for a direct cooling unit. The vapor is then condensed back to bulk liquid utilizing an external cooling device such as a coldplate or fan/heat sink assembly. For indirect cooling unit, a heat source is attached to the bottom plate of cooling unit from outside and boiling heat transfer occurs inside of cooling module filled with a coolant after heat spreading.

1.2 Pool Boiling Heat Transfer

This section will briefly review the pool boiling process and the mechanism in a pool of motionless liquid. A typical boiling curve is illustrated in figure A.2. The vertical axis corresponds to the heat flux, q" (units of heat energy transfer rate per unit surface area, W/cm^2), dissipated from the heated surface. The horizontal axis identifies the temperature difference between the heated surface and the bulk liquid. Three main regions can be identified on the curve; the natural convection region, nucleate boiling region, and a second transition region near the CHF. Throughout the natural convection region, heat is transferred to the bulk liquid via density gradient driven motion caused by temperature difference between the heated surface and liquid. In figure A.2, q''_{inc} is the incipience heat flux point where the first bubbles are generated from the heated surface. In the nucleate boiling region, there are two distinct regimes of bubble behavior. The first one is the isolated bubble regime where discrete bubbles depart from the heated surface. The second region occurs when the number of active sites becomes so dense that adjacent bubbles merge together, which forms vapor slugs and columns. The CHF (critical heat flux) followed by the departure of nucleate boiling regime and leads to the film boiling regime. The CHF is the limiting factor for real applications due to the significant increase in temperature.

1.2.1 Natural Convection

Natural convection is initiated as soon as the surface temperature increases above the bulk liquid temperature. In natural convection, fluid motion is due solely to local buoyancy differences caused by the presence of the hot or cold body's surface. For example, most fluids near a hot wall will experience a decrease in density, and an upward near-wall motion will be induced. Natural convection velocities are relatively gentle and the resultant wall heat flux will generally be less than in forced motion. Kuehn and Goldstein [4] developed a natural convection correlation using a conduction boundary layer model on a horizontal cylinder.

$$\overline{Nu}_D = \frac{2}{\ln\left[1 + \dfrac{2}{\left[\left(0.518 Ra_D^{1/4}\left[1 + \left(\dfrac{0.559}{P_r}\right)^{3/5}\right]^{-5/12}\right)^{15} + \left(0.1 Ra_D^{1/3}\right)^{15}\right]^{1/15}}\right]}$$

Goldstein et al. [5] developed a correlation for external natural convection from upward and downward facing horizontally oriented flat surface.

$$\overline{Nu}_L = C \cdot Ra_L^{\;X}$$

The constants C and X are related to the Rayleigh number and surface inclination. According to their study, C=0.54 and X=0.25 for upward facing laminar condition while C=0.15 and X=0.333 for turbulent condition. They further improved the accuracy of their correlation by using a modified characteristic length defined as the ratio of the heated surface area to its perimeter.

1.2.2 Boiling Incipience

Boiling incipience (formation of initial vapor bubble) occurs due to the excessively superheated liquid near the heated surface after natural convection through the heterogeneous nucleation process. During this process, small amounts of non-condensable gases or vapor are trapped in micro-sized cavities on the heated surface by the advancing fluid front. These trapped gases/vapor pockets act as embryod in the formation of boiling bubbles. As heat is applied to the surface, a superheated liquid layer is generated and this superheated layer drives fluid vaporization at the embryonic bubble vapor/liquid interface. If sufficient heat is applied, the embryonic bubble will grow until it departs and a new bubble will grow in its place. The amount of liquid superheat required to initiate nucleate boiling depends on the fluid properties and the embryonic bubble bubble size. Smaller embryonic bubbles require larger superheats to initiate bubble growth due to increased bubble vapor pressure. The pressure inside a bubble formed on the heated surface can be estimated as following.

$$P_b - P_l = \frac{2\sigma}{r_b}$$

where P_b is the bubble pressure and is equal to the sum of the partial pressures of vapor and gas within the bubble. P_l is the liquid pressure and for saturation conditions is equal to the saturation pressure at the bulk liquid temperature. σ and r_b are the surface tension and the bubble radius, respectively.

Griffith and Wallis [6] were the first to construct a relation to predict the superheat required to initiate boiling. The relation was derived by conducting an equilibrium analysis on the liquid-vapor/gas interface of a bubble resting in a conical cavity on a solid surface. Bar-Cohen and Simon [7] pointed out that there is a variation in the incipience mechanism between highly and non-highly wetting liquids. This is attributed to difference in surface tension, contact angle, dissolved gas, and the ability of the highly-wetting liquids to effectively flood surface cavities. They suggested a correlation relating the vapor pressure required to activate a bubble embryo to the embryonic bubble radius and surface tension.

$$P_{sat}(T_w) - P_{sat}(T_{bulk}) = \frac{2\sigma(T_w)}{r_b}$$

where:

$$\sigma_{FC-72} = 0.042705\left(1 - \frac{T_w}{T_{crit}}\right)^{1.2532} \qquad \text{for FC-72}$$

1.2.3 Nucleate Boiling

The nucleate boiling region can be divided into two regimes; isolated bubble and vapor mushroom regime. On a nucleate boiling surface, the total heat dissipation is divided into four modes of heat transfer: latent, micro-convection, natural convection, and Marangoni flow. Latent heat transfer takes place when liquid vaporizes and leaves the heated surface. Micro-convection results from sensible heat energy removed by entrainment of the superheated liquid in the departing bubble’s wake. Natural convection is the sensible energy transport removed from non-boiling portions of the heated surface due to density gradients. Marangoni flow is caused by the surface tension gradient while the bubble is still attached to the surface. Latent and micro-convection heat transfer are generally considered as primary heat transfer mechanisms in fully developed (vapor mushroom regime) and saturated nucleate boiling. Marangoni flow effects can be neglected if the liquid is fully saturated, and natural convection can be ignored when bubbles are fully developed on a heated surface.

Rohsenow [8] proposed a model correlating the heat flux to the wall superheat during nucleate boiling for both the isolated bubble regime and vapor mushroom regime. His correlation was based on an assumption that bubble agitation disrupts the stagnant liquid film and transports superheated liquid away from the surface (micro-convection).

$$\frac{q''}{\mu_l h_{lv}}\left[\frac{\sigma}{g(\rho_l-\rho_v)}\right]^{1/2}=\left(\frac{1}{C_{sf}}\right)^{1/r}\Pr_l^{-s/r}\left[\frac{c_{pl}\left(T_w-T_{sat}(P_l)\right)}{h_{lv}}\right]^{1/r}$$

C_{sf} is a constant value for different liquid-surface combinations from experiments. Originally, values of r = 0.33 and s = 1.7 were suggested for this correlation. Rohsenow subsequently recommended that s be changed to 1.0 for water. All properties are obtained at the saturation temperature.

1.2.4 Critical Heat Flux (CHF)

The CHF point represents the maximum heat dissipation rate that can endure in the nucleate boiling region. Models to describe the occurrence of CHF are divided into two opposite groups. One emphasizes the breakup of the vapor escape route from the heated surface due to hydrodynamic instabilities. The other accentuates the restriction of cold bulk liquid inflow to the heated surface due to the vapor blanketing phenomenon, which shows a growing agreement with experimental data. According to the hydrodynamic CHF model, two phenomena govern the mechanism causing CHF; Taylor instability and Helmholtz instability. Lienhard [9] described Helmholtz instability by using a flag extended in a wind having arbitrary velocity. The flag exists in a constant state of collapse due to the differential pressures associated with the low and high air velocities on either side of the flag. The end view of the flag represents a wavy type motion where a length equal to the period of the wave is referred to as the Helmholtz wavelength, λ_H.

In 1959, Zuber [10] developed a hydrodynamic prediction of the CHF, which is the theory originally developed by Kutateladze [11] in 1948, on an infinite horizontal flat plate. The model refined by Zuber [10] from Helmholtz-instability has been accepted as a method of CHF prediction for flat horizontal surfaces. Fluid properties affecting CHF values consist of heat of vaporization, densities of vapor and liquid, and surface tension according to the prediction. The correlation is given as:

$$q''_{\max,z} \equiv 0.131 \rho_v^{1/2} h_{lv} \sqrt[4]{g\sigma\left(\rho_l - \rho_v\right)}$$

From experimental data and new theoretical models, Lienhard and Dhir [12] corrected the Zuber's correlation as:

$$q''_{\max,z} \equiv 0.149 \rho_v^{1/2} h_{lv} \sqrt[4]{g\sigma(\rho_l - \rho_v)}$$

This correlation predicts the CHF on a flat surface 13.7% higher than Zuber's correlation.

1.3 Enhancement of Boiling Heat Transfer

Various surface enhancement techniques as a passive method have been previously investigated and commercialized by researchers to maximize boiling heat transfer performance by augmenting the nucleate boiling heat transfer coefficient and extending the critical heat flux (CHF). One of the earliest methods used to produce an enhanced boiling surface was to roughen a plain surface using sandpaper or some other abrasive. Kurihara and Myers [13] showed that the nucleate boiling enhancement by roughening was the result of an increased active nucleation site density. The increased number of nucleation sites may enhance the heat transfer by providing more convection heat transfer from increased bubble agitation and/or increased latent heat transport.

With regard to CHF, the effects of surface roughening are much less clear. Many researchers have reported that CHF was independent of surface roughness (Berenson [14], Nishio and Chandratilleke [15]). Alternatively, Ramilison et al. [16], using data for various fluids, showed that surface roughness actually influence the CHF. The porous metallic coatings were also found to significantly enhance CHF. Polezhaev and Kovalev [17] suggested that the enhancement was due to decreased vapor jet spacing (increased vapor jet velocity) while Tehver [18] proposed that the enhancement was due to increased macrolayer evaporation time.

Griffith and Wallis [19] showed that the geometry of the micro-cavity containing trapped vapor/gases was directly related to the bubble nucleation process. Most notably, they found that re-entrant type cavities were stable, easily activated boiling sites. From their study (as well as others), numerous enhancement techniques utilizing re-entrant type cavities or grooves have been developed. Since their first development, porous metallic coatings have received much attention. Formed by bonding metal particles with diameters of 44-1000 μm to a base surface (coating thickness ranges from 250 to 2000 μm), porous metallic coatings have been shown to significantly enhance nucleate boiling heat transfer performance. Thome [20] concluded that the primary enhancement mechanisms for re-entrant type enhanced surfaces were: enhanced nucleation from the larger embryonic bubbles, increased thin film evaporation due to the large internal surface area of the porous structure, and two-phase convection within the porous structure. From their endeavors, many commercial enhanced surfaces utilizing re-entrant type cavities or grooves have been developed, such as Furukawa's ECR-40, Union Carbides's High-Flux, and Hitachi's Thermoexcel.

A relatively new method for surface enhancement is microporous coating introduced by O'Connor and You [21], refined by Chang and You [22,23] and patented by You and O'Connor [24]. The coating is a surface treatment technique used to increase vapor/gas entrapment volume and active nucleation site density by forming a porous structure of 1-20 μm particles with cavities of about 0.1-1 μm and bonded together with epoxy. The microporous coating is different from conventional metallic porous coatings because: a) it uses much smaller particles, b) the coating is much thinner (~50 μm), and c) the resulting porous structure has a low effective thermal conductivity (estimated at approximately 0.95 W/m-K by O'Connor and You [21]). The microporous coating has already shown to significantly enhance the pool nucleate boiling heat transfer performance and critical heat flux (CHF) over plain surfaces in highly-wetting fluids [25,26]. Chang and You [23] attributed the enhancement of nucleate boiling heat transfer performance to increased active nucleation site density, however, the enhancement mechanisms of the coating have not been thoroughly investigated. Kim et al. [27] showed that the microporous coating augments nucleate boiling performance through increased latent heat transfer in the low heat flux region and through increased micro-convection heat transfer in the high heat flux region. The critical heat flux for the microporous coated surface is significantly enhanced over the plain surface due to decreased latent heat transfer (decreased vapor generation rate) and/or increased hydrodynamic stability from increased vapor inertia; both of which are a direct result of increased nucleation site density.

Figure A.3 shows that the enhanced surface with numerous active nucleation sites generates smaller sizes of bubbles with higher departure frequencies resulting in comparatively thin superheated liquid layer near the heated surface over the plain surface. The consistent contributing factor to nucleate boiling enhancement using the microporous coating is the increase in bubble departure frequency. The increase in departure frequency is probably due to an increase in both single site frequency and nucleation site density. The occurrence of either of these phenomena would have lowered the heater surface temperature by reducing the average temperature within the superheated liquid layer that surrounds the heated surface. As seen in figure A.3, a reduction in waiting time would occur during the bubble growth and departure cycle if a significant increase in single-site frequency occurred. A reduction in waiting time would lead directly to lower surface temperature. If a rise in the number of active nucleation sites occurred, the combined sum of the individual bubble influence areas (the heater surface area affected by micro-convection due to departing bubbles) would increase, even though the resulting bubble diameters are smaller. An increase in area of influence along with an rise in bubble frequency enables the removal of larger amount of superheated liquid and inhibits the growth of the superheated liquid layer, thus reducing wall superheat.

1.4 Objectives

The objective of the present research is to develop enhanced boiling surfaces by generating microporous structures for refrigerants and water. The effects of different metal particle sizes in coating compound for thermally non-conductive microporous coating on pool boiling performance of refrigerants and water are first investigated at atmospheric pressure in saturated FC-72, R-123, and water to understand the limitations of microporous coating. The thermally conductive microporous coatings (MSE and MTSP) are then constructed, and their SEM (Scanning Electron Microscope) and optical microscope images are presented to visualize the microporous cavities. Pool boiling testing of MSE and MTSP coatings is performed in pools of R-123, FC-72, and water at atmospheric pressure. For MTSP coatings, boiling test is additionally conducted in a pool of methanol at atmospheric pressure.

Further research was conducted for possible future industrial applications of microporous coatings. The results of this study are meant to aid in the development of future electronics cooling schemes involving boiling. The MTSP coating was employed for a double-enhancement study for an indirect cooling system that uses spreaders (8 x 8 cm, copper) with varying thickness (1.5, 2.5, 3.5, 5.5, and 6.5 mm). The tests were executed in saturated FC-72 at 35, 45, and 55˚C saturation and water at 45, 55, and 60 ˚C saturation. The MSE coating was selected and tested in a nanofluid at 60 ˚C saturation to investigate the effect of microporous coatings on CHF mechanism. Furthermore, Propylene Glycol (PG) was added into water to make antifreeze (20, 30, 40, and 50% volume) to investigate the effects of MSE and MTSP coatings on anti-freezing liquids at 60 ˚C saturation. Finally, the spreaders (1.5, 3.5, and 5.5 mm thickness) with MTSP coating were selected and tested in 50% antifreeze at 45, 55, and 65 ˚C saturation and compared with results in water.

CHAPTER 2

EXPERIMENTAL APPARATI AND PROCEDURES

This chapter will identify test section designs and heaters used in the present research as well as data acquisition, test procedures, and uncertainty analysis.

2.1 Pool Boiling Test Facility

The experimental setup for this study is shown in figure A.4. The test apparatus was constructed mostly of aluminum to ensure chemical compatibility with working fluids and to reduce total weight. Reinforced glasses were equipped at the front and rear sides of the test section for the view ports. For rapid heating and stirring purpose, two cartridge heaters were immersed below a test heater. The silicon rubber heaters were attached on two sides and on the bottom of the vessel to accurately maintain the steady condition of the boiling fluid. The internal pressure was measured with an absolute pressure transducer, DRUCK PTX-1400, which has a range of 0～2.5 bar and an accuracy of 0.25% in full scale. Copper-Constantan thermocouples (T-type) were placed within the test vessel to measure vapor and bulk liquid temperatures.

An external, water-cooled condenser was used throughout the testing to prevent the loss of test liquid. Atmospheric pressure was maintained by venting the vessel to ambient. A valve was placed between the external condenser and the test section to execute the boiling test at different saturation pressures.

2.2 Data Acquisition System and Instrumentation

The pool boiling test facilities used the same data acquisition setup as follows: a computer controllable DC power supply (HP 6030A, 0-200 V, 0-17 A, 1,000 W) connected in series with a shunt resistor (Crompton, Model 871-92UU-MTGB) and the test heater. The shunt resistor, rated at 100 mV and 10 A, was used to determine the current in the electric circuit. Direct current was supplied to the heating element by the DC power supply. The measured voltage drop across the test heater was used to calculate the heat flux applied to the test heater. An HP 3852A Data Acquisition/Control Unit was used for all temperature, pressure, and voltage measurements. An IBM compatible PC was used to control the data acquisition unit, multimeter and power supply via an IEEE-488 (GPIB) interface. HP-Basic for Windows was used to create and run the testing control programs, which are included in Appendix C for the boiling test. A digital video camera and a halogen lighting system were used to take sample boiling pictures.

2.3 Test Heaters

The design and fabrication of the test heaters are discussed in this chapter.

2.3.1 Fabrication

The test heaters for current research were manufactured as shown in figures A.5 and A.6. A commercially available, 20-ohm square resistor, was used as the heating element. A copper block was soldered to the heating element and a clear epoxy was filled around the copper block and the resistor to provide insulation and to generate a flush-mounted heating surface. In order to obtain the surface temperature, the T-type thermocouple was inserted at 1.5 mm below the upper surface of the copper block. From the measured temperatures, the wall temperature was then calculated assuming one-dimensional heat conduction through the copper block.

2.3.2 Plain Surface, 1 x 1 cm

The assembly for 1 x 1 x 0.3 cm heater was fabricated as shown in figure A.5. A 20-ohm square resistor obtained from Component General Co. was used for the heating element. The copper block was soldered with soldering wire (melting point, 180 ˚C) to the heating element to minimize thermal contact resistance between the heating element and copper block. The copper block soldered into heating element was mounted on the Lexan plate and surrounded with 1838 L B/A epoxy by 3M. and cured for 24 hours at room temperature to generate a flush-mounted heating surface and to secure the heater assembly, thermocouple, and electrical leads.

2.3.3 Spreading heater with MTSP coating

This heater configuration shown in figure A.6 is constructed to investigate the effects of spreader thickness on indirect cooling schemes. The copper body of the 8 x 8 cm (spreader) with varying thickness and 1 x 1 cm with 0.3 cm thickness copper block underneath a spreader were machined as a single component to eliminate possible measurement errors due to inconsistent contact resistance between the spreader and 1 x 1 cm with 0.3 cm thickness copper block if jointed together. Power leads and thermocouple line were fed through holes in the bottom of the frame, then the copper/heater assembly was mounted in the Lexan frame with epoxy, generating a spreaded heating surface.

2.4 Test Procedures

The test fluids, R-123, FC-72, de-ionized and distilled water, and methanol (only for MTSP coating) were prepared for current study. Selected thermal properties for each liquid are listed in Table B.1-4. Prior to all testing, the test chamber was heated to the test liquid's saturation temperature at atmospheric pressure using band and cartridge heaters. Once reached at its saturation temperature, the test liquid was boiled vigorously for at least one hour to remove dissolved non-condensable gases.

The fluid level for the saturation cases was maintained in the test chamber at approximately 15 cm above the test surface. After degassing, the external condenser was turned off. With the system still open to ambient, some of the test liquid was allowed to escape in order to push out any trapped air at the top of the condenser. After about 15 minutes, the valve at the top of the external condenser was closed. The measured temperature and pressure readings within the test chamber were monitored against the liquid's saturation curve to ensure that all non-condensables had been removed. The desired system pressure was then established by controlling the bulk fluid temperature using the external cooling fan and the temperature controller interfaced with the band heaters. After the desired pressure was obtained and stabilized, testing began. For the saturated tests at atmospheric pressure, a simpler procedure was employed. Instead of the closed system approach above, the external condensers was left on and open to ambient during the entire test period.

After the proper fluid conditions were obtained and stabilized, two consecutive boiling curves were generated for each test surface. Identical boiling curves for each surface assured the consistency and repeatability of the data. There was a two-hour delay between runs to allow the heater and test section to return to steady-state. Heat flux was controlled by voltage input. After each voltage change (heat-flux increment), a 15-second delay was imposed before initiating data acquisition. After the delay, the computer repeatedly collected and averaged 125 base surface temperature measurements over 15 seconds until the temperature difference between two consecutive averaged temperature measurements for all thermocouples was less than 0.2 ˚C. The test heater at this point was assumed to be at steady-state. After reaching steady state, the heater surface and bulk fluid temperatures were measured and the heat flux was calculated. For heat flux values greater than ~80% of CHF, instantaneous surface temperature was monitored for 45 seconds after each increment to prevent heater burnout. Each instantaneous surface temperature measurement was compared with the previous steady-state surface temperature measurement. If a temperature difference larger than 20 ˚C was detected, CHF was assumed and the power shut off to protect the test heater. The CHF value was computed as the steady-state heat flux value just prior to power supply shutdown plus half of the increment. To avoid heater failure, the maximum steady-state base temperature of the heaters was limited to 130 ºC. Tables of the experimental pool boiling data used in this study are included in Appendix B.

2.5 Consecutive Photo Method

To conduct the boiling mechanism analysis for the nanofluid in Chapter 5, the “Consecutive-photo method” introduced by Ammerman et al. [28] was employed for this study. A high-speed camera captured the images of the domain of interest including bubbles departing from a heated platinum wire during the boiling process. The camera was connected to a personal computer to archive and digitize the images of the bubbles. To obtain images of the bubbles departing from a wire during boiling process, a high-speed camera was used during the test. The camera was connected to a personal computer to digitize the images and to directly download the images into the computer's memory slots. The frame speed was set to 240 frames per second and a shutter speed was assigned at 1/10,000 of a second. The wire heater was illuminated from the back with 150 Watts halogen lamp. A tracing paper was placed on the back of the vessel to diffuse light from the lamp for highly accurate measurement of the bubble's size. According to Lunde and Perkins [29], bubbles diameter could be underestimated and inaccurate if a perfect diffuser was used.

To get a length scale for the bubbles, a ball bearing of known diameter (0.238 cm) was glued onto a clear plastic ruler and the ruler was positioned next to the wire heater. To correctly define the edge of a bubble, before taking pictures of the bubbles leaving the wire, several pictures of the ball bearing attached to the ruler; each of these pictures was taken with five slightly different light intensity settings by changing the f-stop on the camera lens. Those calibration images were compared with the pictures of bubbles during the experiment, and the best calibration picture was determined by the background gray level (the background is anyplace where there are no bubbles shown). The image processing software (Global Lab Image) was used to find the edge of the ball bearing in the calibration photo. The ruler in this image was used to get a length scale, then the image processor located the edge and showed the ball bearing's diameter value. This image process was repeated by modifying the gray level, which defines the edge of a bubble until the software showed that the diameter of the ball bearing is 0.2381 cm. To increase the accuracy of measuring the bubbles size, the lens magnification was set proportionally so that the bubbles departing from different wires were approximately same range of size.

2.6 Uncertainty Analysis

In order to establish the credibility of measured data, single-sample uncertainties for this study were estimated using the method of Kline and McClintock [30]. They introduced a technique for estimating the measurement uncertainty in a given empirical results which is a function of different independent measurement parameters. The uncertainty in the required experimental results can be determined by knowing the uncertainties in each of the independent measurement parameters given with specified uncertainty values.

Uncertainty in pressure measurements was estimated as ~2%. Heat flux measurement uncertainty was estimated based upon the substrate conduction losses reported by O'Connor and You [21], whose heater had a similar construction as the present one. Taking into account both measurement and substrate conduction errors, the uncertainty in heat flux (based on base area) was estimated as ~16% at 0.5 W/cm^2 and ~6.0% at 16, 80 and 120 W/cm^2. In addition, temperature measurement uncertainty was estimated considering the thermocouple calibration error, temperature correction for the embedded thermocouples, and thermocouple resolution error. The uncertainty for temperature measurement was ±0.4 ˚C.

CHAPTER 3

NON-CONDUCTIVE MICROPOROUS COATINGS

Non-conductive microporous coatings are defined as the microporous coatings that employ epoxy-type materials with low thermal conductivity to bind metal particles. Development of non-conductive microporous coatings is presented in this chapter. The boiling tests are performed in selected refrigerants (R-123 and FC-72) and water to find the optimal coating structures for specific working liquids. All boiling tests were performed with the 1x1cm test heaters in the horizontal, upward facing orientation under increasing heat flux conditions at atmospheric pressure.

3.1 ABM Microporous Coatings

ABM coatings were previously developed and patented by You and O'Connor [21,24]. The microporous coating provides a boiling enhanced surface by increasing vapor/gas entrapment and active nucleation site density with a porous structure. The coatings were named from the initial letters of their three components. ABM coating is made with **A**luminum, Devcon **B**rushable Ceramic, and **M**ethyl-Ethyl-Keytone. ABM coating is thermally non-conductive because Brushable Ceramic is an epoxy-type binder with low thermal conductivity (less than 1.0 W/mK). A mixture of the three components can be either drip-coated or spray-coated over the heater surfaces. After the carrier (Methyl-Ethyl-Keytone) evaporates, the resulting coated layer consists of microporous structures with aluminum particles and a binder (Devcon Brushable Ceramic). For current study, five different sizes of aluminum particles were selected to find the optimum metal particle size for specific working fluids.

3.1.1 Fabrication

Aluminum particles with size ranges of 3-4.5, 4.5-10, 8-12, 10-14, and 17-30 μm were prepared to fabricate the ABM coatings. Except the range of 17-30 μm (drip method must be accompanied for this size due to the small nozzle size of air brush), the spray method was used to fabricate the ABM coatings. A mixture batch of coating compounds is prepared. The spray and drip methods use the same mixing procedure, which is described below.

1) Mix a small amount of epoxy.
2) Pour epoxy into the back of a 3cc syringe then insert the plunger and remove the air. If the epoxy is sucked into the syringe, an inaccurate measurement will result.
3) Place a 30 ml vial on a mass balance and zero, then inject required amount of epoxy into the 30 ml vial.
4) Pour 10 ml of MEK into the vial and close.
5) Calculate the amount of particles needed by dividing your measured amount of epoxy by 0.32 g and then multiply by 1.5 g. This keeps the epoxy/particle ratio more accurate and repeatable.

6) Place a piece of measuring paper on the mass balance and zero. Measure out the calculated amount of Aluminum powder (about 1.5 g) and then pour it into the vial.
7) Shake vial until all of the epoxy on the bottom of the vial is gone then place in the ultrasonic bath for ~5 minute. This should sufficiently mix the "paint".

The spray method uses an Iwata HP-C airbrush to coat ABM microporous surfaces onto desired surface. The airbrush setup uses the building air supply, a filter system, a low pressure gauge (need to measure 5 psig), and the airbrush. Below is the procedure:

1) Setup the airbrush. Run a hose from the building air to the filter system, from the filter rack to the pressure gauge, and from the pressure gauge to the airbrush. The filter is needed to filter water and oils from the air supply.
2) With the airbrush on, set the supply pressure to 5 psig.
3) Prepare the heater. Mask off all but the surface to be coated.
4) Shake the coating mixture then swirl it. Pour a small amount into the airbrush cup.
5) To coat the surface, point the airbrush away from the surface and start spraying. Make sure to push the trigger all the way down and pull it fully back. (The sprayer is made for variable paint flowrate by adjusting the trigger position. However, due to the solid particles in the paint this could cause a filtering effect,

which would allow more epoxy and fewer particles through the nozzle than needed.) Then start coating the surface with slow even strokes. Spray at about 6 inches away from the surface. In addition, the surface should remain wet while spraying. Be sure to practice first and be careful not to put too thick a coating on the surface or allow it to run. Be sure to keep the coating mixed well during spraying. This can be achieved by periodically covering the nozzle with your finger and spraying (creates bubbles in the cup).

6) Check the coating for uniformity and coverage then use a Q-Tip to wipe excess off the sides of the heater.

7) Place the coated heater under a lamp for curing. Curing takes about 24 hrs.

For 17-30 μm aluminum particles, a drip method was employed. The drip method uses a #3 standard artist paintbrush. The following is the method:

1) Shake the coating well and then stick the brush in the vial and stir without touching the bottom of the vial. Since Brushable Ceramic has large iron particles that settle in the bottom, avoid picking them up in the paintbrush.

2) After stirring, pull the paintbrush up and slightly touch the side of the vial to pull a small drop from the paintbrush.

3) Pull the paintbrush from the vial, then mash it on the surface of the heater, and then remove it. The heater must be perfectly horizontal. In addition, aim the tip of the paintbrush at the center of the heater. The brush will then bend over toward the edge.

4) Allow the MEK to fully evaporate.

5) Place the coated heater under a lamp for curing. Curing takes about 24 hrs.

O'Connor and You [21] found that the optimum thickness of ABM coating with 8-12 μm particles was ~50 μm. For other size ranges of ABM coatings, the selected thicknesses were determined by the appropriate ratio (mean size of particle/thickness = 10 μm / 50 μm). Therefore, the thicknesses for current ABM coatings test are; 3-4.5 μm = ~20 μm, 4.5-7 μm = ~30 μm, 10-14 μm = ~60 μm, and 17-30 μm = ~120 μm.

3.1.2 SEM Images

After fabricating all five different ABM coatings, SEM images of ABM coatings were obtained. Figures A.7-11 show the SEM images of 3-4.5, 4.5-10, 8-12, 10-14, and 17-30 μm, respectively. Numerous cavities with multi-layered are successfully created for all cases as shown in figures. The aluminum particles look mostly round shaped (almost 100% in 3-4.5 and 4.5-10 μm) and range in size as specified by manufacturer. Some irregular shapes of metal particles can be seen at ABM coatings of 8-12, 10-14, and 17-30 μm. It is seen that, as nominal sizes of particles increase, the size of cavities increases accordingly. Extremely small sizes (~less than 1 μm) of aluminum particles were shown at all over the place in SEM images of each ABM coatings. This is due to the manufacturing process of metal particles, which employs a meshing method with a net. Since most microporous cavities shown in SEM images were not affected by tiny aluminum powders, the existence of tiny aluminum particles in the ABM coatings can be ignored for current research.

3.2 Pool Boiling Test Results

Effects of different aluminum particle sizes (3-4.5, 4.5-7, 8-12, 10-14, 17-30 μm diameter) on boiling performance of ABM coatings have been investigated in saturated R-123, FC-72 and water at atmospheric pressure.

3.2.1 R-123

Figure A.12 illustrates the pool boiling curves of the plain and microporous surfaces immersed in saturated R-123 at atmospheric pressure. The single-phase natural convection data of all of the surfaces exhibit constant heat transfer coefficients indicating equivalent areas and showing negligible surface microstructure effects. The incipient superheat values of the 17-30 μm is the lowest while other sizes shows the similar trend with a plain surface. In order to understand this phenomenon, following analysis was postulated (also mentioned in section 1.2.2). For a given working fluid at certain pressure, the liquid properties are fixed and the required superheat to initiate liquid vaporization at the liquid-vapor interface is dependent only on, and inversely proportional to the embryonic bubble radius.

$$\Delta T_{sat} = T_w - T_{sat}(P_f) = \frac{2\sigma}{r_b}\left(\frac{T_{sat} \cdot v_{fg}}{h_{fg}}\right)$$

Therefore, the more vapor trapped in a cavity, the larger the embryonic bubble radius and the lower superheat required to initiate bubble growth. Hence, varying size of cavities can be a key point for boiling optimization in specific working fluids with given thermal properties.

The surface microstructure effect on nucleate boiling heat transfer and CHF can be clearly seen in figure A.13. In general, all particle sizes of ABM coating show a huge enhancement of nucleate boiling and CHF over a plain surface at entire heat flux range. 3-4.5 μm size shows the lowest enhancement of boiling performance, ~120% for nucleate boiling and ~20% for CHF. 8-12 μm size shows the best enhancement for both nucleate boiling and CHF, ~370% for nucleate boiling and ~60% for CHF. At low heat flux range, less than 5 W/cm^2, the largest size (17-30 μm) shows the highest nucleate boiling performance among others.

3.2.2 FC-72

Figure A.14 shows the pool boiling curves of the plain and ABM coatings immersed in saturated FC-72 at atmospheric pressure. Again, the natural convection data of all of the surfaces exhibit identical heat transfer coefficients indicating equivalent areas and showing negligible surface microstructure effects. The incipient superheat values of the present ABM coated surfaces are comparable with those of Rainey and You [31] and show the same decreasing trend with increased “surface roughness” as previously reported by Rainey and You [31]. O’Connor and You [21] attributed the decrease in incipient superheat for their microporous coating compared to plain surfaces primarily to the presence of larger embryonic bubble diameters produced by increased vapor/gas entrapment in the microstructure. The nucleate boiling coefficients of all ABM coated surfaces in figure A.15 show significant increases in heat transfer coefficient and is believed to be a direct result of increased active nucleation site density. At low heat flux region (under 5 W/cm^2), the largest size (17-30 μm) again shows the highest nucleate boiling coefficient while 3-4.5 μm (smallest) shows the least enhancement of nucleate boiling. After 10 W/cm^2, 4.5-7 μm shows the best enhancement of nucleate boiling (~350%) until it reaches comparatively low CHF, ~20 W/cm^2. 8-12 μm shows the best nucleate boiling performance at middle heat flux range of 5-10 W/cm^2 and provides the highest CHF enhancement (~60%).

3.2.3 Water

Figure A.16 shows the pool boiling curves of the plain and ABM coatings immersed in saturated water at atmospheric pressure. The pool boiling test was conducted until a heat flux reaches at ~50 W/cm^2 due to the temperature limitation of Brushable Ceramic (~130°C). The natural convection data of all the surfaces exhibit well matched agreement. Enhancement of the boiling incipience of 17-30 μm is clearly shown in figure 3.10 while 3-4.5 and 4.5-7 μm show almost same boiling incipience with a plain surface. 3-4.5 and 4.5-7 μm show no enhancement of nucleate boiling over a plain surface while 17-30 μm holds the largest enhancement (~40%) until a heat flux reaches at 40 W/cm^2. In figure A.17, the nucleate boiling coefficient of 10-14 μm size seems to capture the performance of 17-30 μm above ~40 W/cm^2. The maximum enhancement of nucleate boiling coefficient (~40%) of ABM coatings in water seems to be very low compared to the results from R-123 and FC-72 (~350-370%). Rainey and You [32] reported that the enhancement effectiveness of the microporous coating diminishes significantly in flow boiling of FC-72 at high heat flux region and high velocities since the additional thermal conduction resistance of binders in ABM coatings becomes a dominant factor at high heat flux region. Based upon their analysis and current boiling results for water, it is imperative to develop thermally conductive microporous coatings to enhance the boiling performance for water because a boiling in water can dissipate higher heat flux due to its superior thermal properties over refrigerants. Hence, next chapter will present and describe the development of thermally-conductive microporous coatings in detail.

CHAPTER 4

CONDUCTIVE MICROPOROUS COATINGS

This chapter will describe the development of thermally conductive microporous coatings, which resulted from insignificant boiling enhancement of conventional non-conductive microporous coating techniques for water. A significant advantage of this conducting microporous coating is insensitivity of coating thickness due to the high thermal conductivity of solder binders. In addition, the coating technique is efficient for various types of working liquids simply by changing the size of metal particle sizes since different surface tension of liquids requires different sizes of porous cavities to optimize boiling heat transfer performance.

4.1 Multi-Staged Electroplating

Bliss et al. [33] performed the electroplatings of 130 μm layers of copper, chrome, nickel, cadmium, tin, and zinc on stainless steel tubes. They have found copper, chrome, and cadmium electroplated surfaces provided the enhancement of nucleate boiling in the range of 200-300%. Albertson [34] showed that electroplating at very high current densities built the formation of dendrites and nodules on the base surface. This porous surface induced the large heat transfer increase for boiling R-12. The current research utilizes the electroplating at multi-stages of current fluxes to construct the cavities and to bond the microporous structures.

4.1.1 Bath Preparation and Coating Procedure

The bath is prepared with composition of cupric sulfate (200 grams/liter), H_2SO_4 (70 grams/liter), and 2%-Hydrochloride (10 ml/liter). The surface of test heater should be pre-cleaned with Hydrochloric (2%) before the process for higher bonding strength of coatings. The copper electrode is connected into positive (+) pole and the desired surface to be coated is connected into negative (−) pole in D.C. power supply, which is controlled by personal computer, as shown in figure A.18. The magnetic stirrer is used to generate the uniform coating surfaces by distributing electric field uniformly. Desired high current density of 0.166, 0.25, 0.33, 0.5, 1.0, and 1.2 A/cm^2 are maintained with fixed duration of 20-30 seconds to build the dendrites and nodules. A fixed low current density of 0.05 A/cm^2 is applied for 80 minutes for all cases to create the permanent bonding strength of microporous structures. After electroplating process is complete, the electroplated surfaces are rinsed with distilled water and dried completely with pressured air before boiling test.

4.1.2 Microporous Structure and SEM Images

SEM images of multi-staged electroplating coatings were obtained. Figures A.19-24 show the SEM images of 0.166, 0.25, 0.33, 0.5, 1.0, and 1.2 Ampere/cm^2, respectively. MSE coating with 0.166 Ampere/cm^2 seems to have very tiny cavities as shown in figure A.19 while other MSE coatings show numerous cavities in figures. MSE coating with 0.25 Ampere/cm^2 forms into mounds, comparatively large and round shapes as shown in figure A.20. Many cavities can be seen at the area where those hills are interconnected. MSE coatings with 0.33 and 0.5 Ampere/cm^2 generate numerous tiny particle shapes on a surface as shown in figures A.21 and A.22. 0.5 Ampere/cm^2 fabricates somewhat irregular shapes of copper particles. Interestingly, MSE coatings with 1.0 and 1.2 Ampere/cm^2 construct microporous cavities with shapes of a honeycomb, probably due to the high current field. Generally speaking, SEM images of MSE coatings look very identical with ABM coatings in terms of microporous structures except that MSE coating has no glue or epoxy as a binder.

4.2 Multi-Temperature Soldering Process

The fabrication of microporous surfaces can be also achieved by thermally conducting components such as sintering process. The sintered microporous surfaces generate a highly effective porous surface; however it is known to be an expensive process which requires extremely high operating temperatures. The motive of current research is an improvement of microporous coating method and consists of metal particles (various size ranges) and the solder paste that bonds the metal particles together in order to produce numerous microporous cavities on a target surface. Nickel particles were chosen because they are highly resistant to atmospheric corrosion and to most acids. The MTSP is stemmed from an effort to combine the advantages of a mixture batch type (inexpensive & easy process) and thermally-conductive microporous coating (low thermal resistance of conduction).

4.2.1 Coating Components and Procedures

The optimized coating component is on U.S. patent processing. Currently, this microporous coating is U.S. patent pending. The coating procedure is as follows;

1) Prepare nickel powder, premixed solder paste, ethyl alcohol, and solder flux.

2) Mix them as given optimum ratios with small amount of solder flux.

3) Blend (disperse) the coating mixtures thoroughly and uniformly using an ultrasonic bath.

4) Apply thin layer of solder flux on a target surface in order to expedite formation of micro-pores during the bonding process between nickel powders.

5) Paint the coating mixture on a target surface by using a paintbrush.

6) Heat the sample up slowly to 100°C to vaporize the ethyl alcohol (carrier).

7) Heat up to 250 °C to melt solder paste, and then cool it down to room temperature.

8) Remove the residue of flux on the surface with acetone & hydrochloride (2%), or any kinds of flux remover commercially available.

4.2.2 Microporous Structure and SEM Images

Figure A.25 shows the SEM images of nickel particle coated surfaces for -325 mesh sizes of nickel particles (8-12 μm). It shows numerous active nucleation sites with a wide range of cavity sizes from 3-5 μm up to +10 μm. Figure A.26 and A.27 show the microscopic images of MTSP coatings with -100+325 and -50+100 mesh, respectively. As shown in the figures, the soldering carriers are clearly seen as binders between nickel particles and resultantly produce numerous microporous structures. Figure A.26 shows that -100+325 mesh (30-50 μm) MTSP coating generates the microporous sizes of cavities in the range from 5 to 50 μm. This wide range of cavity sizes are due to the randomness of solder amount interconnecting the nickel particles. Figure A.27 shows somewhat uniform sizes (~50-100 μm) of cavities for MTSP coating with -50+100 mesh nickel particles because the nickel particles are very larger (150-200 μm) than solder solids, therefore the randomness of solder amount is comparatively insensitive for MTSP coating with -50+100 mesh.

4.3 Pool Boiling Test Results

The pool boiling test of MSE and MTSP coatings are fabricated onto the 1x1 cm test heater and tested in different liquids. MSE coatings are tested in saturated R-123, FC-72 and water at atmospheric pressure. MTSP coatings are tested in saturated R-123, FC-72, methanol, and water at the atmospheric pressure also. Their pool boiling results are presented in this chapter.

4.3.1 MSE coatings for R-123

Figure A.28 demonstrates the pool boiling curves of the plain and MSE coated surfaces immersed in saturated R-123 at atmospheric pressure. In addition, nucleate boiling curve of plain (sanded with 600 grits) surface is shown for reference. It is confirmed that negligible surface microstructure effects exist from the single-phase natural convection data. The incipient superheat values and CHF of the MSE coatings with 1.0 and 1.2 Ampere/cm^2 are the smallest, which is the similar trend with ABM coatings. The surface microstructure effect on nucleate boiling heat transfer can be obviously seen in figure A.29. All MSE coatings show the significant enhancement of nucleate boiling over a plain surface at entire heat flux range in saturated R-123. MSE with 0.166 Ampere/cm^2 shows the least enhancement of boiling performance (~80% enhancement for nucleate boiling and ~20% for CHF). As seen in figure A.19, this lowest boiling enhancement is due to the lack of sufficient number of active nucleation sites. MSE with 0.5 Ampere/cm^2 shows the largest enhancement for nucleate boiling and CHF, up to ~700% for nucleate boiling and ~50% for CHF. The remarkable heat transfer coefficient value of 100,000 W/°C·m^2 could be obtained at the heat flux of ~35 W/cm^2 in saturated R-123 at atmospheric pressure by using MSE coating with 0.5 Ampere/cm^2. MSE coating with 1.0 Ampere/cm^2 shows an equivalent nucleate boiling enhancement with 0.5 Ampere/cm^2. However, CHF enhancement is the least one among others.

4.3.2 MSE coatings for FC-72

Based on the results from previous R-123 boiling experiments, MSE coatings with 0.166, 0.33, 0.5, and 1.2 Ampere/cm^2 were selected and tested for FC-72. Figure A.30 presents the pool boiling curves of the MSE coated surfaces immersed in saturated FC-72 at atmospheric pressure. The single-phase natural convection data was confirmed to be well collapsed each other. The incipient superheat values of all MSE coatings in FC-72 are the same and significantly smaller than those in R-123. In order to examine the boiling coefficient of MSE coatings more clearly, the boiling data were re-plotted in h vs. q" as shown in figure A.31. It is to be noted all MSE coatings show the significant enhancement of nucleate boiling over a plain surface at entire heat flux range in saturated FC-72. MSE coating with 0.166 Ampere/cm^2 shows again the least enhancement of boiling performance (~50% enhancement for nucleate boiling and ~20% for CHF). MSE coating with 0.5 Ampere/cm^2 size shows the largest enhancement of nucleate boiling coefficient up to ~600% with 60% enhancement for CHF over a plain surface. This phenomenon is very identical with R-123 case. The heat transfer coefficient of ~50,000 W/°C·m^2 was obtained at the heat flux of ~22 W/cm^2 in saturated FC-72 at atmospheric pressure by using MSE coating with 0.5 Ampere/cm^2.

4.3.3 MSE coatings for Water

Based on the results from boiling experiments of R-123, MSE coatings with 0.166, 0.33, 0.5, and 1.2 Ampere/cm^2 were tested for water. Figure A.32 shows the pool boiling curves of the MSE coatings comparing with a plain surface immersed in saturated water at atmospheric pressure. Enhancement of the boiling incipience of all MSE coatings is clearly shown in figure A.32. Compared to non-conductive microporous coatings, ABM coatings, a dramatic enhancement of nucleate boiling performance are obtained for saturated water using MSE coatings. Enhancement of CHF for all MSE coatings in water is approximately in the same range (~30-40%). The boiling data are re-drawn in h vs. q" as shown in figure A.33 to compare the boiling performance of various MSE coatings. MSE coating with 0.166 Ampere/cm^2 again shows the smallest enhancement of nucleate boiling performance (~50%) whereas MSE coating with 0.5 Ampere/cm^2 size shows the largest enhancement of nucleate boiling performance (up to ~250%) over a plain surface. The heat transfer coefficient of ~147,000 W/°C·m^2 was obtained at the heat flux of ~150 W/cm^2 in saturated water at atmospheric pressure by using MSE coating with 0.5 Ampere/cm^2. This dramatic increase in heat transfer coefficient for water, compared to other liquids, could be possible due to the thermally conductive microporous coatings, MSE coatings, in combination with superior thermal properties of water.

4.3.4 MTSP coatings for R-123

For boiling test of R-123 for MTSP coatings, a test heater was slightly modified due to the chemical reaction factor. For ABM and MSE coatings, the coating process was followed after the test heater, which is shown in figure A.5, was fabricated by masking unwanted area. Since MTSP must be cured at 230°C to melt the soldering process, MTSP coating process must be performed on the copper block before building a test heater (the temperature limitation of a test heater is ~150°C). This reversed process caused a major difficulty of sealing the copper block with an epoxy. The microporous structures on the heater surface were easily smeared and filled with epoxy due to the capillary pumping, causing a severe degradation of boiling performance. Therefore, a special tape must be used to attach and segregate the sides of copper block after MTSP coatings were applied from the epoxy. It is found that the tape was severely reacted with R-123, but not reacted with FC-72 and water. The schematic view of modified test heater is shown in figure A.34 along the boiling curves of R-123. 1.2 x 1.2 cm-thin copper spreader (0.6 mm thickness) was jointed onto the copper block by soldering. Figure A.34 illustrates the pool boiling curves of the MTSP coated surfaces immersed in saturated R-123 at atmospheric pressure. A nucleate boiling curve of plain surface is also shown for reference. Even though it is confirmed that negligible surface microstructure effects exist from the single-phase natural convection data, the incipient superheat values of the MTSP coatings are the same with a plain surface, which might be caused by the thin copper spreader. However, once the nucleate boiling is ignited, all MTSP coatings show the huge enhancement of nucleate boiling over a plain surface at entire heat flux range in saturated R-123. However, the amount of enhancement is underestimated for MTSP in R-123 compared to other microporous coatings in R-123 due to the existence of thermal resistance of soldered layer between thin copper spreader and copper block. MTSP coating with -325 mesh shows the least enhancement of boiling performance (~150% enhancement for nucleate boiling and ~35% for CHF) as shown in figure A.35. MTSP coating with -50+100 mesh, largest nickel particles, shows the largest enhancement for nucleate boiling at the heat flux range of 0-16 W/cm^2 (up to ~300%) while MTSP coating with -100+325 mesh shows the best performance of nucleate boiling heat transfer at above 16 W/cm^2. Enhancement of CHF for all MTSP coatings in R-123 is approximately in the same range (~30-40%).

4.3.5 MTSP coatings for FC-72

Figure A.36 exhibits the pool boiling curves of the MTSP coated surfaces immersed in saturated FC-72 at atmospheric pressure. Lower wall superheats at boiling incipience for all MTSP coatings are confirmed that a plain surface. CHF enhancement of MTSP coatings with -100+325 and -50+100 mesh are approximately similar (~80%) while -325 mesh shows the least CHF enhancement (~30%) over a plain surface. Throughout the nucleate boiling regime, all three MTSP coatings consistently augmented the heat transfer coefficients by up to ~ 600% when compared to those of the plain surface. As shown in figure A.37, -100+325 mesh (30-50 μm) particle sizes produced highest nucleate boiling heat transfer coefficients at low heat flux (~up to 12 W/cm^2) while the boiling graphs of -100+325 and -325 mesh particles sizes collapse in the same line right after 12 W/cm^2 and -325 mesh overtakes the performance of -

100+325 mesh. -50+100 mesh (100-200 μm) MTSP shows the smallest enhancement of nucleate boiling heat transfer since the size of cavities are assumed to be too large for FC-72. The maximum heat transfer coefficient of boiling that MTSP can achieve seems to be ~40,000 W/°C·m^2 at the heat flux of 20 W/cm^2.

4.3.6 MTSP coatings for Methanol

For MTSP coatings, an additional working liquid, methanol, was added for study of boiling heat transfer. Figure A.38 shows the boiling results for MTSP with all sizes of nickel powders tested in saturated methanol at atmospheric pressure along the results of a plain surface. Enhancement of the boiling incipience of all MTSP coatings over a plain surface is clearly shown in figure A.38. Remarkably, -50+100 mesh size (the largest size) shows the dramatically early boiling incipience. MTSP coating with -100+325 mesh size of shows the highest levels of enhancement of nucleate boiling in figure A.39. This might be due to increased cavity size requirement for saturated methanol since the surface tension of methanol is comparatively larger than that of FC-72 as shown in table B.2 and B.3. The nucleate boiling coefficient results of -325 and -50+100 mesh sizes particle sizes are about the same as shown figure A.39. The CHF values of -100+325 and -50+100 mesh sizes are moderately similar and ~20-30% larger than that of -325 mesh size MTSP with small size particles (8-12 μm). However, the CHF of small particle size was not fairly enhanced over plain surface even though the nucleate boiling of small particle size shows a significant boiling enhancement over a plain surface.

4.3.7 MTSP coatings for Water

Boiling experiments of MTSP coatings in saturated water were performed at atmospheric pressure and the results are shown in figure A.40. Enhancement of the boiling incipience of all MTSP coatings is apparently shown in the figure. CHF enhancement for all MTSP coatings in water is obtained and -50+100 mesh size shows the largest CHF increase from a plain surface (~50%). The -50+100 mesh (100-200 μm) particle sizes shows slightly higher nucleate boiling coefficients at low heat flux region than -100+325 mesh size while the -100+325 mesh size takes the lead the higher enhancement of nucleate boiling than 100-200 μm after ~40 W/cm^2 in figure A.41. MTSP coating with -325 mesh shows the least nucleate boiling and CHF enhancement over a plain surface, which is a similar result caused by sizes of particles from methanol results. The heat transfer coefficient of ~150,000 W/°C·m^2 was acquired at the heat flux of ~150 W/cm^2 in saturated water at atmospheric pressure by using MTSP coating with -100+325 mesh size, which is quite lower than that of optimized MSE coating (~230,000 W/°C·m^2 at the same heat flux).

4.4 Boiling Performance Comparison of Microporous Coatings

This section will briefly compare the boiling performance of ABM, MSE, and MTSP coatings in saturated R-123, FC-72, and water. The boiling results from section 3.2 and 4.3 are re-plotted to perform the comparison study. Only the optimized results from each coating methods for specific working fluids are selected and plotted for comparison.

4.4.1 Comparison for R-123

Figure A.42 shows the pool boiling curves of ABM and MSE coatings in saturated R-123 at atmospheric pressure with a plain surface result as a reference. The boiling data of MTSP coatings was excluded due to the inconsistency of test heater as discussed in section 4.3.4. ABM coating with 8-12 μm produced the highest boiling enhancement for R-123 while MSE coating with 0.5 Ampere/cm^2 was selected for comparison. As shown in figure A.43, ABM coating, non-conductive option, shows a significant boiling enhancement over a plain surface. MSE coating, thermally conductive coating option, further enhanced the boiling performance (nucleate boiling coefficient and CHF). The maximum boiling coefficient of MSE coating is ~100,000 W/°C·m^2 at the heat flux of 30 W/cm^2. At the same heat flux, ABM coating shows the boiling heat transfer coefficient of ~35,000 W/°C·m^2.

4.4.2 Comparison for FC-72

Figure A.44 shows the pool boiling curves of ABM, MSE, and MTSP coatings immersed in saturated FC-72 at atmospheric pressure with a plain surface data as a reference. ABM coating (8-12 μm) shows the least nucleate boiling enhancement over a plain surface while MSE (0.5 Ampere/cm^2) and MTSP (-100+325 mesh) coatings show the same nucleate boiling coefficient at the low heat flux region (0-12 W/cm^2). After 12 W/cm^2, MSE coating leads the highest nucleate boiling performance as shown in figure A.45. The maximum boiling coefficient of MSE coating is ~45,000 W/°C·m^2 at the heat flux of ~20 W/cm^2. At the same heat flux, MTSP and ABM coatings show the boiling heat transfer coefficient of ~36,000 and ~24,000 W/°C·m^2, respectively.

4.4.3 Comparison for Water

Figure A.46 shows the pool boiling curves of ABM, MSE, and MTSP coatings in saturated water at atmospheric pressure. Obtained boiling data of ABM coating (17-30 μm) shows insignificant nucleate boiling enhancement over a plain surface only at the low heat flux region. It can be postulated from the boiling curve pattern that the ABM coating will be generating worse boiling performance than a plain surface as shown in figure A.46. This result was very similar with flow boiling research conducted by Rainey et al. [32] as discussed earlier. MTSP (-100+325 mesh) coatings shows higher nucleate boiling coefficient than MSE (0.5 W/cm^2) at the entire heat flux region. Approaching to ~160 W/cm^2, MSE coating catches up with the nucleate boiling performance of MTSP as shown in figure A.47. The maximum boiling coefficient of MSE coating is ~147,000 W/°C·m^2 at the heat flux of ~150 W/cm^2. At the same heat flux, MTSP coating shows the boiling heat transfer coefficient of ~150,000 while ABM coating data is unavailable.

4.5 Boiling Performance of MTSP at 60°C of Saturation

In electronic cooling industries, a maximum operating temperature for chips is subject to be less than ~80˚C generally. Since the boiling point of water at atmosphere is comparatively high, 100˚C, it is very important to accumulate the boiling results of microporous coatings in water at lower saturation temperature (pressure). In order to investigate the system pressure effects on boiling performance of microporous coatings in saturated water, MTSP coating (-100+325 mesh) was selected for current study. A selection of MTSP coating for this study was determined since the pressure test involves with real application and MTSP coating has a strong environmental resistance. The boiling experiment data at T_{sat} = 60°C are used based upon typical operating temperature for electronic cooling applications. Figure A.48 shows the boiling performance comparison between MTSP (-100+325 mesh) and a plain surface for saturated water at pressure of 2.89 psia (T_{sat} = 60°C) along with boiling results at atmospheric pressure (100°C saturation). It is seen that the nucleate boiling performance degrades as the system pressure decreases regardless of surface conditions in the figure. Approximately 250% enhancement of nucleate boiling was achieved for MTSP compared to the plain surface at the heat flux of 75 W/cm^2 as shown in figure A.49. In addition, MTSP coating provides ~70% enhancement of CHF over a plain surface. In saturated water at atmospheric pressure, MTSP coating enhances the boiling coefficient by ~300% at the same heat flux and augments CHF by ~40% over a plain surface. Therefore, it can be concluded that the enhancement trend of boiling performance by MTSP coating is fairly consistent regardless of the system pressure.

CHAPTER 5

FURTHER RESEARCH FOR APPLICATIONS

This chapter will conduct further research of microporous coatings for real applications. Double enhancement of microporous coatings combined with effect of spreading for indirect cooling for electronic chips, nanofluids for high power dissipation, and anti-freezing of water are the major concerns in this chapter.

5.1 Spreader Effects for Indirect Cooling

Indirect cooling scheme requires the investigation of spreader effects due to the module geometry as shown in figure A.1. In other words, a thermal spreading resistance exists when heat flows from one region to another different cross sectional area. It is well known that the spreading resistance can be generally reduced by increasing the thickness of spreader. A spreader onto the heated surface induces the spreading and conduction resistance in addition to the thermal contact resistance between a spreader and heater. From the current heater configuration shown in figure A.6, the contact resistance in this study can be excluded for analysis. For a heat sink design, it is necessary to optimize the thickness of spreader since spreading resistance is inversely proportional with conduction resistance. When boiling occurs at the surface as shown in figure 2.3, the boiling area depends on the spreader thickness, which affects the boiling performance significantly. Therefore, the effects of spreader thickness combined with boiling performance of MTSP coating are studied in this section. To investigate the effects of spreader thickness, 1.5, 2.5, 3.5, 5.5, and 6.5 mm thicknesses are selected and tested. The study was performed in FC-72 and water at different saturation temperatures to investigate the effects of working fluids and system pressure.

5.1.1 Water Test

Figure A.50 shows the boiling curves of MTSP (-100+325 mesh) coating with spreader of 1.5 mm thickness in saturated water at different saturation temperatures (45, 55, and 65°C). This temperature range was determined by considering the operating temperature ranges of conventional electronic devices. Figure A.50 clearly illustrates the effect of system pressure on the saturated nucleate boiling curves of the MTSP coated surface. In a saturated condition, changing system temperature causes change of system pressure according to the thermodynamic of pure substance. 45, 55, and 65°C of saturated water corresponds to 9.6, 15.8, and 25.0 kPa in saturation pressure, respectively. In general, the incipient superheat increases with decreasing pressure, which is similar to the observations of You et al. [35]. The effect of pressure on the nucleate boiling performance is consistent with the prevailing trend in the literature of increased heat transfer coefficient and CHF with increased pressure [36]. At 200 W/cm^2, the boiling coefficient of MTSP coating at 45, 55, and 65°C are ~70,000, 100,000, and 130,000 W/°C$\cdot$m^2, respectively as shown in figure A.51. In figures A.52-59, data from other thicknesses of spreaders with MTSP coating are plotted and they show the identical trend with boiling results of 1.5 mm thickness as shown in figures A.50 and A.51.

Figure A.60 shows the boiling curves of MTSP coating with different thickness of spreaders in saturated water at 45°C. In order to find the optimum thickness for maximum boiling heat transfer coefficient, h versus q" graph was plotted from boiling data and is shown in figure A.61. At 45°C saturation condition in water, 6.5 mm thickness shows the highest boiling heat transfer coefficient at low heat flux region (under ~40 W/cm^2). This is to be expected because the nucleate boiling is not fully developed at low heat flux regime. Therefore, heat transfer enhancement through better spreading is the dominant augmentation mechanism. At the heat flux range of 40-75 W/cm^2, the boiling heat transfer coefficient seems to be independent of spreader thickness. After 75 W/cm^2, the 1.5 mm thickness generates the highest boiling coefficient until it reaches the CHF (~255 W/cm^2) and 6.5 mm thickness shows the least value of boiling heat transfer coefficient until it reaches the CHF (385 W/cm^2), which is the highest CHF value among other thickness. From this result, it can be assumed that the nucleate boiling is fully developed after ~75 W/cm^2 and nucleate boiling heat transfer becomes a dominant factor. 6.5 mm thickness generated the highest CHF because the boiling area on heated surface is assumed to be largest among other thicknesses due to the spreading.

Figure A.62 illustrates the boiling curves of MTSP coating with different thickness of spreaders in saturated water at 55°C. 6.5 mm thickness again shows the largest boiling heat transfer coefficient at low heat flux region (under ~60 W/cm^2) and highest CHF value as shown figure A.62 and A.63. After ~95 W/cm^2, the 1.5 mm thickness shows the highest boiling heat transfer coefficient until it reaches the CHF

(~250 W/cm^2) and 6.5 mm thickness shows the least value of boiling coefficient until it reaches the CHF (400 W/cm^2), which is identical with the trends shown from the results at 45°C. Figure A.64 shows the boiling data of MTSP coating with different thickness of spreaders in saturated water at 65°C. 6.5 mm thickness produces the largest boiling coefficient at low heat flux region (under ~65 W/cm^2) and highest CHF value as shown figure A.65. After ~120 W/cm^2, the 1.5 mm thickness shows the highest boiling coefficient until it reaches the CHF (~260 W/cm^2).

5.1.2 FC-72 Test

In order to investigate the working fluids effect on spreader test, boiling test for same thicknesses of spreader with water case described in section 5.1.1 are repeated in saturated FC-72. Figure A.66 shows the boiling curves of MTSP (-100+325 mesh) coating with spreader of 1.5 mm thickness in saturated FC-72 at different saturation temperatures (35, 45, and 55°C). This temperature range was modified from water test to maintain the system pressure under atmospheric pressure since the boiling temperature of FC-72 at atmosphere is ~56.5°C. Figure A.66 apparently demonstrates the effect of system pressure on the saturated nucleate boiling curves of the MTSP coated surface immersed in saturated FC-72. The effect of pressure on the nucleate boiling performance is consistent with the trend shown in water test. The nucleate boiling coefficient and CHF degrades as decreasing the system pressure. At 100 W/cm^2, the boiling heat transfer coefficient of MTSP coating at 35, 45, and 55°C are ~43,000, 52,000, and 60,000 W/°C·m^2, respectively as shown in figure A.67. CHF occurred at

~210, 225, and 240 W/cm2 for 35, 45, and 55°C, respectively. The data from other thicknesses of spreaders with MTSP coating in 35, 45, and 55°C saturated FC-72 show the very similar behavior of boiling performance with boiling results of 1.5 mm thickness as shown in figures A.68-75.

Figure A.76 illustrates the boiling curves of MTSP coating with different thickness of spreaders in saturated FC-72 at 35°C. To seek the optimum thickness for highest boiling heat transfer coefficient value, h versus q" graph was generated from boiling data as shown in figure A.77. For 35°C saturated condition in FC-72, 6.5 mm thickness shows the highest boiling heat transfer coefficient at entire heat flux region except the low heat flux region (under ~40 W/cm^2) while 1.5 mm thickness shows the least boiling heat transfer coefficient. Basically, it can be concluded that the boiling heat transfer coefficient and CHF degrades as the thickness of spreader decreases for FC-72 as shown in figure 5.28. This means that spreading heat transfer mode for FC-72 plays an important role in total heat dissipation in opposition to water case. This can be expected because the nucleate boiling heat transfer coefficient of MTSP in saturated FC-72 is significantly lower than in saturated water as mentioned earlier chapter (~40,000 $W/°C\cdot m^2$ for FC-72 and 150,000 $W/°C\cdot m^2$ for water). Therefore, heat transfer through spreading in copper for FC-72 gives more influence on total heat dissipation augmentation compared to water. A larger thickness provides the higher CHF because the boiling area on heated surface increases as the thickness increases. Figure A.78 and A.80 demonstrate the boiling curves of MTSP coating with different thickness of spreaders in saturated FC-72 at 45 and 55°C, respectively. Identically, 6.5 mm thickness again shows the largest boiling coefficient and highest CHF value while 1.5 mm thickness for 45 and 55°C as shown figure A.79 and A.81. This trend is very identical with the results from data for 45°C saturation.

Figure A.82 and A.83 illustrate the enhancement of nucleate boiling performance by using MTSP coating and a spreader (1.5 mm thickness) in saturated water at 60°C and saturated FC-72 at 55°C, respectively. As shown in figure A.82, MTSP coating enhances the boiling performance over a plain surface significantly and a spreader with MTSP coated further enhances CHF dramatically. Nucleate boiling coefficient of MTSP with 1 x 1 cm base and MTSP with a spreader (1.5 mm thickness) are fairly collapsed (only for 1.5 mm thickness data) in the heat flux range of 0-100 W/cm^2. After 100 W/cm2, MTSP with a spreader shows a distinct enhancement of nucleate boiling coefficient over MTSP with 1 x 1 cm base copper and extend the CHF significantly (~100%). Dissimilarly with water case, MTSP coating with a spreader immersed in FC-72 shows a tremendous boiling enhancement (~900%) over a plain surface in figure a.83. At low heat flux range (under 40 W/cm^2), MTSP coating with a spreader shows lower heat transfer rate than MTSP coating with 1x1 cm copper base since this heat flux region is corresponding to natural convection regime for MTSP coating with a spreader in saturated FC-72. The maximum boiling coefficient of a plain surface is less than ~10,000 W/°C·m^2, while MTSP coating with 1x1 cm base and

MTSP coating with a spreader show the boiling coefficient of ~45,000 and 90,000 W/°C·m^2, respectively.

In order to explain the significant difference of boiling enhancement by MTSP coating with a spreader between water and FC-72, the boiling pictures from 2.5 mm thickness spreader in saturated FC-72 and water are obtained and shown in figure A.84. The operating temperature and heat flux were maintained equally for comparison purpose (55°C and ~150 W/cm^2, respectively). As seen in figure A.84, the boiling area for FC-72 is greatly larger than for water. This revelation can explain the huge difference of boiling enhancement between water and FC-72. This picture demonstrates that the spreader generates larger boiling area in FC-72 than in water at the identical condition due to the lower surface tension of FC-72 than that of water as shown in table B.2 and B.4.

5.2 Nanofluids

Nanofluids are the new kinds of heat transfer fluids containing nanoparticles that are suspended uniformly and stably in a liquid as shown in figure A.85. Numerous theoretical and experimental studies of the effective thermal conductivity of liquids containing suspended solid particles have been previously conducted. However, with very few exceptions, previous studies of the thermal conductivity of suspensions have been confined to those containing millimeter- or micrometer-sized particles. Choi et al. [37] found intriguing experimental results of thermal conductivity enhancement for nanofluids containing carbon nanotubes, revealing that the increase in thermal conductivity was greater than existing theoretical predictions. Eastman et al. [38]

demonstrated that nanofluids consisting of copper nanoparticles in ethylene glycol exhibit enhanced thermal conductivity. A maximum increase in thermal conductivity of approximately 40% was observed in that study for 0.3 volume % Cu nanoparticles with average diameter of less than 10 nm dispersed in ethylene glycol.

Recently, two experimental studies have been reported on the boiling heat transfer of nanofluids. In 2003, You et al. [39] noticed that an addition of nanoparticles in water generates up to 200% enhancement of critical heat flux (CHF). They tested the pool boiling experiments with a flat heater by varying concentrations of aluminum oxide nanoparticles ranging from 0 (pure water case) to 0.05 grams per liter at the pressure of 2.89 psia (T_{sat} = 60ºC). Vassallo et al. [40] also performed pool boiling heat transfer experiments in silica-water nanofluids by using a wire heater. They reported a marked increase in CHF for nano-solutions compared to pure water.

The present study is to further understand the boiling heat transfer of nanofluids. In addition, the present study focuses on the enhancement of CHF combined with microporous coating in saturated nanofluids.

5.2.1 CHF Enhancement of Nanofluids

The boiling curves of the nanofluids at different concentrations are excerpted and modified from You et al. [39] and shown in figure A.86. The boiling curve of pure water was placed on the same graph to provide a better comparison. It is shown that the fully developed nucleate boiling started at approximately 20 W/cm^2. In the fully developed nucleate boiling regime, the boiling heat transfer coefficient values of all concentrations including pure water appear to be the same. As concluded by You et al.

[39], the nucleate boiling heat transfer coefficient is not affected by having a small amount of nanoparticles.

5.2.2 Boiling Mechanism Analysis

In a boiling surface, the total heat dissipation is divided into four different modes of heat transfer: latent heat, micro-convection, natural convection, and Marangoni flow. Latent heat transfer takes place when liquid vaporizes and leaves the heated surface, micro-convection results from sensible heat energy removed by entrainment of the superheated liquid in the departing bubble’s wake, natural convection is the sensible energy transport removed from non-boiling portions of the heated surface due to density gradients, and finally Marangoni flow is caused by the surface tension gradient while the bubble is still attached to the surface.

Latent heat transfer and micro-convection are generally considered as a primary heat transfer mechanism in fully developed and saturated nucleate boiling because Marangoni flow effect is negligible if the liquid is fully saturated, and natural convection is ignored when bubbles are fully developed on a heated surface. The latent heat contribution can be calculated by measuring vapor volume flow rate from a surface and micro-convection can be estimated by subtracting the amount of latent heat from a total heat transfer in fully developed and saturated nucleate boiling.

In order to investigate the boiling heat transfer mechanism in nanofluids and pure water, boiling experiments using a platinum wire as a heater were conducted. The wire test heater consists of a platinum wire soldered between two copper terminals that connect the voltage probe and the power supply. The images of departing bubbles were captured and analyzed for boiling mechanism study using the consecutive photo method [28]. Sample images of bubbles departing from a wire heater immersed in water and nanofluids are shown in figure A.87. The boiling images were analyzed in terms of the size and frequency of bubbles. The latent heat flux contribution to the total heat transfer from the heated wire was determined by measuring volumetric bubble flow rate as suggested by Ammerman and You [28]. The process of liquid heating, nucleation, growth of bubble, and departure can be referred to the main mechanism of heat transfer during nucleate boiling. In this experiment, the steady-state vapor volume flows rate measured with the consecutive-photo method [28] were used to estimate the latent heat portion to the total heat transfer from the heated wire. The following equation was used to compute latent heat flux:

$$q_{LH} = \frac{\rho_v \dot{V}_v h_{lv}}{\pi DL}$$

where h_{lv} is the latent heat of vaporization, and D stands for diameter of platinum wire and L is length of wire examined. In equation, volume flow rate is only variable factor to determine the function of latent heat since the density and heat of vaporization are assumed as constant over the test. The plots of latent heat flux versus total heat flux applied for these experiments are shown in figure A.88. As shown in figure A.88, the latent heat contribution is a major heat transport mechanism of total heat dissipation for both water and nanofluids. The latent heat flux for nanofluids is relatively larger than that of water. The data for 20 and 30 W/cm^2 are more meaningful in this study since the heat flux of 10 W/cm^2 belongs to partial nucleate boiling regime as seen in figure A.86. The latent heat flux contribution steadily changes from about 68% of the total heat flux at 20 W/cm² to about 56% at 30 W/cm² in water. In nanofluids, the latent heat flux contribution also decreases from about 72% of the total heat flux at 20 W/cm² to about 65% at 30 W/cm².

From the measurement of boiling parameters using consecutive photo method presented in section 2.5, the comparison of average bubble diameters versus heat flux is shown in figure A.89. The average bubble diameters in nanofluids were approximately 1.3 times larger than in water at 20 and 30 W/cm^2. As the heat flux increases from 20 W/cm^2 to 30 W/cm^2, both nanofluids and water show constant values of bubble diameters. In order to compare the frequency difference, the plots of frequency per unit area versus heat flux for water and nanofluids are generated and shown in figure A.90. Both nanofluids and water produced a similar increasing trend of bubble frequencies from 20 to 30 W/cm^2. The bubble frequency for water was about two times greater than for nanofluids at the both heat fluxes. In order to dissipate higher heat load, the bubble size is comparatively maintained constant and the bubble frequency is increased as the heat flux increases at the tested heat flux range. The comparison of boiling parameters between two fluids revealed that the size of bubbles increases and the bubble frequency decreases significantly in nanofluids compared to those in the pure water.

Frequency distributions over the diameter of bubbles are shown in figure A.91 to investigate the behavior of departing bubbles at different heat flux values for water and nanofluids. The plot shows the peak frequency value at a certain bubble diameter for each given heat flux. The peak points for nanofluids occurred at slightly larger diameter of bubbles (~1.75 mm) than pure water cases (~1.45 mm), leading to the increase of average bubble size for nanofluids corresponding to the results shown in figure A.89. Dramatic bubble peak frequency decrease from ~5000 Hz/cm^2 to ~ 1500 Hz/cm^2 occurs by adding significantly small amount of nanoparticles into pure water. In addition, it can be concluded that the bubble frequency distribution of nanofluids become flatter compared to pure water. This phenomenon might explain that departing bubbles near the heated surface merge vigorously in nanofluids or possibly depart at larger sizes

Based upon the Zuber's prediction for CHF, only remaining possible factor for CHF increase from the correlation is the surface tension, which appears proportional to CHF with ¼ power since the changes in liquid density and heat of vaporization have negligible effects on the increase of CHF for nanofluids. In order to estimate surface tension change due to the nanoparticles, the measurement of bubble sizes by consecutive photo method was employed. The bubble departure takes place when the size of the bubble becomes large enough to produce greater buoyant force that exceeds the balanced surface tension force around the perimeter of the bubble at the heater surface assuming static force balance. The balance between buoyant force and surface tension right before bubble's departure may be expressed as:

$$F_{Buoyant} = (\rho_l - \rho_v)\, g\, V = (\rho_l - \rho_v)\, g\, (\frac{1}{6}\pi d^3) = \pi\, d\, \sigma$$

From equation above, the surface tension must be proportional to diameter of bubble with 2nd power to satisfy the hydrodynamic force balance. Therefore, correlated CHF becomes proportional to $\sqrt{d}$ since the CHF is proportional to surface tension with ¼ power. In order to achieve the observed 200% increase of CHF, the diameter of bubbles must be nine times larger than that of pure water. From the measurement of bubble sizes using consecutive photo method in this current study, the average sizes of departing bubbles in the nanofluids were accurately measured and turned out to be 25% larger than in pure saturated water case. This increase provides at most 12% enhancement of CHF, much less than the observed 200% increase. Therefore, the present Zuber's prediction of CHF is incomplete to account for the effects of adding nanoparticles. In other words, possible unknown factors, potentially missing in Zuber's correlation, may exist for the 200% increase of CHF in nanofluids.

5.2.3 Boiling Test of Nanofluids with MTSP Coating

In order to investigate the effects of microporous coating on CHF enhancement of nanofluids, MTSP coating was tested in nanofluids and compared with the boiling data for MTSP coating in water. Figure A.92 shows the boiling curves of MTSP coating and a plain surface immersed in saturated water and nanofluids at 60°C saturation. Boiling performance of a plain surface in water and nanofluids seems to be well matched with previous results [39]. A increase in CHF for MTSP coating over a plain surface in pure water was obtained by ~70%. For MTSP coating in nanofluid, no degradation of boiling coefficient is detected and additional ~15% enhancement of CHF for MTSP coating in nanofluids was achieved compared to water results. This

CHF enhancement is significantly reduced compared to plain surface data (~200%). However, this CHF enhancement is still notable and further researched must be conducted to understand this phenomenon such as visualization of departing bubbles. It is concluded that the CHF enhancement of nanofluids is influenced by heater surface condition.

5.3 Conductive Microporous Coatings for Anti-Freezing of Water

This section covers the concern for freezing problem of water below 0°C at ambient. MTSP coatings are tested in anti-freeze liquids to investigate the effects of adding anti-freezer on boiling performance.

5.3.1 Anti-Freeze

In general, most refrigerants have a freezing temperature range from -90 to -135°C. The refrigerants selected for current research, R-123 and FC-72, have a freezing point of -107°C and -90°C, respectively. However, water has a freezing point of 0°C which is considerably high compared to conventional refrigerants. In order to avoid freezing problem of water, many people add certain amount of ethylene glycol or propylene glycol into pure water. Numerous researchers have performed the experimental study to find the effect of anti-freeze addition on boiling performance. Frea et al. [41] found that 50% and 75% concentration by weight of ethylene glycol significantly reduced CHF compared to pure water and ethylene glycol. In addition, they showed the reduction in nucleate boiling heat transfer occurred as the concentration of ethylene glycol increases. Investigation of Van Wijk et al. [42] with ethylene glycol and water mixture showed negligible change in critical heat flux up to concentration of 80% by weight. For current study, 20, 30, 40, and 50% concentrations (by volume) of propylene glycol (PG) are prepared to investigate the boiling performance degradation level for MTSP coatings.

5.3.2 Pool Boiling Results for MTSP coating

Figure A.93 illustrates the boiling curves of MTSP coating and a plain surface in anti-freeze liquids at 60°C saturation. Since the thermal properties of different concentrations of PG are shifted, the system pressure for each concentration at 60°C will be different. Table B.5 presents the system pressure of 20, 30, 40, and 50% PG at 60°C, which are obtained during boiling experiments. The table shows that the system pressure drops as the concentration of PG increases at the same temperature of 60°C. Therefore, the degradation of nucleate boiling performance is expected because it is well known that decreased pressure aggravates the boiling heat transfer rate. There is an obvious reduction in the nucleate boiling coefficient and CHF with increase in the concentration of propylene glycol for both MTSP coating and a plain surface. It is clearly shown in figure A.94 that boiling coefficient of MTSP coating is approximately 2.5 times larger than that of a plain surface for all concentrations of propylene glycol. At 60 W/cm^2, 20% PG shows the highest boiling coefficient of ~48,000 $W/°C \cdot m^2$ while 50% PG provides the lowest boiling coefficient of ~30,000 $W/°C \cdot m^2$.

5.3.3 Boiling Performance of MTSP Coating with Spreader

To investigate the effects of anti-freeze on boiling performance of MTSP coatings with spreader, 1.5, 3.5, and 5.5 mm thicknesses are selectively chosen and tested in anti-freezing liquids, 50% PG concentration (freezing point of -35°C) . Figure

A.95 shows the boiling curves of MTSP (-100+325 mesh) coating with spreader of 1.5, 3,5, and 5.5 mm thickness in anti-freezing liquids (50% PG) and pure water at 55°C. Figure A.95 clearly illustrates the effect of anti-freeze addition to water on the saturated nucleate boiling curves and CHF of the MTSP coated surface. Nucleate boiling performance and CHF of MTSP coating with spreaders are degraded by adding the anti-freeze, which is an identical behavior detected in boiling test with 1x1cm heater. At low heat flux region (~under 100 W/cm^2), the boiling coefficient of MTSP coating are fairly collapsed into a line regardless of spreader thickness and anti-freeze addition as shown in figure A.96. A distinct reduction in nucleate boiling heat transfer rate can be perceived in the figure by addition of anti-freeze after 100 W/cm^2 until it reaches CHF. The degradation of boiling coefficient seems to be consistent without reference to the thickness of spreader. It can be seen that ~20% of performance degradation for 1.5, 3.5, and 5.5 mm thicknesses are induced by anti-freeze at 200 W/cm^2.

CHAPTER 6

CONCLUSIONS AND RECOMMENDATIONS

6.1 Conclusion of Chapter 3

(1) Numerous active nucleation sites with multi-layered are successfully created by thermally non-conductive microporous coatings.

(2) For ABM coatings in saturated R-123, 3-4.5 μm size shows the lowest enhancement of boiling performance while 8-12 μm size shows the best enhancement for both nucleate boiling and CHF. At low heat flux range, less than 5 W/cm^2, the largest size (17-30 μm) shows the highest nucleate boiling performance among others.

(3) For ABM coatings in saturated FC-72, the largest size (17-30 μm) shows the highest nucleate boiling coefficient at low heat flux region (under 5 W/cm^2), while 3-4.5 μm (smallest size) shows the least enhancement of nucleate boiling. After 10 W/cm^2, 4.5-7 μm shows the best enhancement of nucleate boiling until it reaches comparatively low CHF, ~20 W/cm^2. 8-12 μm shows the best nucleate boiling performance at middle heat flux range of 5-10 W/cm^2 and provides the highest CHF enhancement.

(4) For ABM coatings in saturated water, 3-4.5 and 4.5-7 μm show no enhancement of nucleate boiling over a plain surface while 17-30 μm holds the largest enhancement. The nucleate boiling coefficient of 10-14 μm size seems to catch

the performance of 17-30 µm above ~40 W/cm^2. The maximum enhancement of nucleate boiling coefficient of ABM coatings in water seems to be very low compared to the results from R-123 and FC-72.

6.2 Conclusion of Chapter 4

(1) The development of thermally conductive microporous coatings, MSE and MTSP, are conducted to upgrade the conventional non-conductive microporous coating techniques.

(2) For MSE coatings in saturated R-123, MSE with 0.5 Ampere/cm^2 shows the largest enhancement for nucleate boiling and CHF, up to ~700% for nucleate boiling and ~50% for CHF whereas MSE with 0.166 Ampere/cm^2 shows the least enhancement of boiling performance (~80% enhancement for nucleate boiling and ~20% for CHF).

(3) For MSE coatings in saturated FC-72, MSE coating with 0.166 Ampere/cm^2 shows the least enhancement of boiling performance. MSE coating with 0.5 Ampere/cm^2 size shows the largest enhancement of nucleate boiling coefficient up to ~600% with only 60% enhancement for CHF over a plain surface.

(4) For MSE coatings in saturated water, MSE coating with 0.166 Ampere/cm^2 shows the smallest enhancement of nucleate boiling performance (~50%) whereas MSE coating with 0.5 Ampere/cm^2 size shows the largest enhancement of nucleate boiling performance (up to ~250%) over a plain surface. The remarkable heat transfer coefficient of ~147,000 W/°C$\cdot$m^2 is obtained at the heat

flux of ~150 W/cm^2 in saturated water at atmospheric pressure by using MSE coating with 0.5 Ampere/cm^2.

(5) For MTSP coatings in saturated R-123, MTSP coating with -325 mesh shows the least enhancement of boiling performance whereas -100+325 mesh size provides the highest nucleate boiling coefficient.

(6) For MTSP coatings in saturated FC-72, the -100+325 mesh (30-50 μm) particle sizes produced highest nucleate boiling heat transfer coefficients at low heat flux (~up to 12 W/cm^2) while the boiling graphs of -100+325 and -325 mesh particles sizes collapse in the same line right after 12 W/cm^2 and -325 mesh overtakes the performance of -100+325 mesh.

(7) For MTSP coatings in saturated methanol, MTSP coating with -100+325 mesh size of shows the highest levels of enhancement of nucleate boiling at entire heat flux.

(8) For MTSP coatings in saturated water, the -50+100 mesh (100-200 μm) particle sizes shows approximately slightly higher nucleate boiling coefficients at low heat flux region than -100+325 mesh size while the -100+325 mesh size takes the lead the higher enhancement of nucleate boiling than 100-200 μm after ~40 W/cm^2. The heat transfer coefficient of ~150,000 W/°C$\cdot$m^2 was acquired at the heat flux of ~150 W/cm^2 in saturated water at atmospheric pressure by using MTSP coating with -100+325 mesh size.

6.3 Conclusion of Chapter 5

(1) MTSP coating with spreaders in saturated water, 6.5 mm thickness shows the highest boiling coefficient at low heat flux region (under ~40 W/cm^2). After 75 W/cm^2, the 1.5 mm thickness generates the highest boiling coefficient until it reaches the CHF (~255 W/cm^2) and 6.5 mm thickness shows the least value of boiling coefficient until it reaches the CHF (385 W/cm^2), which is the highest CHF value among other thickness.

(2) MTSP coating with spreaders in saturated FC-72, 6.5 mm thickness shows the highest boiling coefficient at entire heat flux region except the low heat flux region (under ~40 W/cm^2) while 1.5 mm thickness shows the least boiling coefficient.

(3) The nucleate boiling coefficient and CHF degrades as decreasing the system pressure for boiling test in water and FC-72.

(4) The most startling trend found in the present study is the dramatic increase in CHF while increasing nanoparticle concentrations from 0 gram/liter to 0.05 gram/liter. The results show that the enhancement of CHF was achieved by ~200% increase only at 0.01 gram/liter concentration of nanofluids. Throughout the nucleate boiling regime, the heat transfer coefficients remain unchanged regardless of concentrations.

(5) The measurement of boiling parameters found that the size of departing bubbles increases and the bubble frequency decreases significantly in nanofluids compared to those in the pure water.

(6) For MTSP coating results in the nanofluid, no degradation of boiling coefficient is found and ~15% enhancement of CHF for MTSP coating in nanofluids was achieved. This CHF enhancement is significantly reduced compared to plain surface data (~200%).

(7) There is a reduction in the nucleate boiling coefficient and CHF with increase in the concentration of propylene glycol for MTSP coatings..

(8) Boiling coefficient of MTSP coating is approximately 2.5 times higher than that of a plain surface for all concentrations of propylene glycol.

(9) For MTSP coating with spreaders in antifreeze, a distinct reduction in nucleate boiling heat transfer rate can be detected by addition of anti-freeze to water after 100 W/cm^2 until it reaches CHF. The degradation of boiling coefficient seems to be consistent regardless of the spreader thickness. It is shown that ~20% of performance degradation for 1.5, 3.5, and 5.5 mm thicknesses are induced by adding anti-freeze to water at 200 W/cm^2.

6.4 Recommendations

The following are recommended for future research by the author.

(1) Additional working fluids must be investigated for ABM coatings to understand the importance of thermally conductive coating options.

(2) MSE coatings must be tested in saturated methanol to compare the boiling performance with MTSP coatings.

(3) Long term reliability test must be conducted for microporous coatings presented in this study.

(4) The effect of a confined space on the boiling performance needs to be investigated before current results can be implemented in real applications.

APPENDIX A

ILLUSTRATIONS

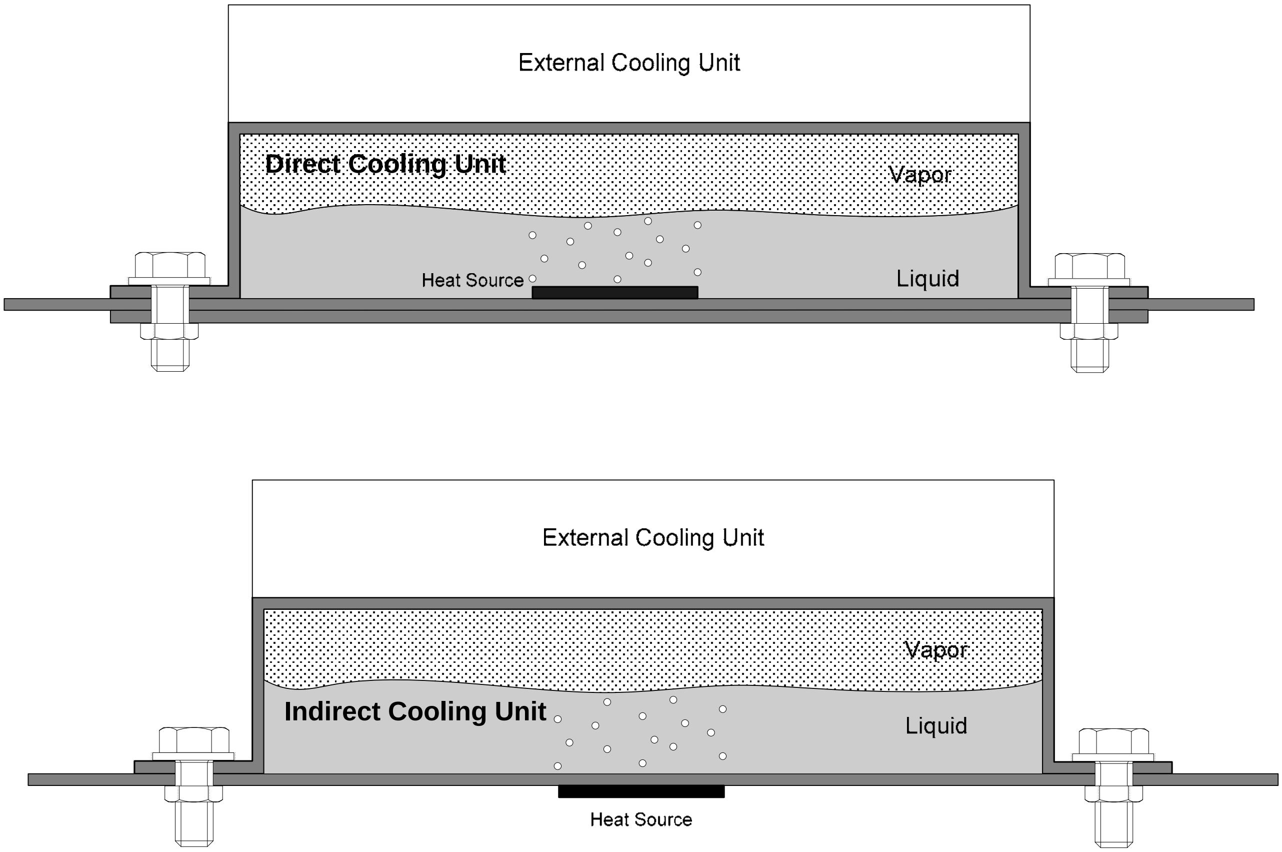

Figure A.1 Conceptual diagrams of two-phase cooling modules

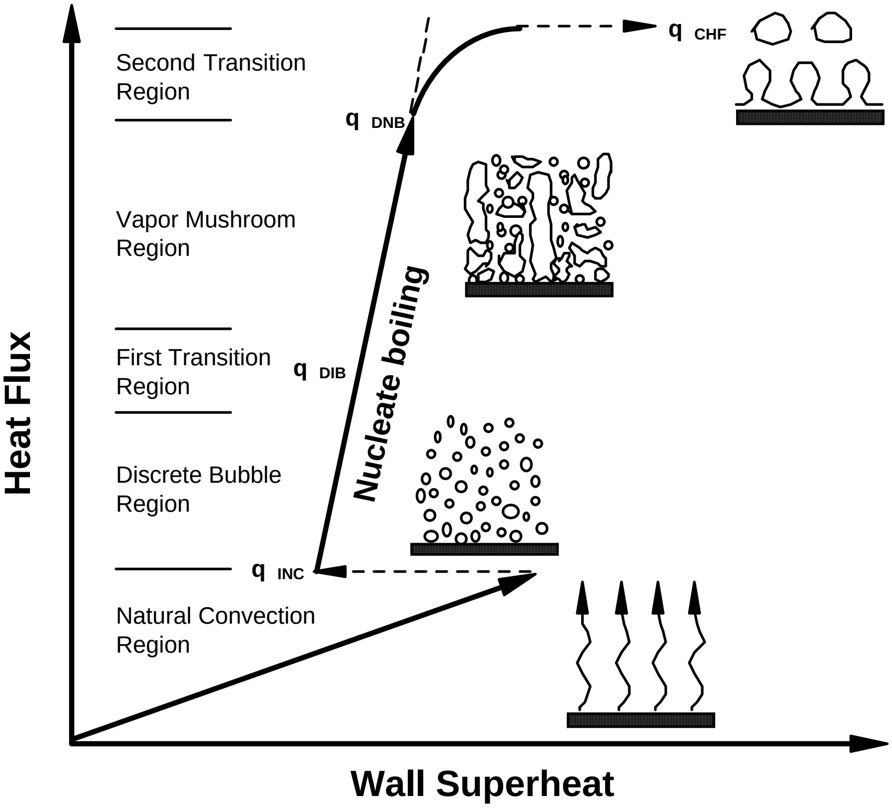

Figure A.2 Typical boiling curve

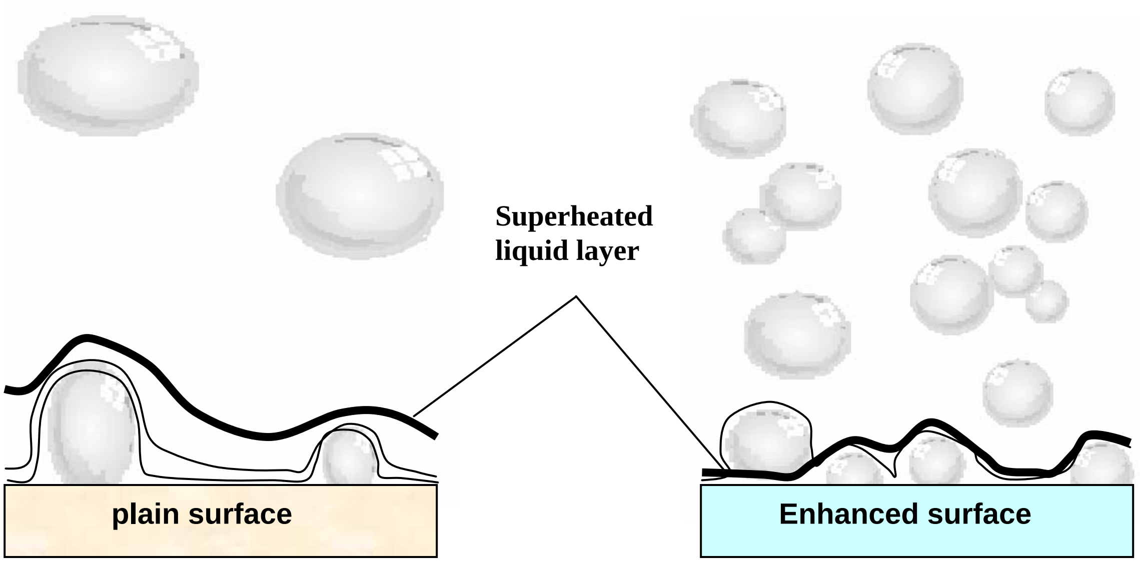

Figure A.3 Boiling enhancement mechanism

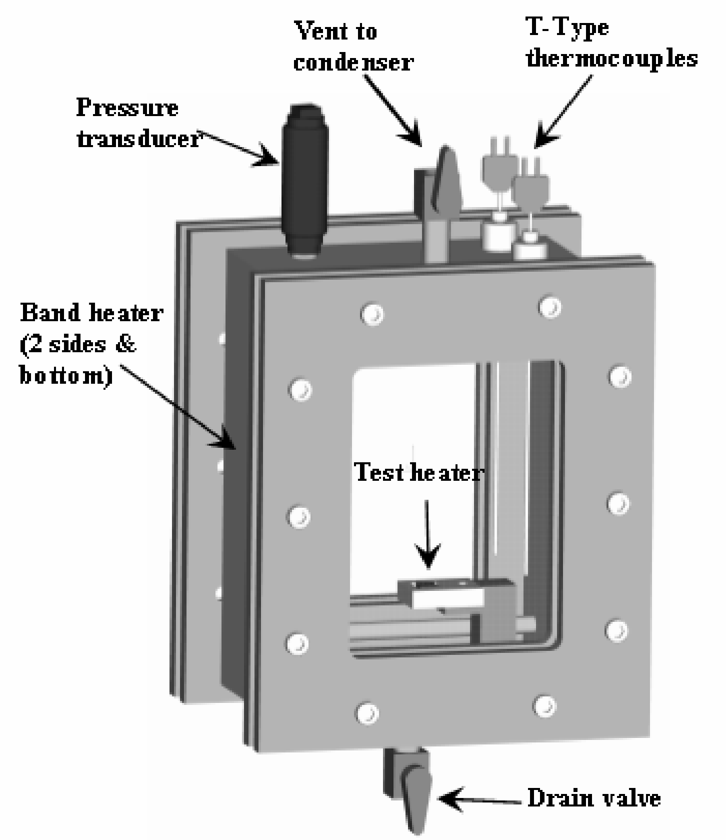

Figure A.4 Pool boiling test section

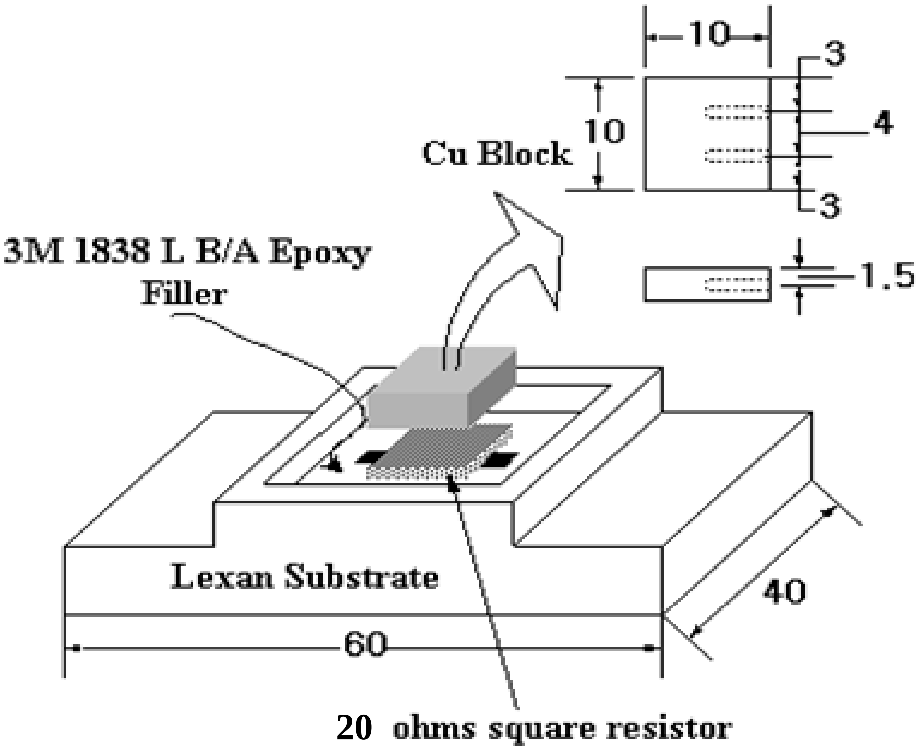

Figure A.5 Boiling teat heater assembly (1x1 cm)

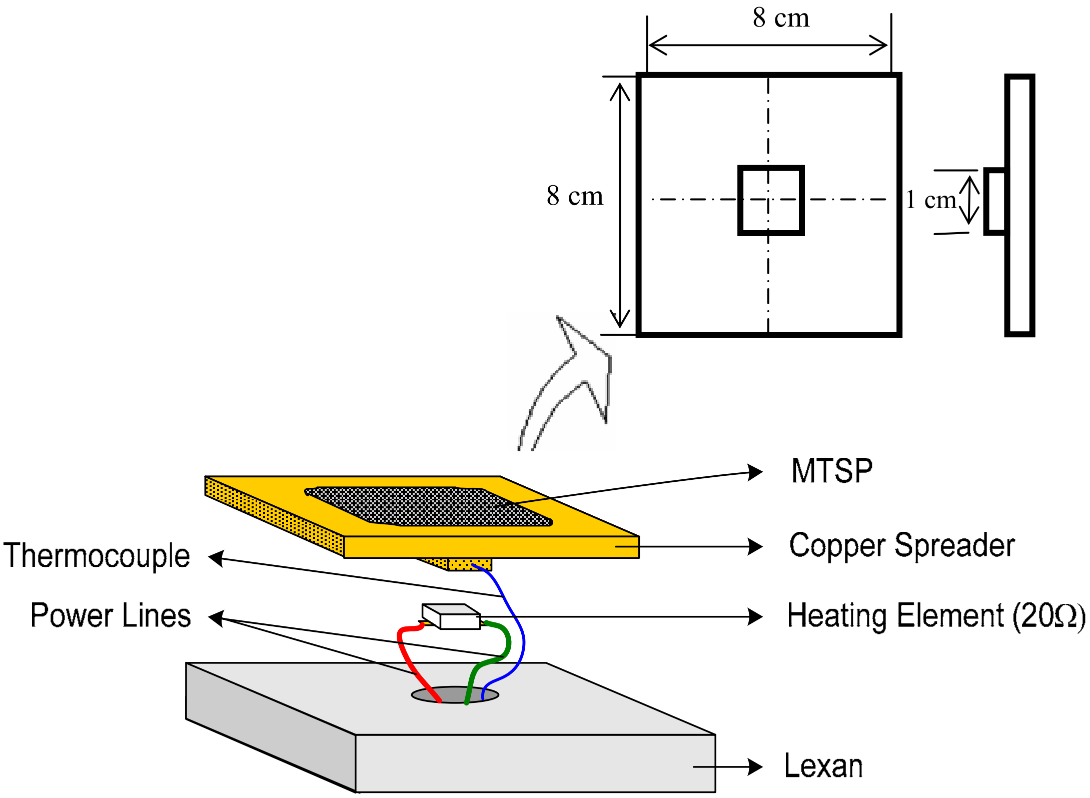

Figure A.6 Boiling teat heater assembly (with spreader)

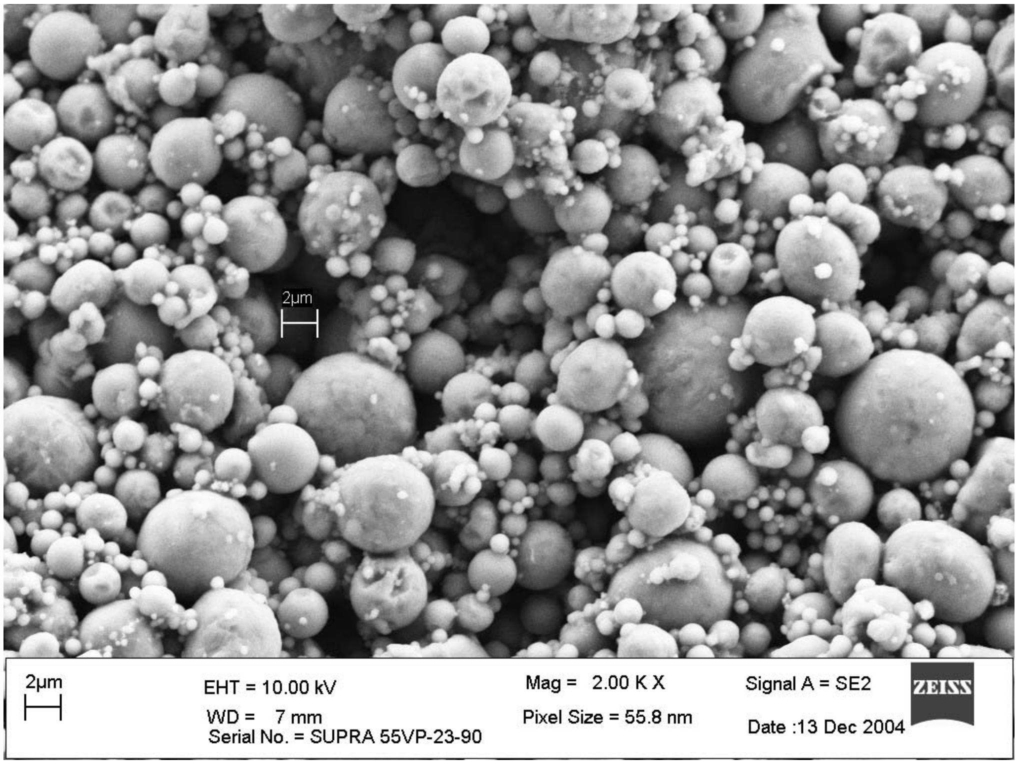

Figure A.7 SEM image of ABM coatings (3-4.5 µm)

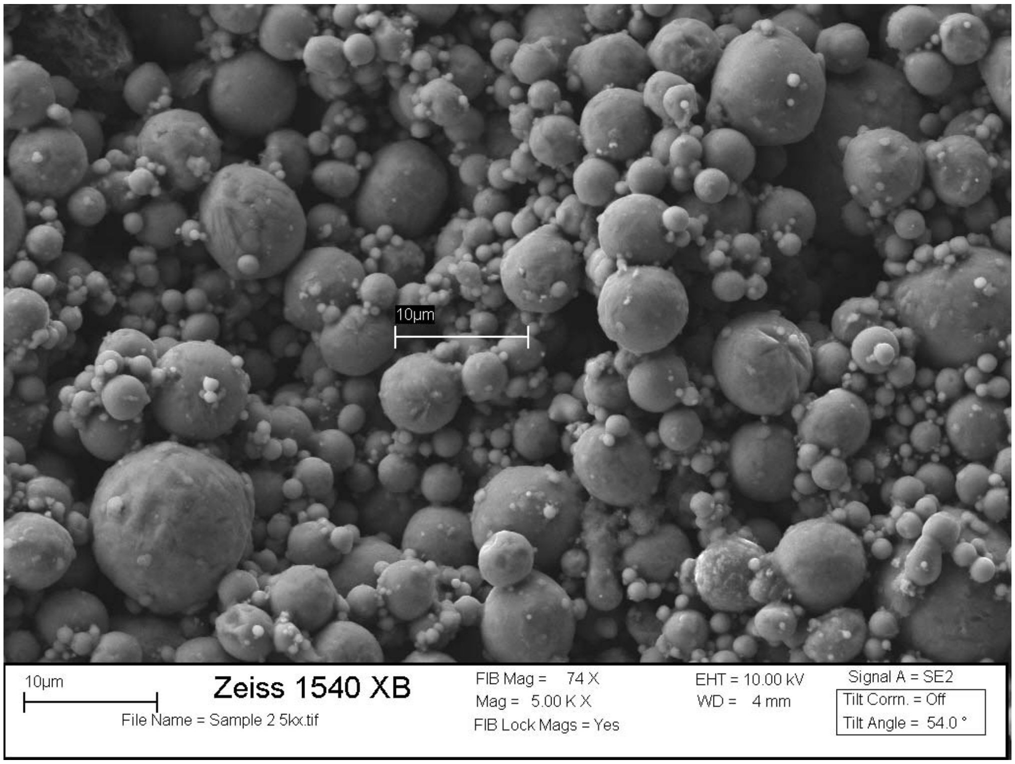

Figure A.8 SEM image of ABM coatings (4.5-10 µm)

Figure A.9 SEM image of ABM coatings (8-12 μm)

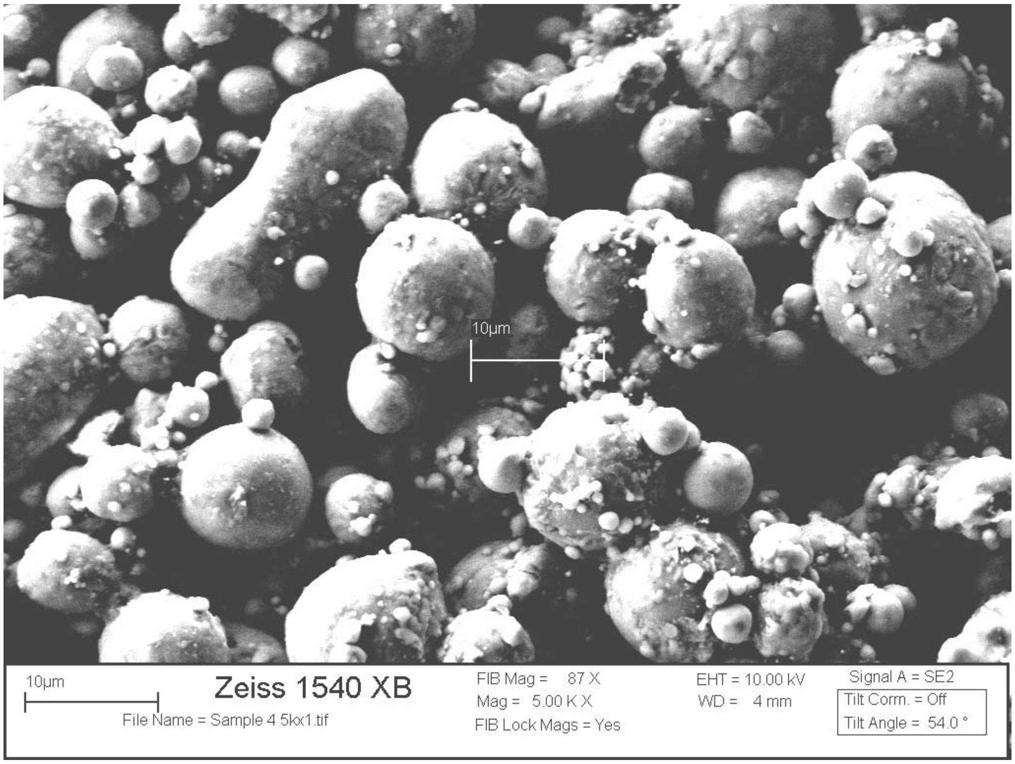

Figure A.10 SEM image of ABM coatings (10-14 µm)

Figure A.11 SEM image of ABM coatings (17-30 µm)

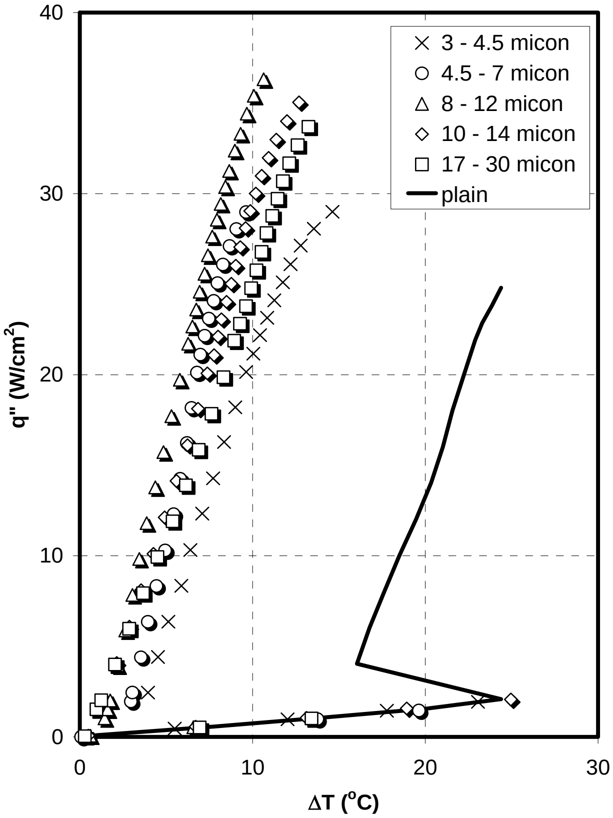

Figure A.12 Boiling curves of ABM coatings in saturated R-123 at atmospheric pressure

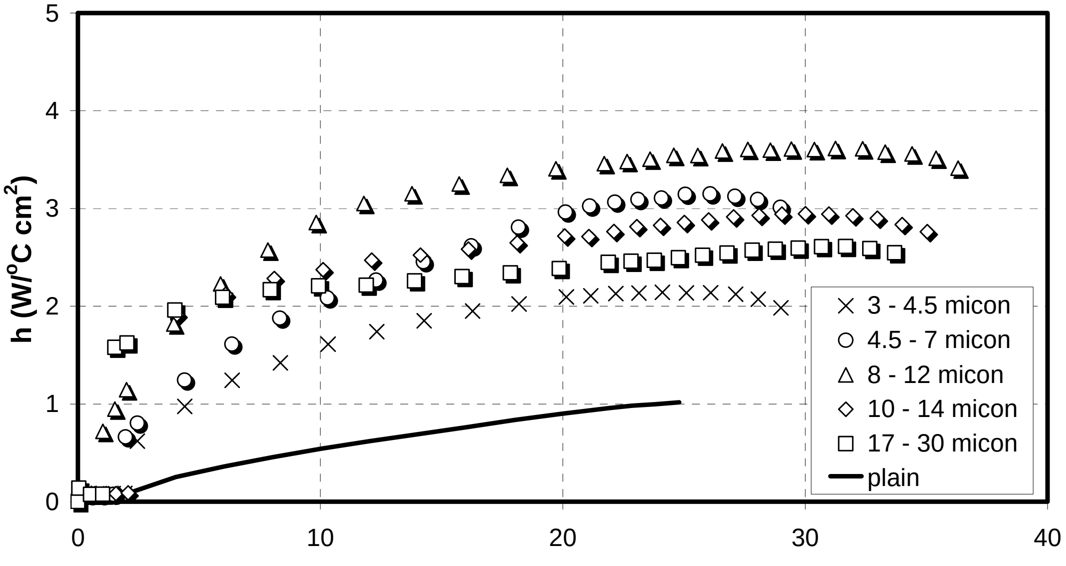

Figure A.13 Average boiling coefficient of ABM coatings in saturated R-123 at atmospheric pressure

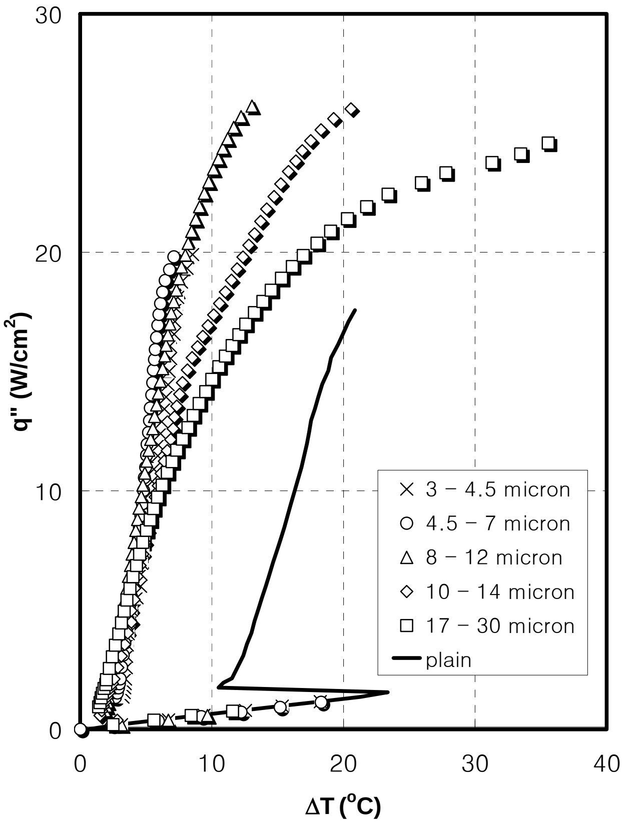

Figure A.14 Boiling curves of ABM coatings in saturated FC-72 at atmospheric pressure

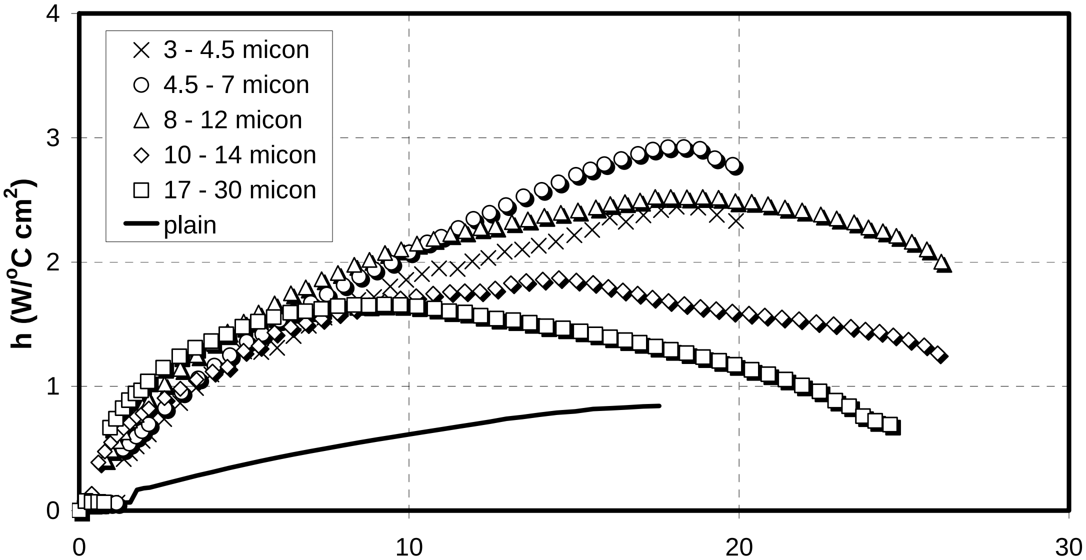

Figure A.15 Average boiling coefficient of ABM coatings in saturated FC-72 at atmospheric pressure

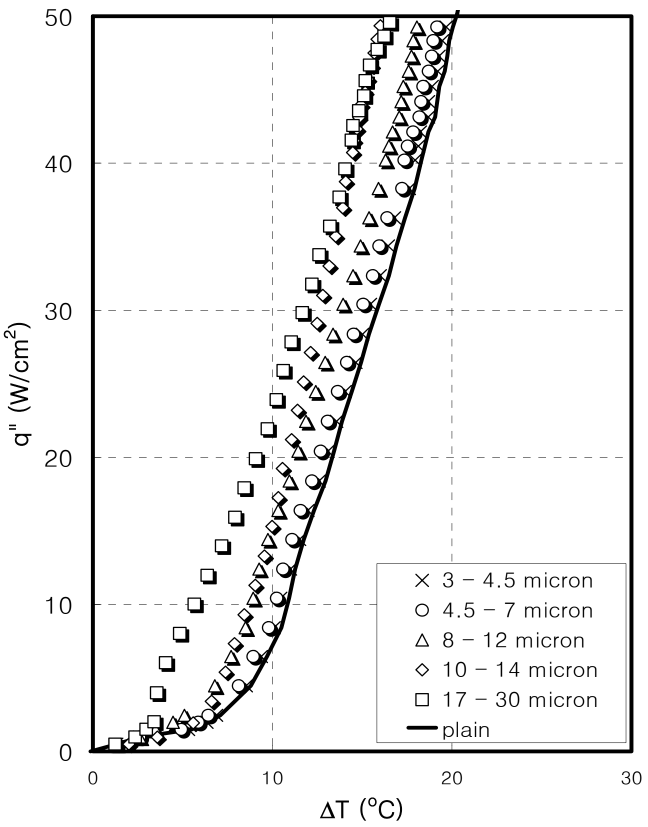

Figure A.16 Boiling curves of ABM coatings in saturated water at atmospheric pressure

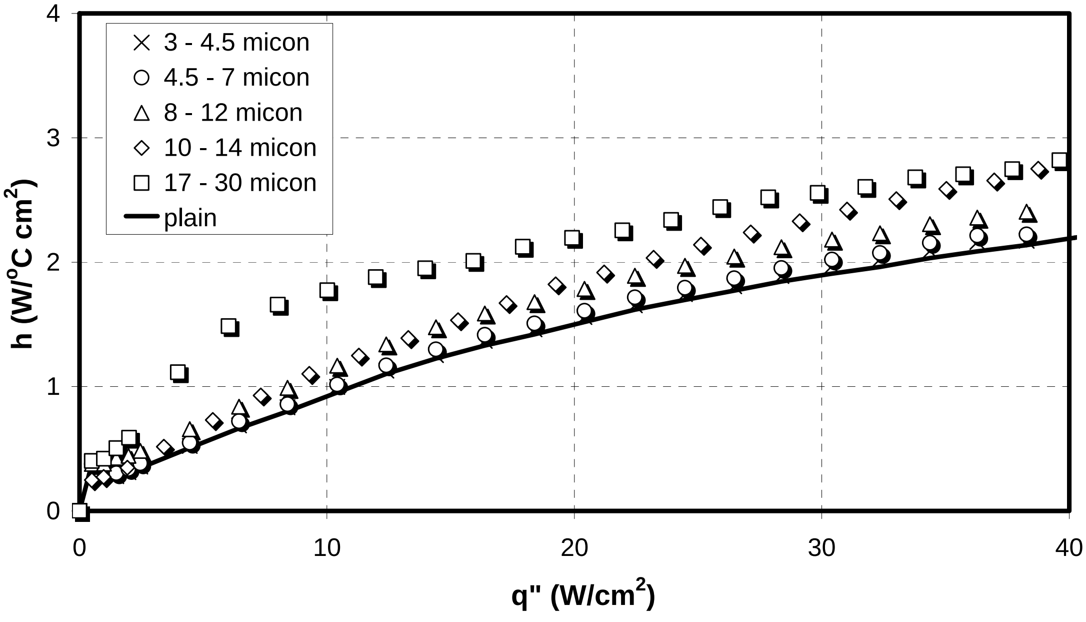

Figure A.17 Average boiling coefficient of ABM coatings in saturated water at atmospheric pressure

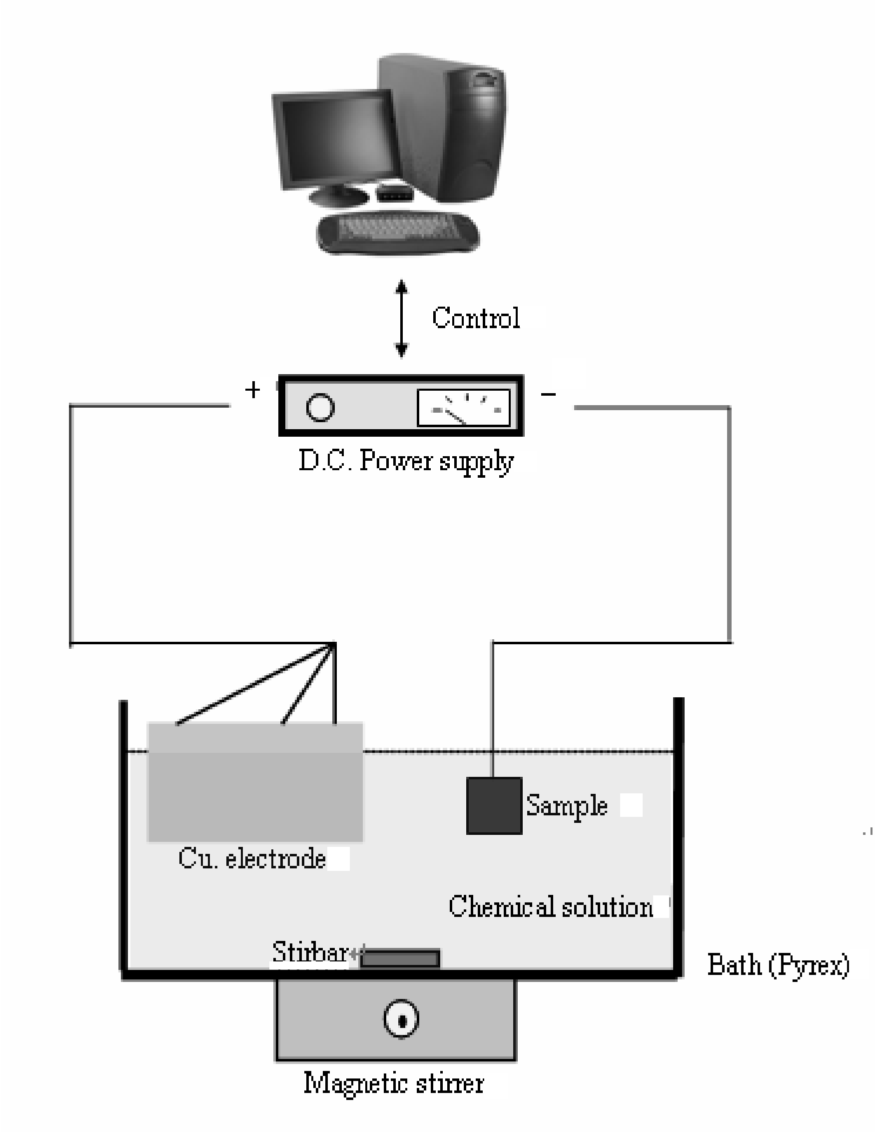

Figure A.18 Diagram of electroplating process

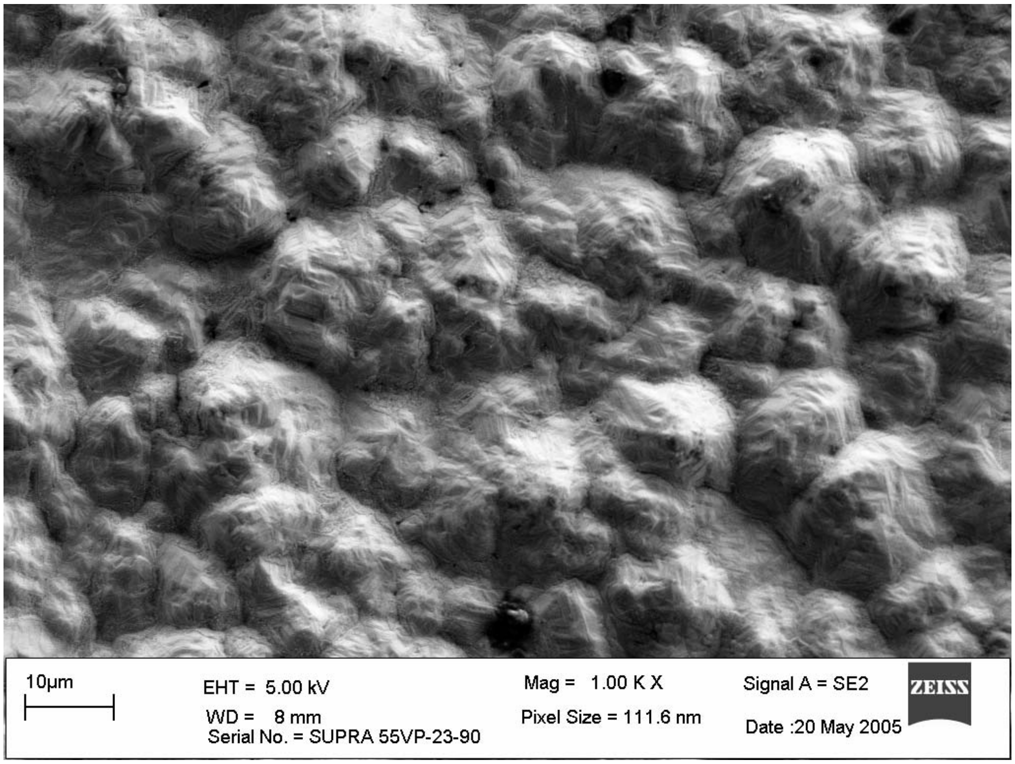

Figure A.19 SEM image of MSE coatings (0.166 Ampere/cm^2)

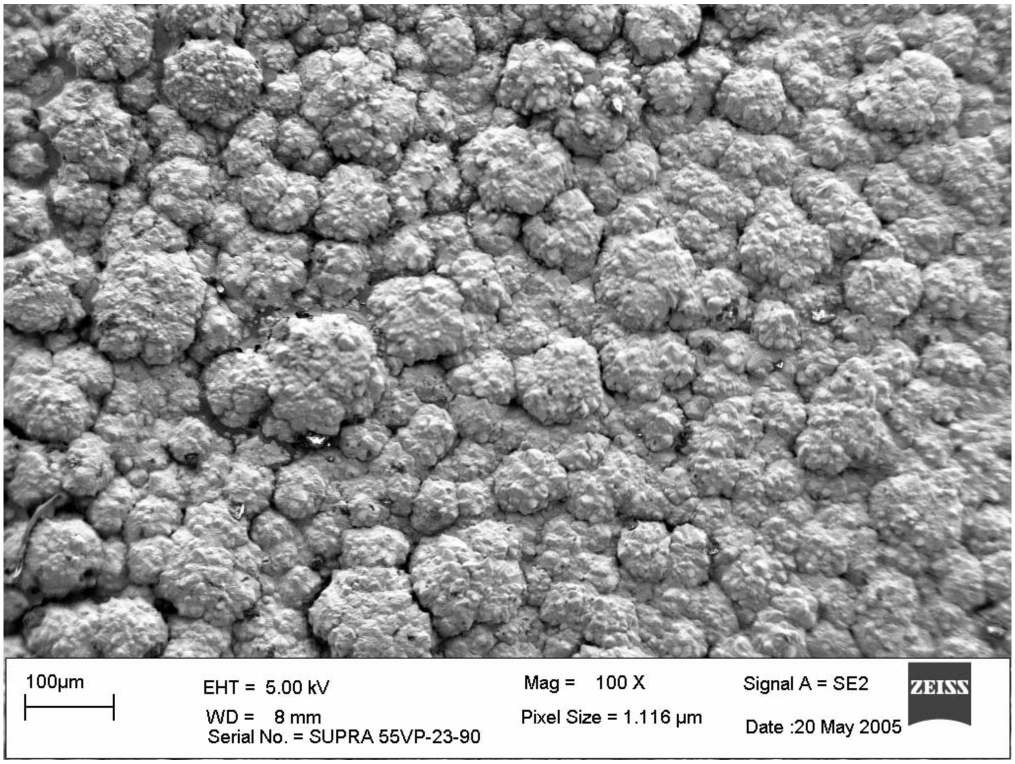

Figure A.20 SEM image of MSE coatings (0.25 Ampere/cm^2)

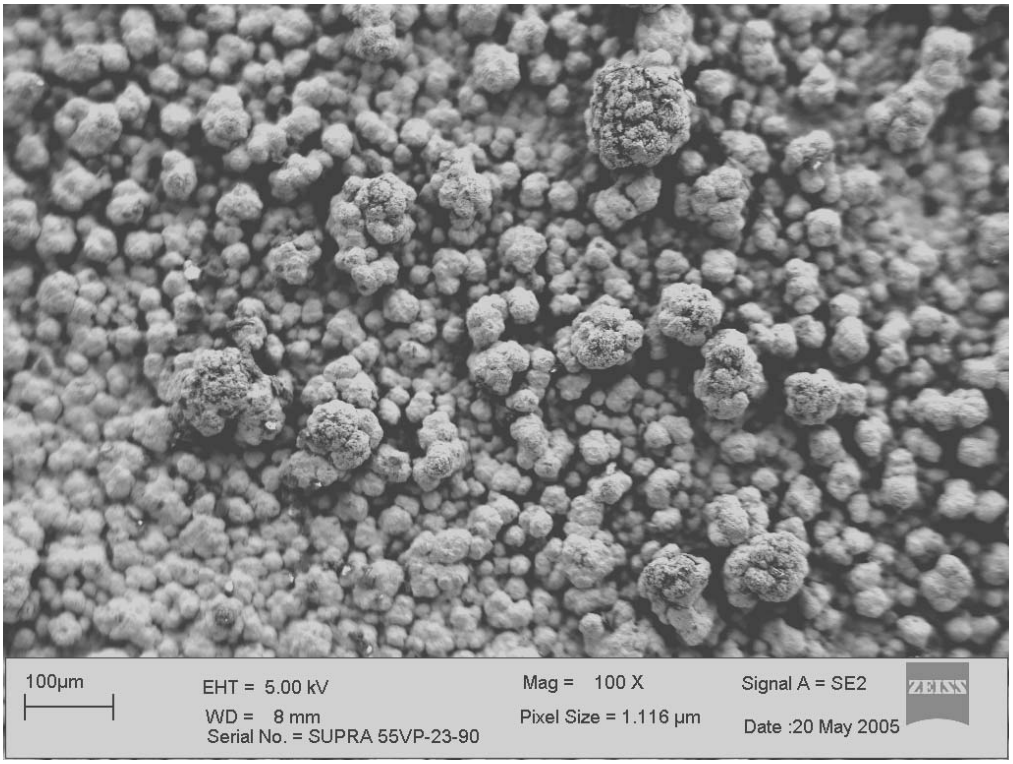

Figure A.21 SEM image of MSE coatings (0.33 Ampere/cm^2)

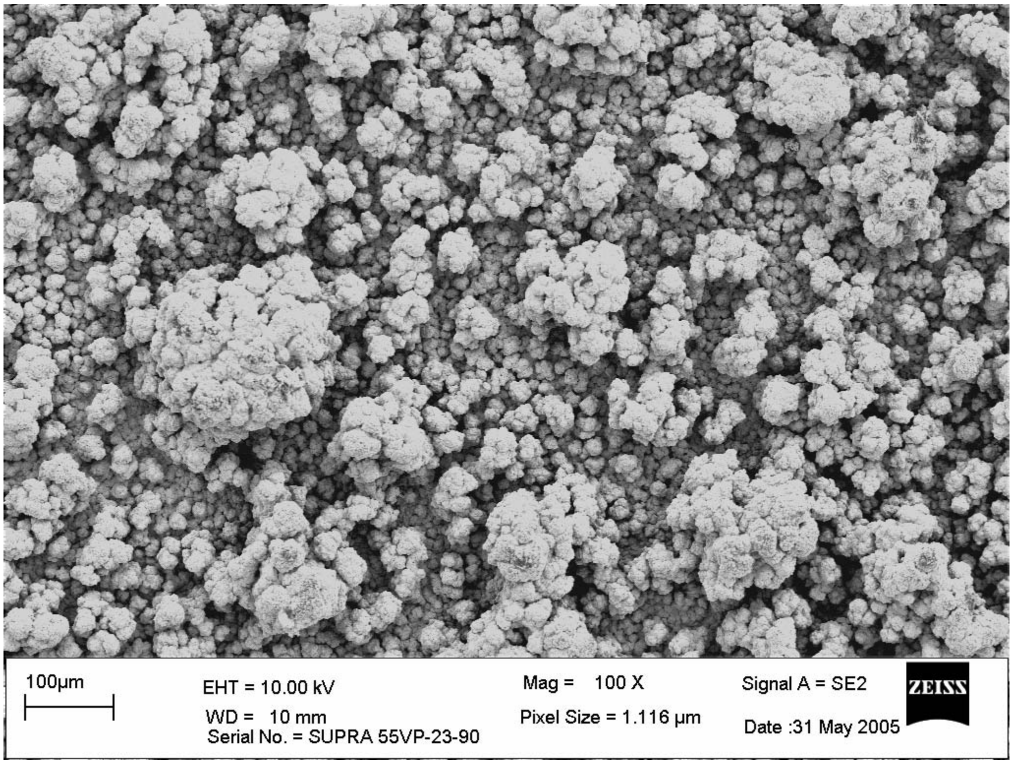

Figure A.22 SEM image of MSE coatings (0.5 Ampere/cm^2)

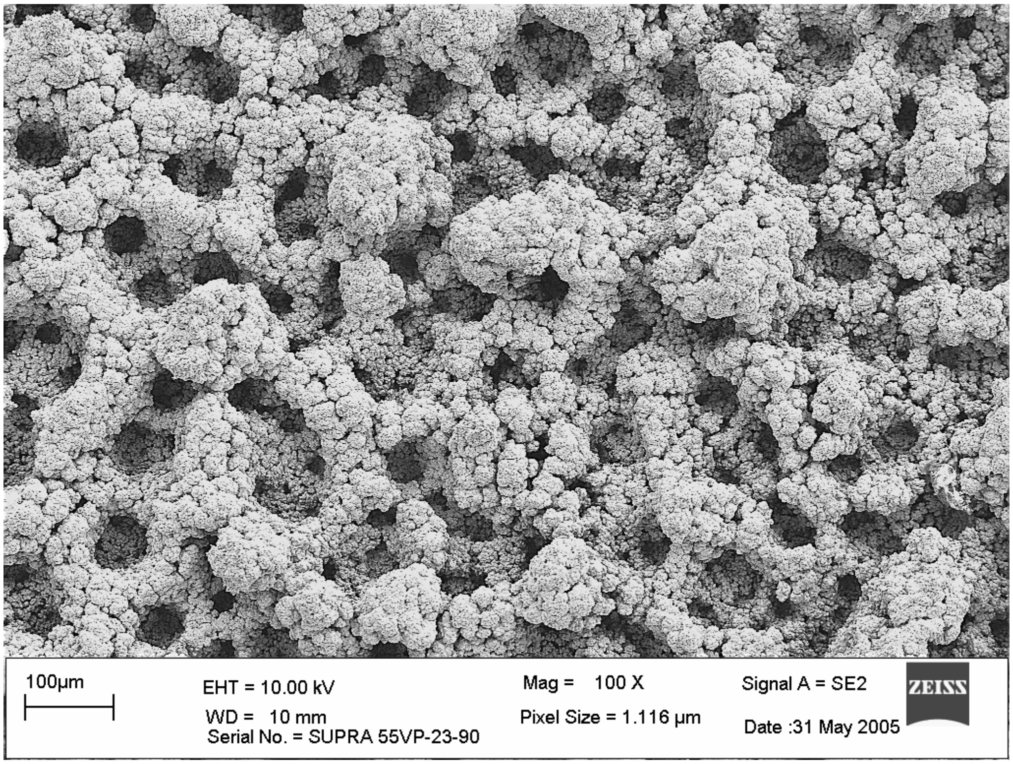

Figure A.23 SEM image of MSE coatings (1.0 Ampere/cm^2)

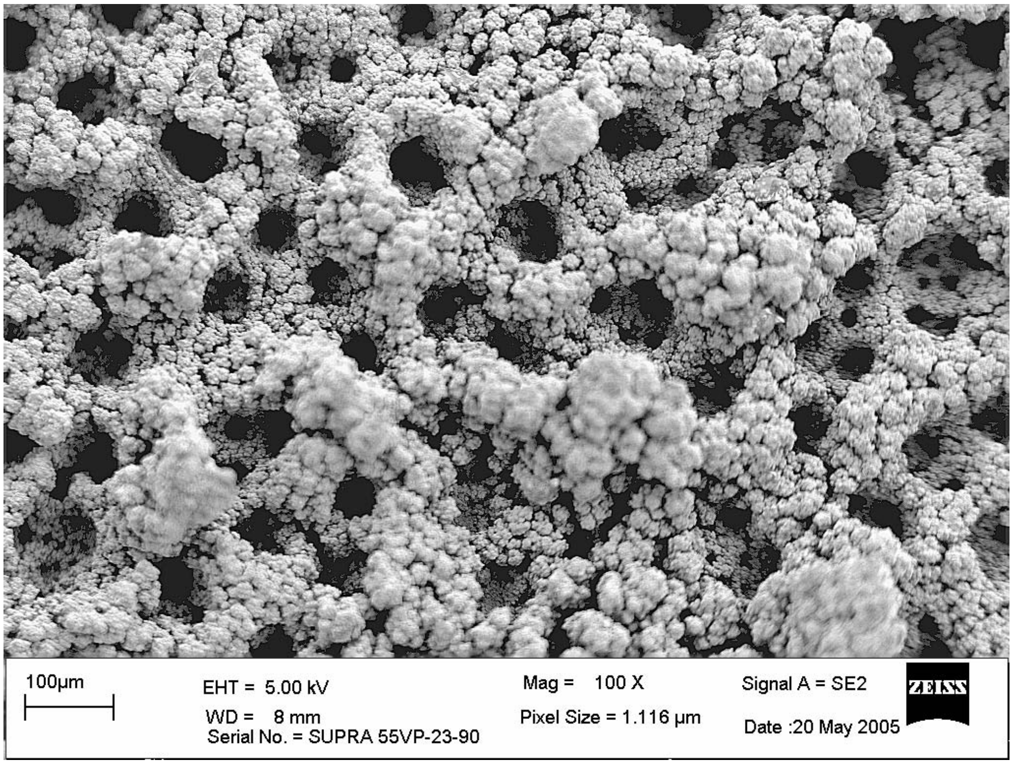

Figure A.24 SEM image of MSE coatings (1.2 Ampere/cm^2)

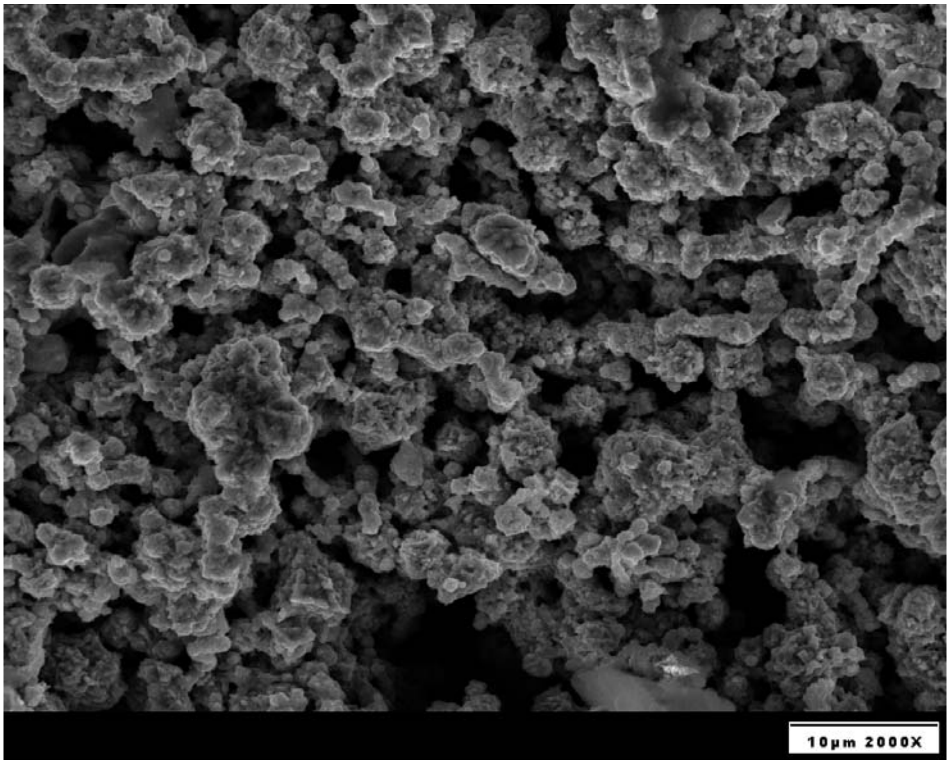

Figure A.25 SEM image of MTSP coatings (-325 mesh)

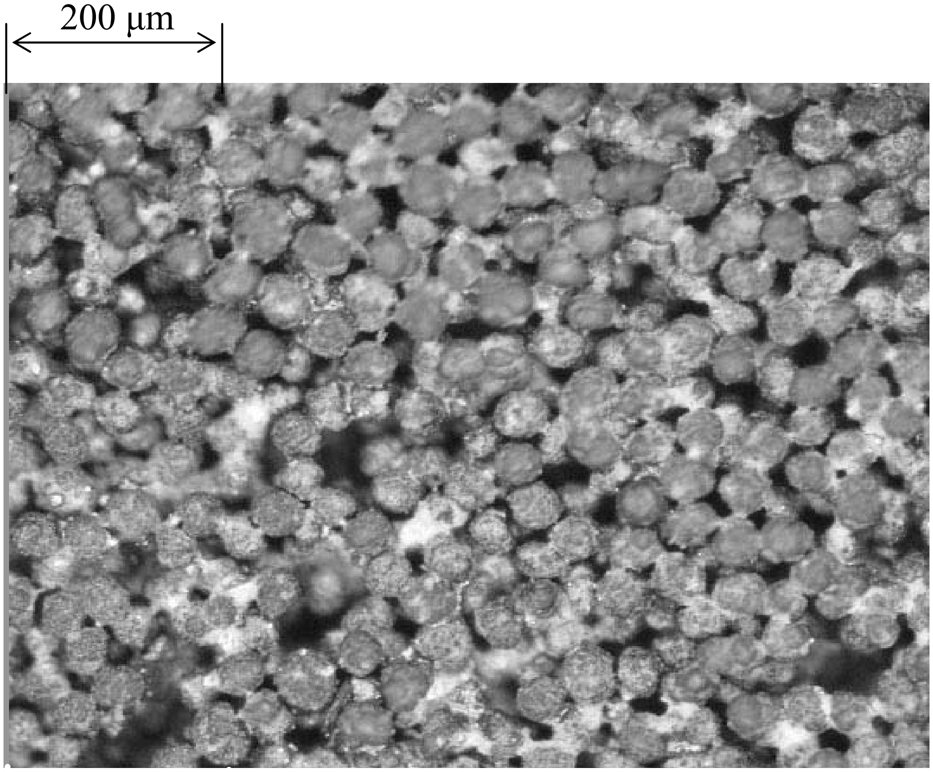

Figure A.26 Microscopic image of MTSP coatings (-100+325 mesh)

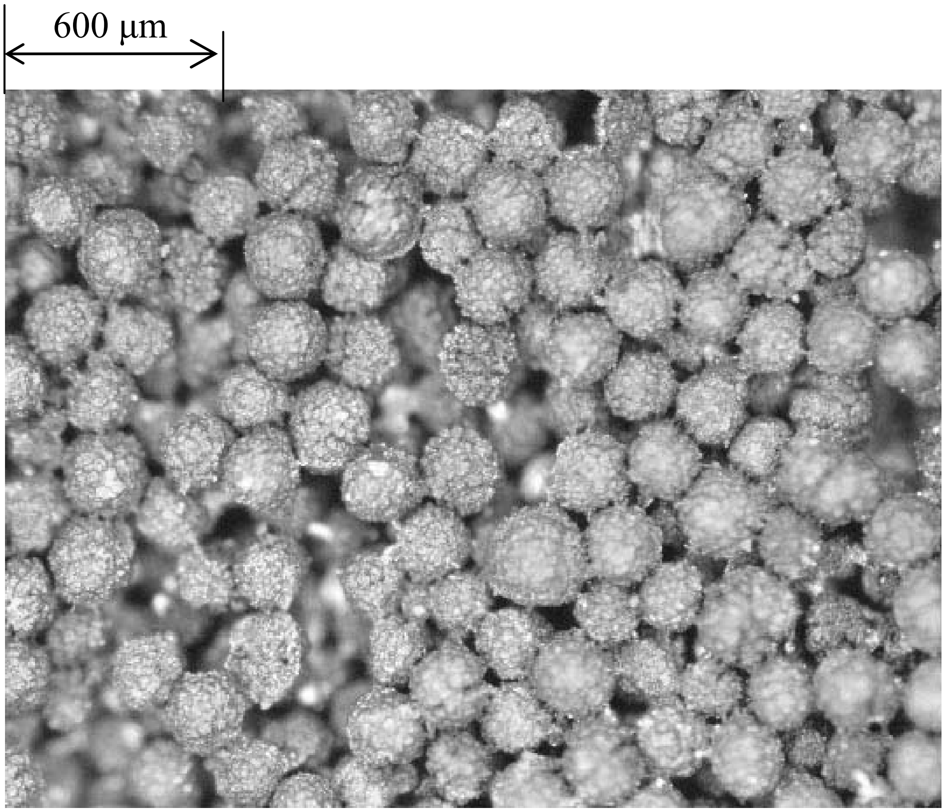

Figure A.27 Microscopic image of MTSP coatings (-50+100 mesh)

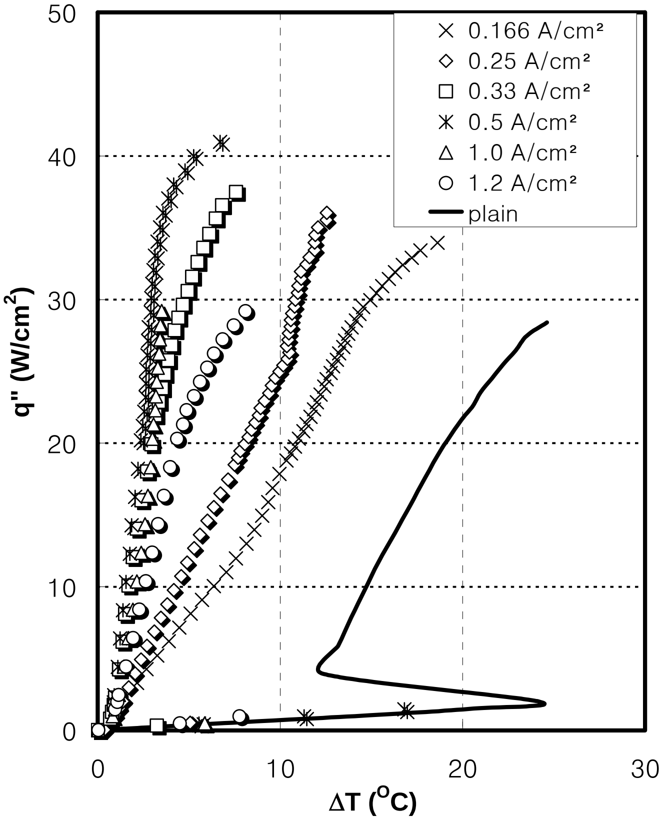

Figure A.28 Boiling curves of MSE coatings in saturated R-123 at atmospheric pressure

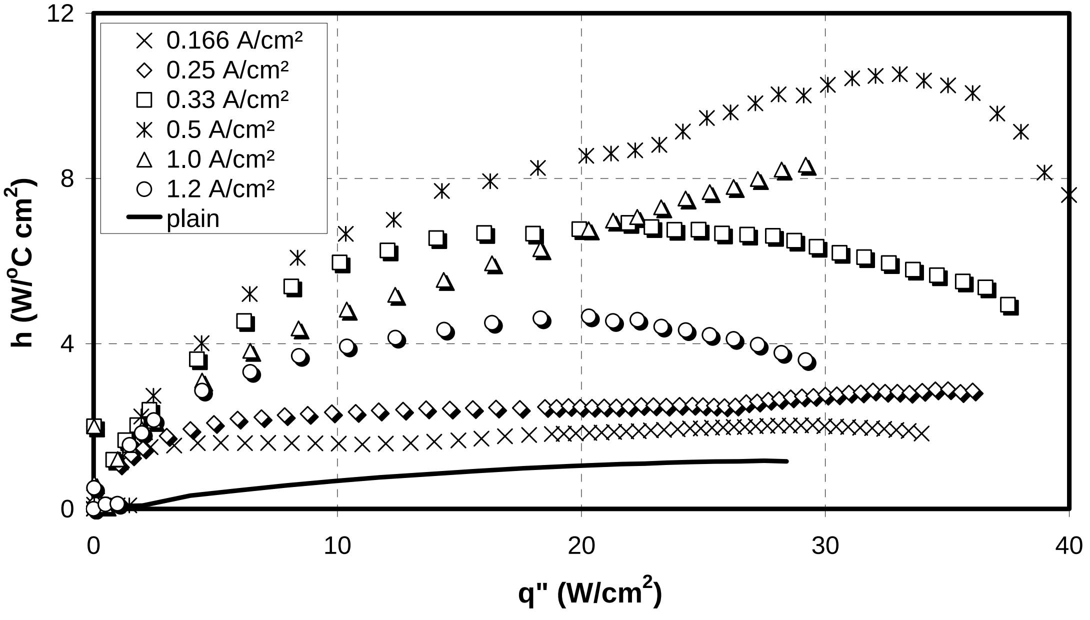

Figure A.29 Average boiling coefficient of MSE coatings in saturated R-123 at atmospheric pressure

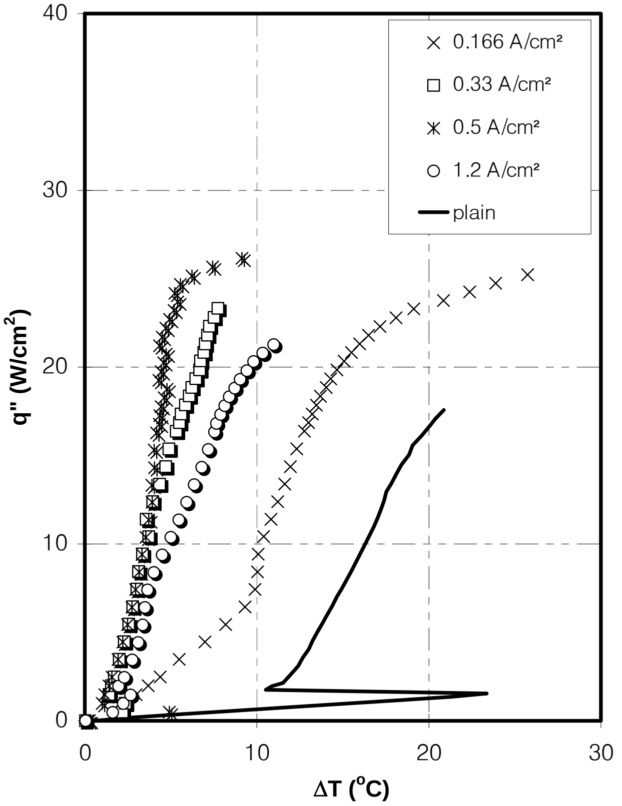

Figure A.30 Boiling curves of MSE coatings in saturated FC-72 at atmospheric pressure

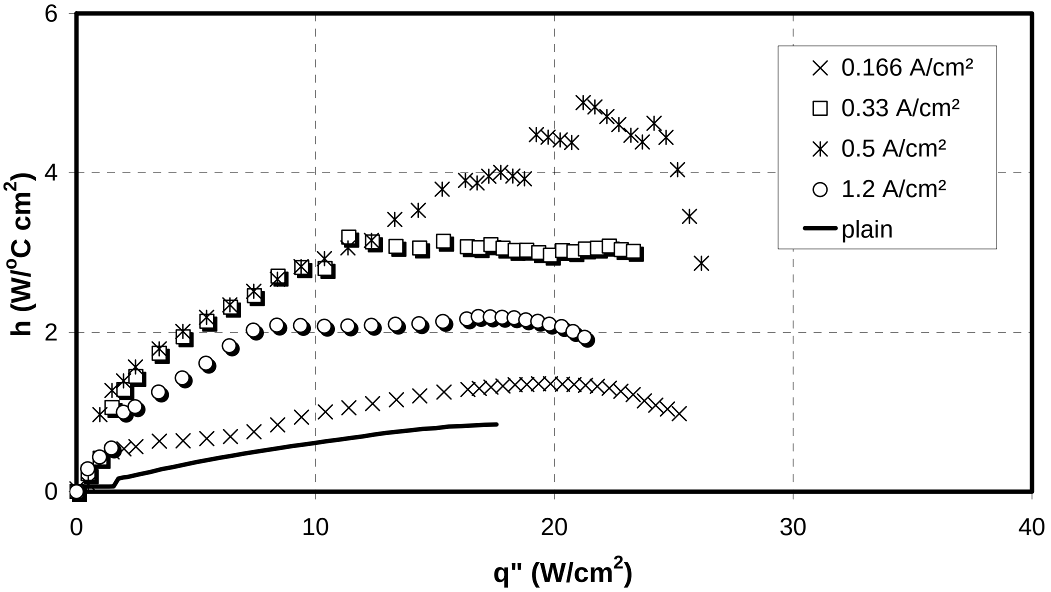

Figure A.31 Average boiling coefficient of MSE coatings in saturated FC-72 at atmospheric pressure

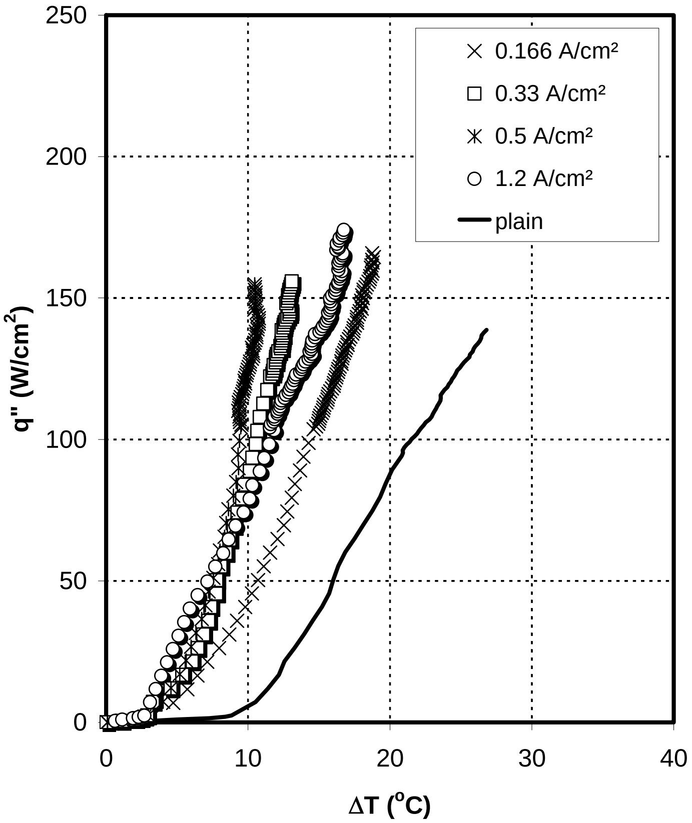

Figure A.32 Boiling curves of MSE coatings in saturated water at atmospheric pressure

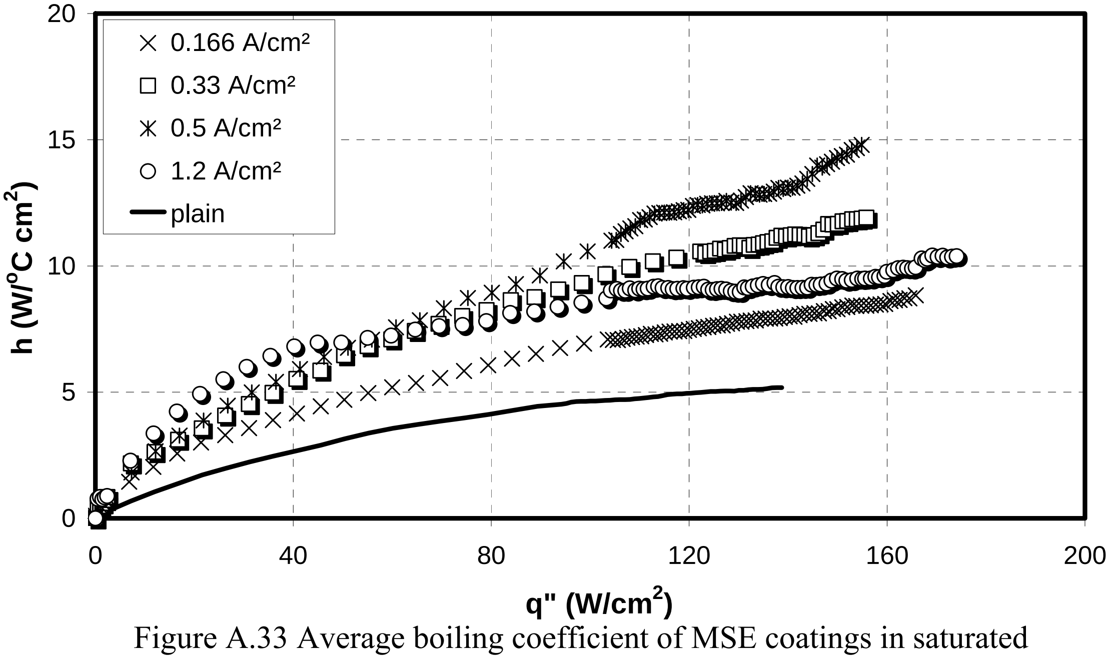

Figure A.33 Average boiling coefficient of MSE coatings in saturated water at atmospheric pressure

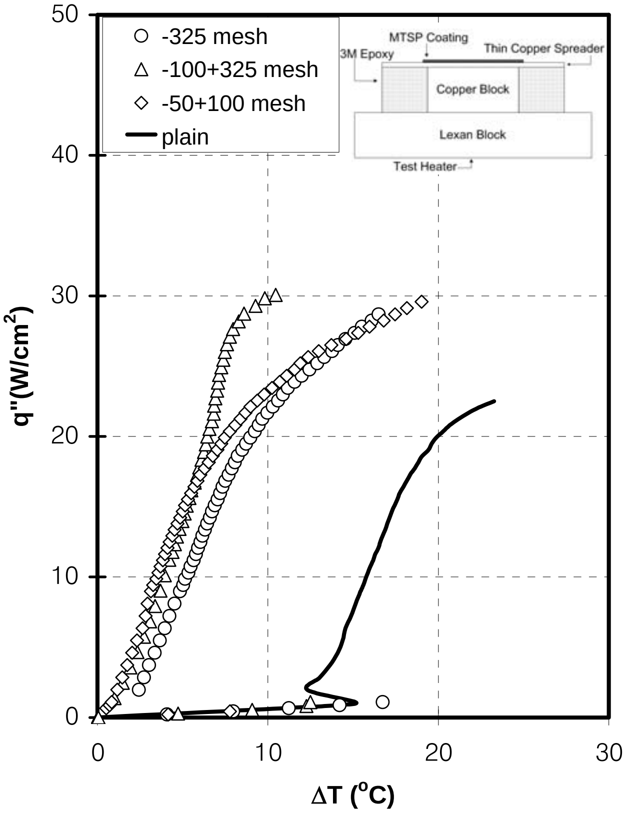

Figure A.34 Boiling curves of MTSP coatings in saturated R-123 at atmospheric pressure

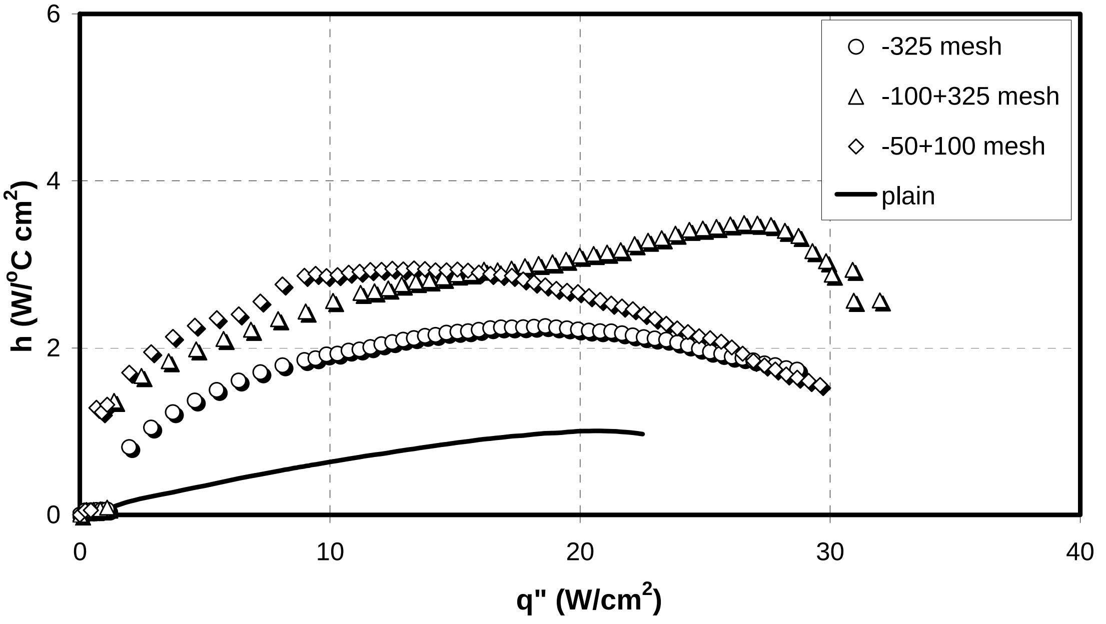

Figure A.35 Average boiling coefficient of MTSP coatings in saturated R-123 at atmospheric pressure

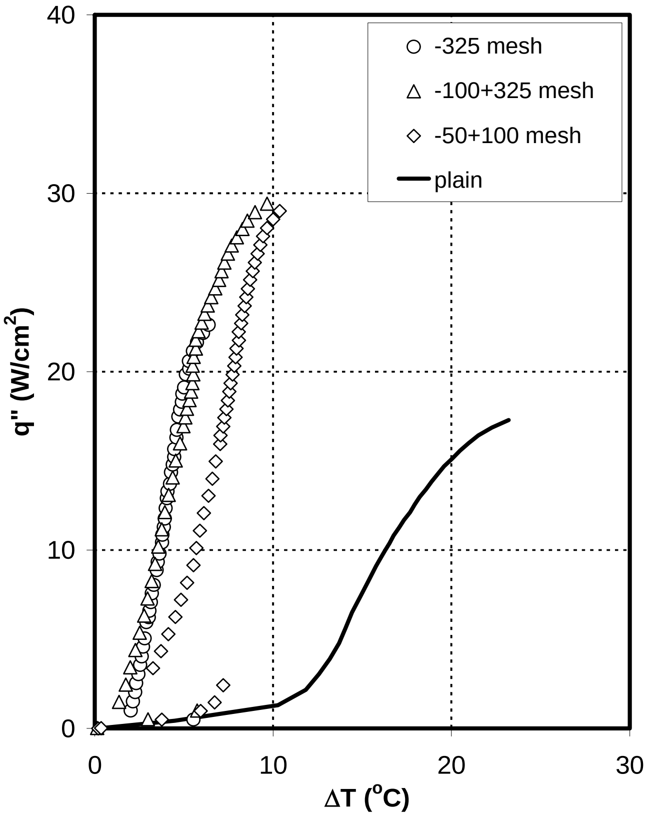

Figure A.36 Boiling curves of MTSP coatings in saturated FC-72 at atmospheric pressure

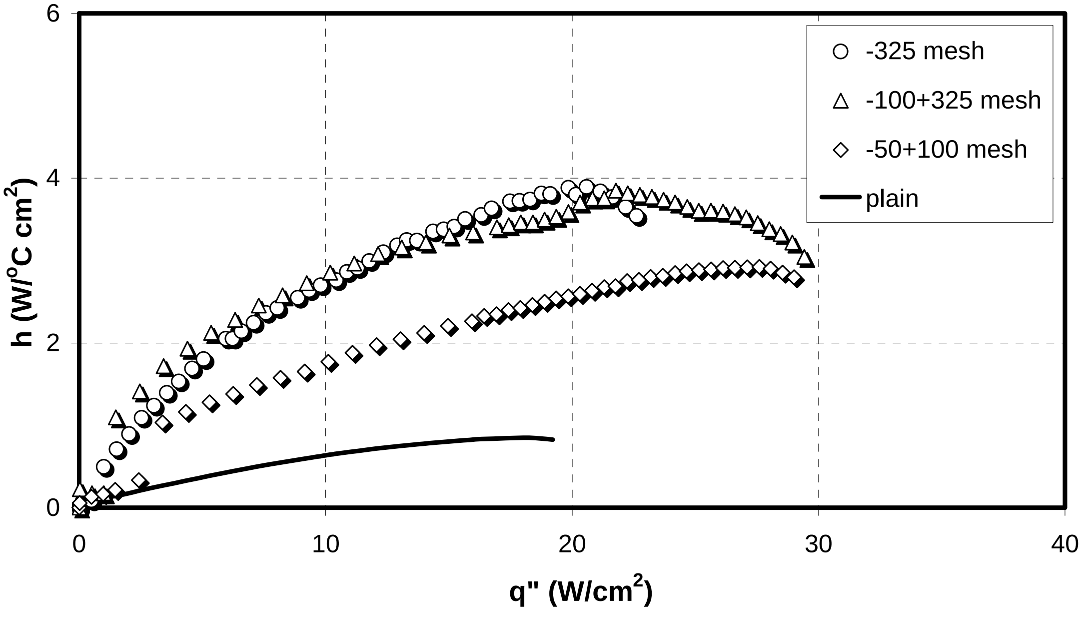

Figure A.37 Average boiling coefficient of MTSP coatings in saturated FC-72 at atmospheric pressure

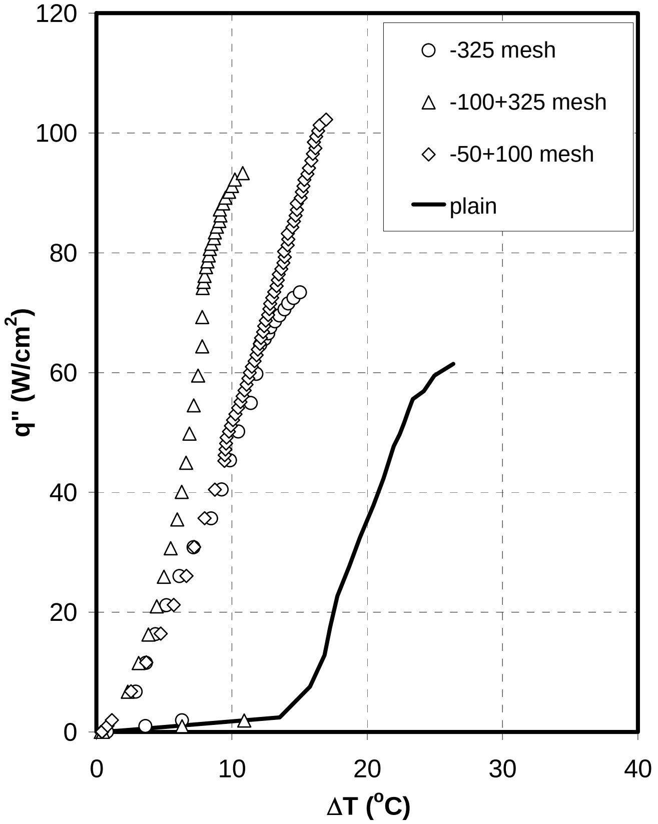

Figure A.38 Boiling curves of MTSP coatings in saturated methanol at atmospheric pressure

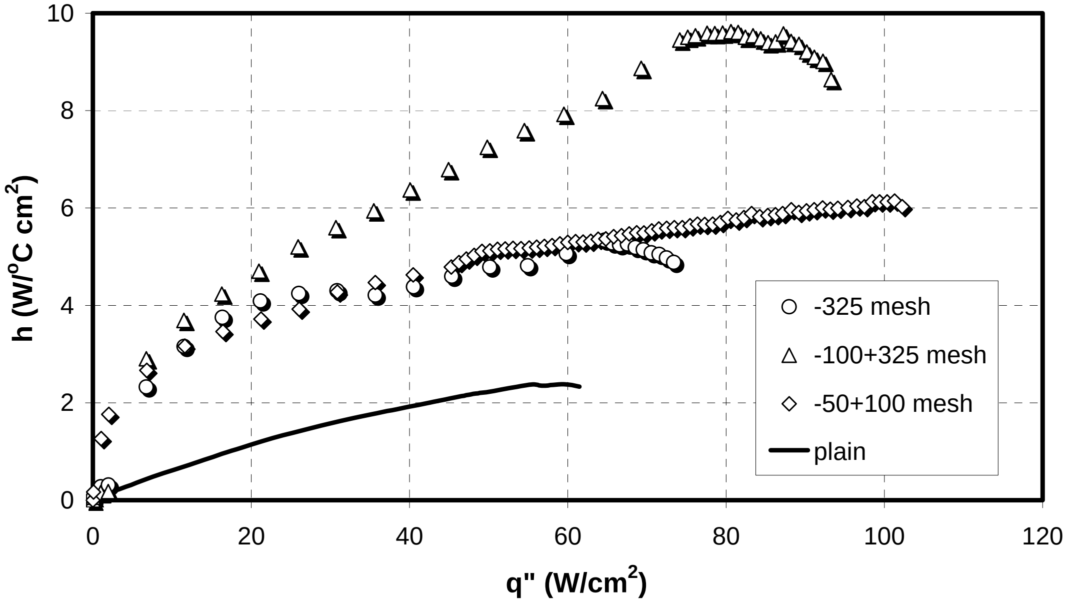

Figure A.39 Average boiling coefficient of MTSP coatings in saturated methanol at atmospheric pressure

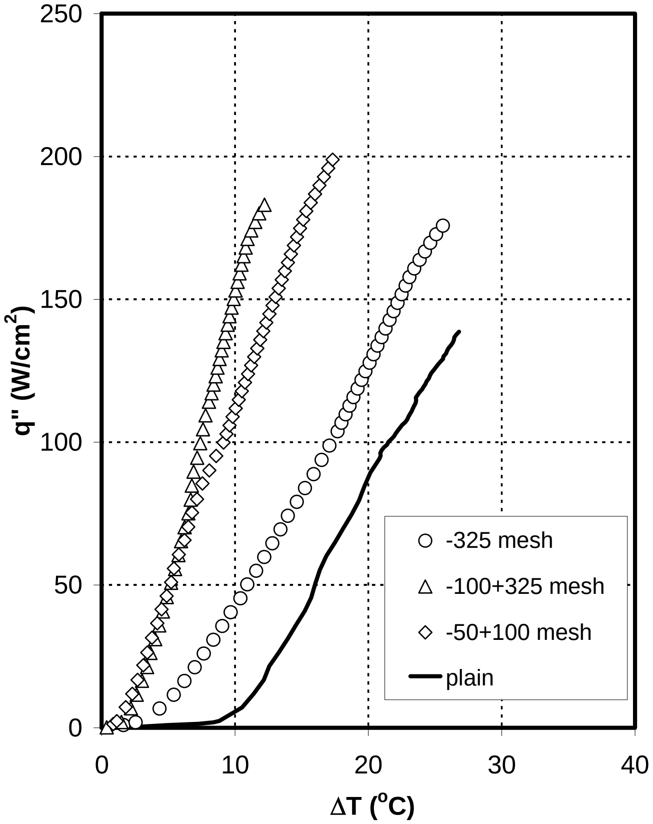

Figure A.40 Boiling curves of MTSP coatings in saturated water at atmospheric pressure

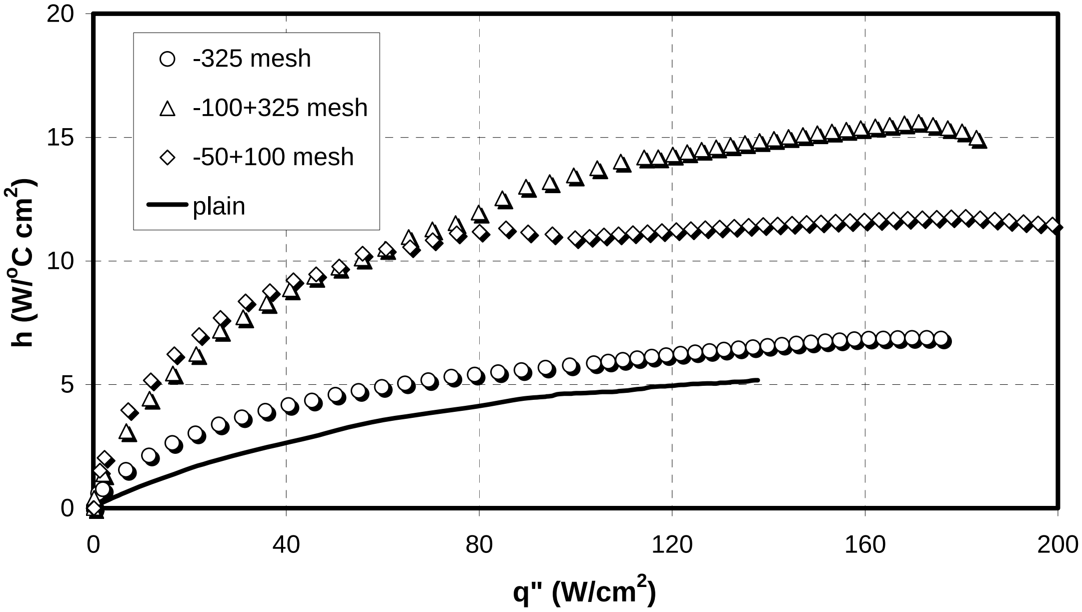

Figure A.41 Average boiling coefficient of MTSP coatings in saturated water at atmospheric pressure

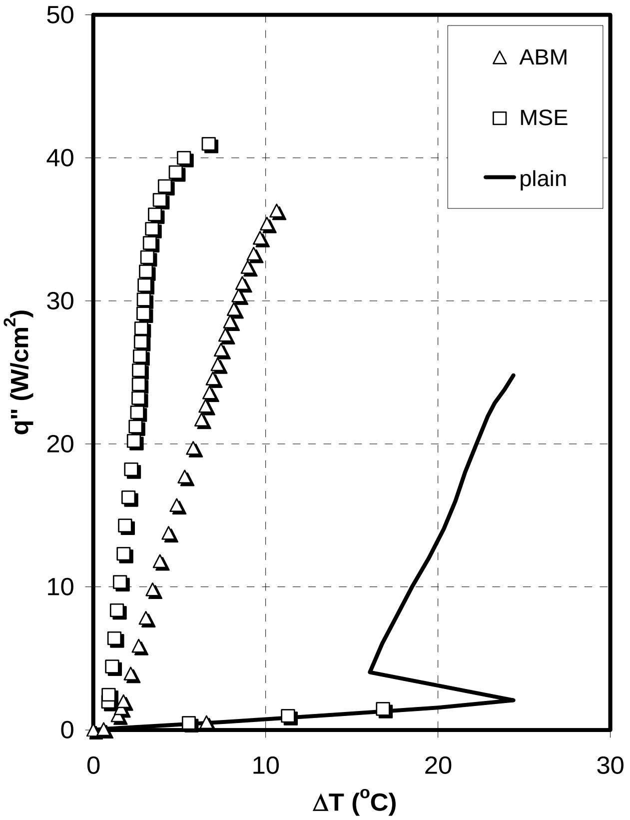

Figure A.42 Boiling performance comparison of microporous coatings in saturated R-123

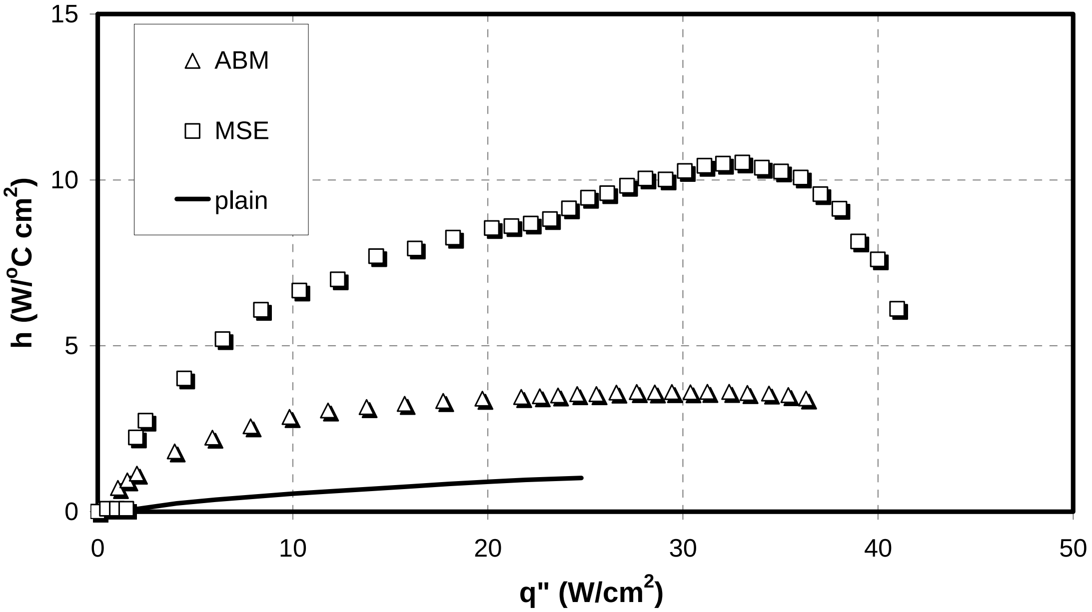

Figure A.43 Boiling coefficient comparison of microporous coatings in saturated R-123

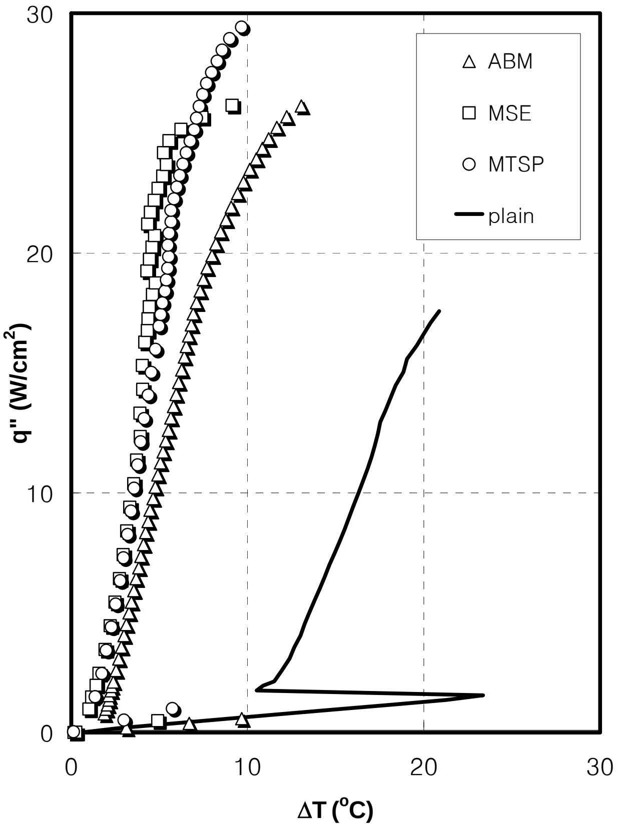

Figure A.44 Boiling performance comparison of microporous coatings in saturated FC-72

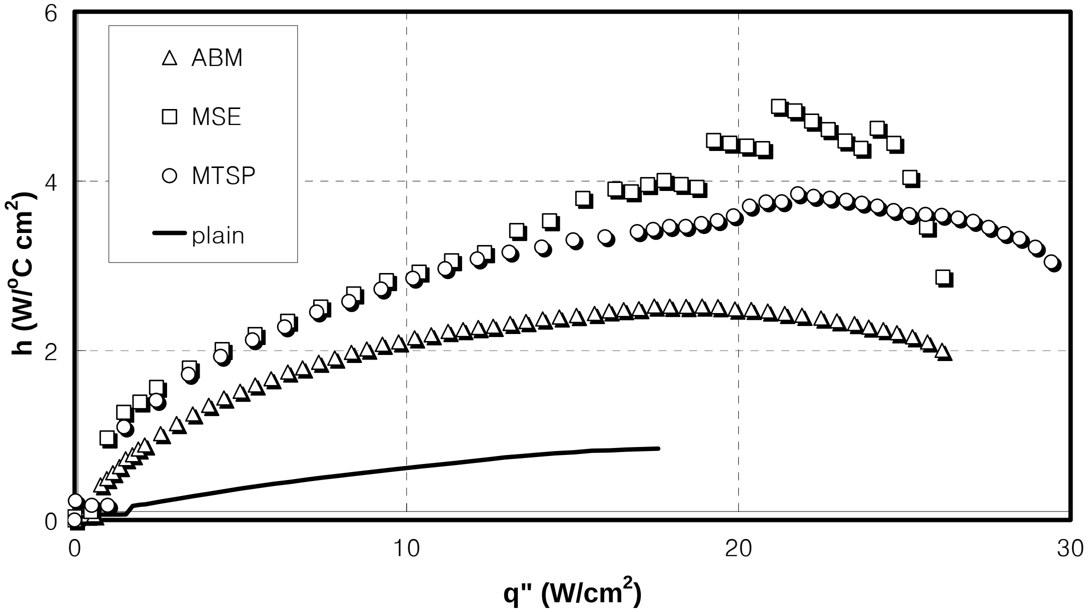

Figure A.45 Boiling coefficient comparison of microporous coatings in saturated FC-72

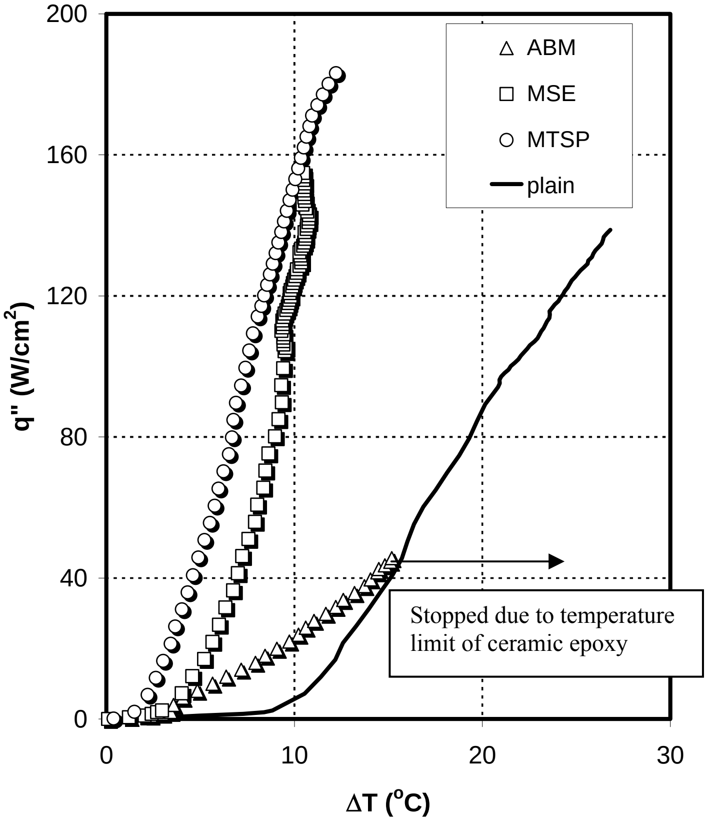

Figure A.46 Boiling performance comparison of microporous coatings in saturated water

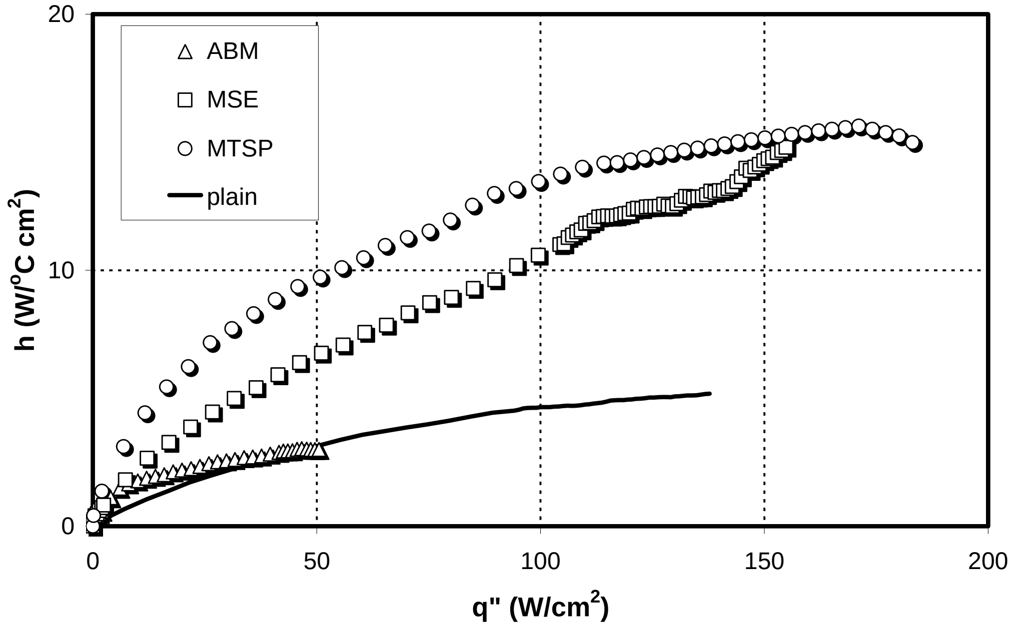

Figure A.47 Boiling coefficient comparison of microporous coatings in saturated water

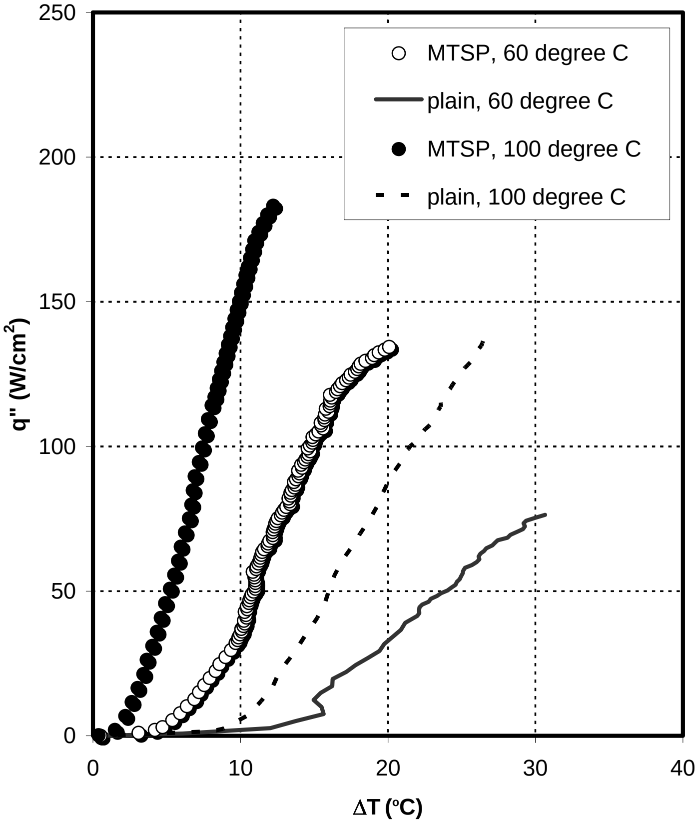

Figure A.48 Boiling curves of MTSP coatings in saturated water at 60°C saturation temperature (P_{sat} = 20 kPa)

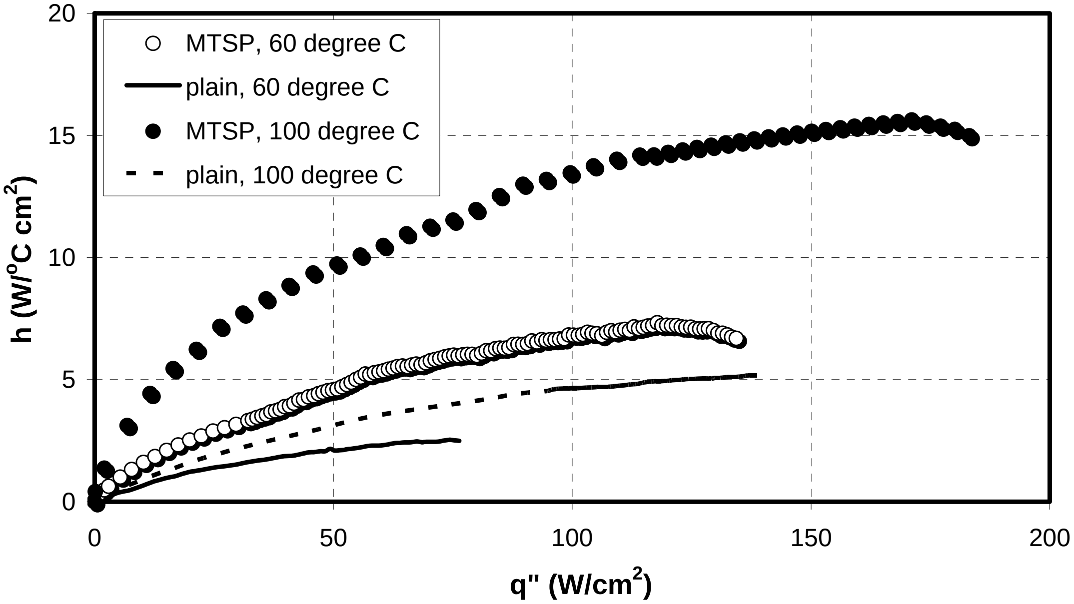

Figure A.49 Boiling coefficient of MTSP coatings in saturated water at 60°C saturation temperature (P_{sat} = 20 kPa)

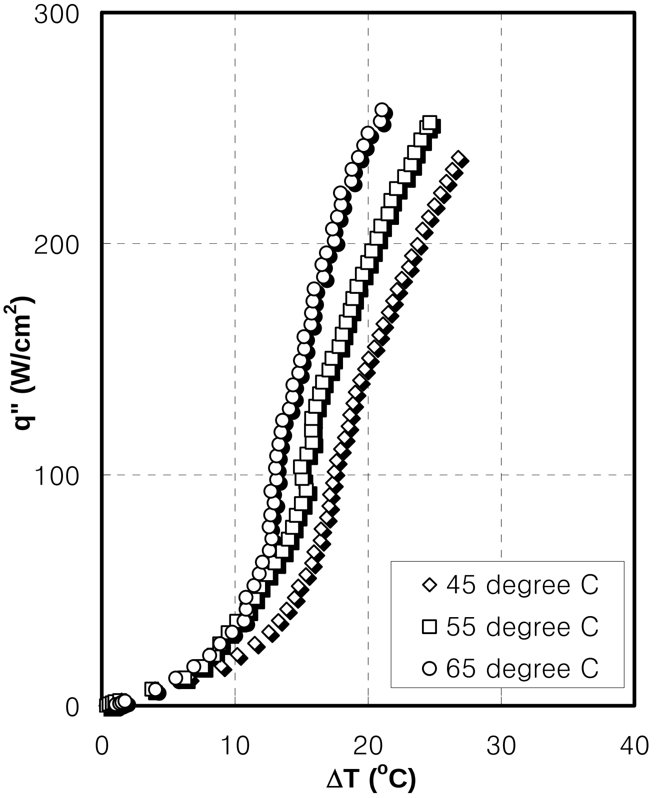

Figure A.50 Boiling curves of MTSP coating with spreader (t = 1.5 mm) in saturated water at different temperatures (45, 55, and 65 °C)

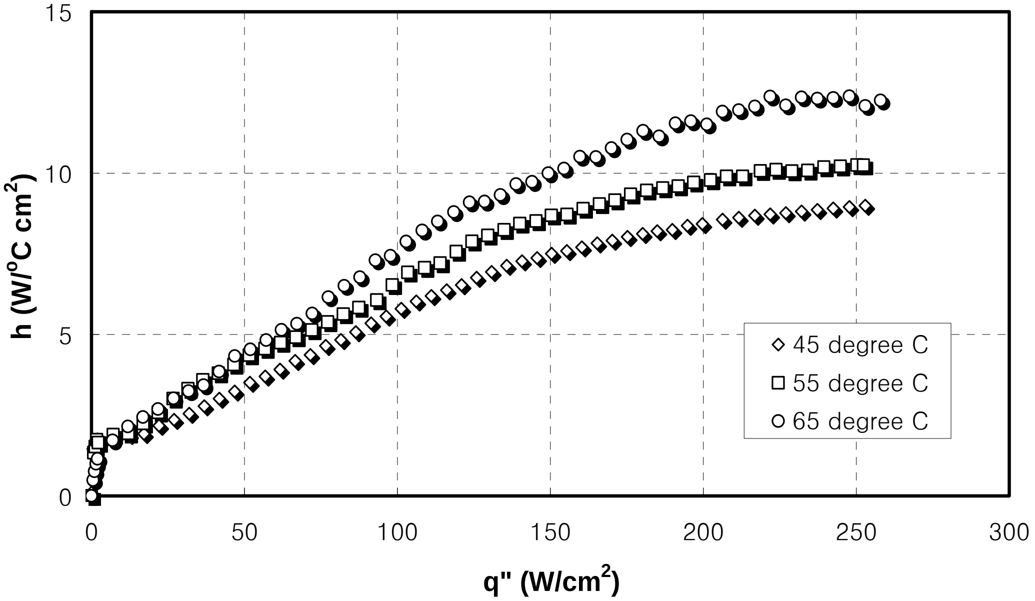

Figure A.51 Boiling coefficient of MTSP coating with spreader (t = 1.5 mm) in saturated water at different temperatures (45, 55, and 65 °C)

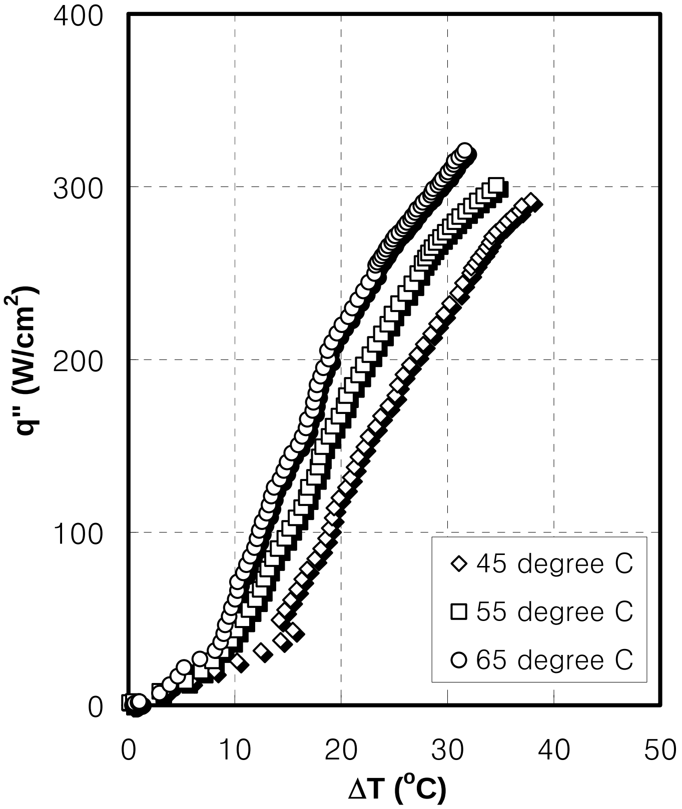

Figure A.52 Boiling curves of MTSP coating with spreader (t = 2.5 mm) in saturated water at different temperatures (45, 55, and 65 °C)

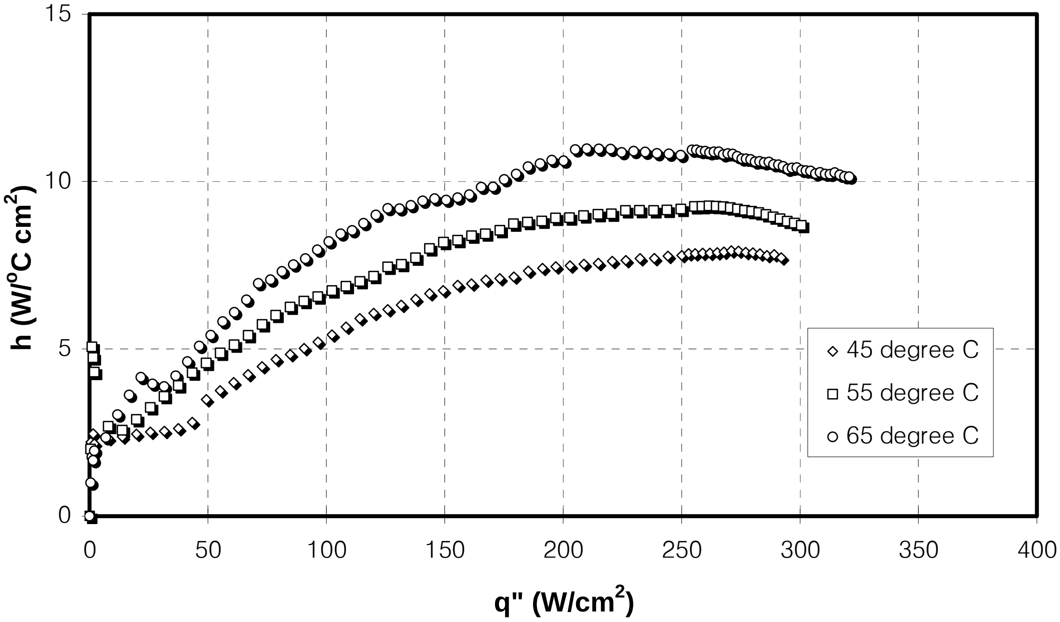

Figure A.53 Boiling coefficient of MTSP coating with spreader (t = 2.5 mm) in saturated water at different temperatures (45, 55, and 65 °C)

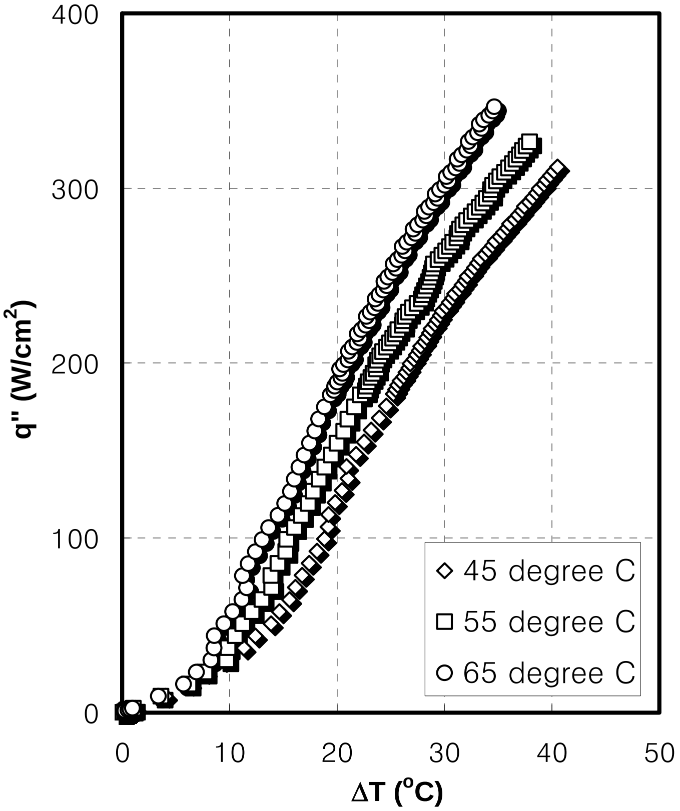

Figure A.54 Boiling curves of MTSP coating with spreader (t = 3.5 mm) in saturated water at different temperatures (45, 55, and 65 °C)

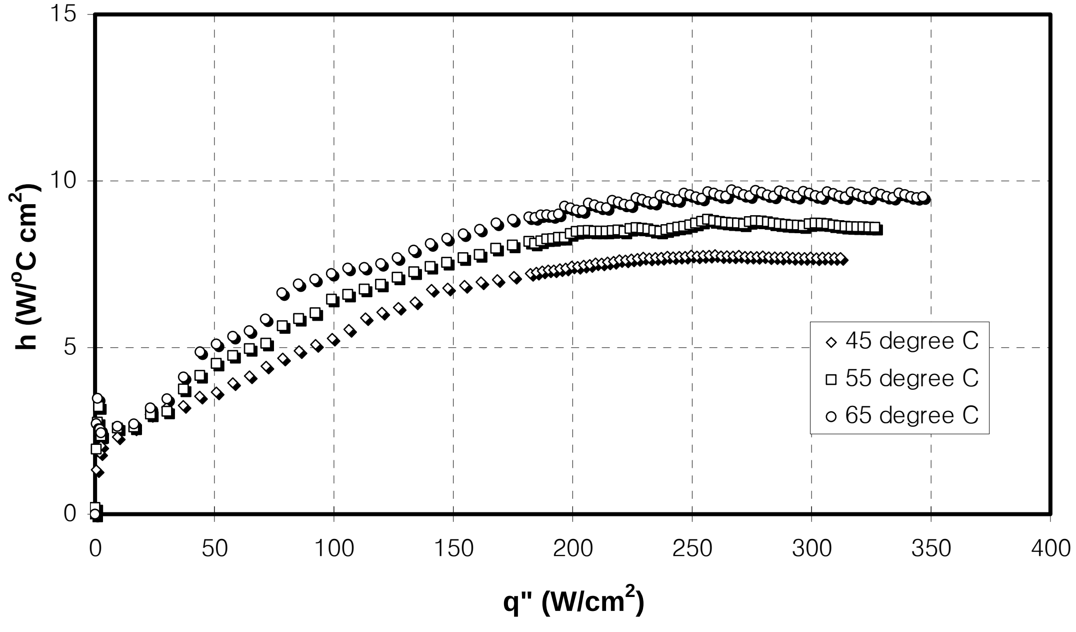

Figure A.55 Boiling coefficient of MTSP coating with spreader (t = 3.5 mm) in saturated water at different temperatures (45, 55, and 65 °C)

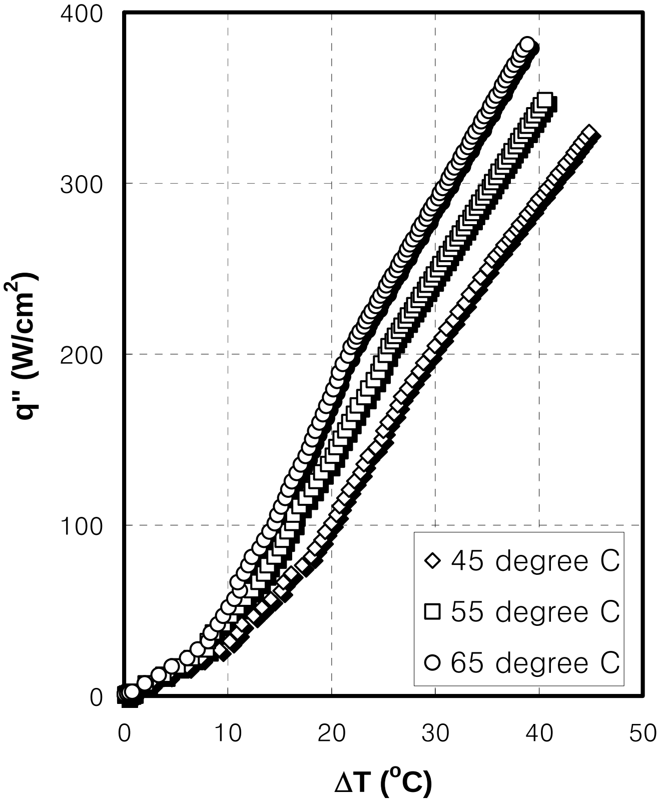

Figure A.56 Boiling curves of MTSP coating with spreader (t = 5.5 mm) in saturated water at different temperatures (45, 55, and 65 °C)

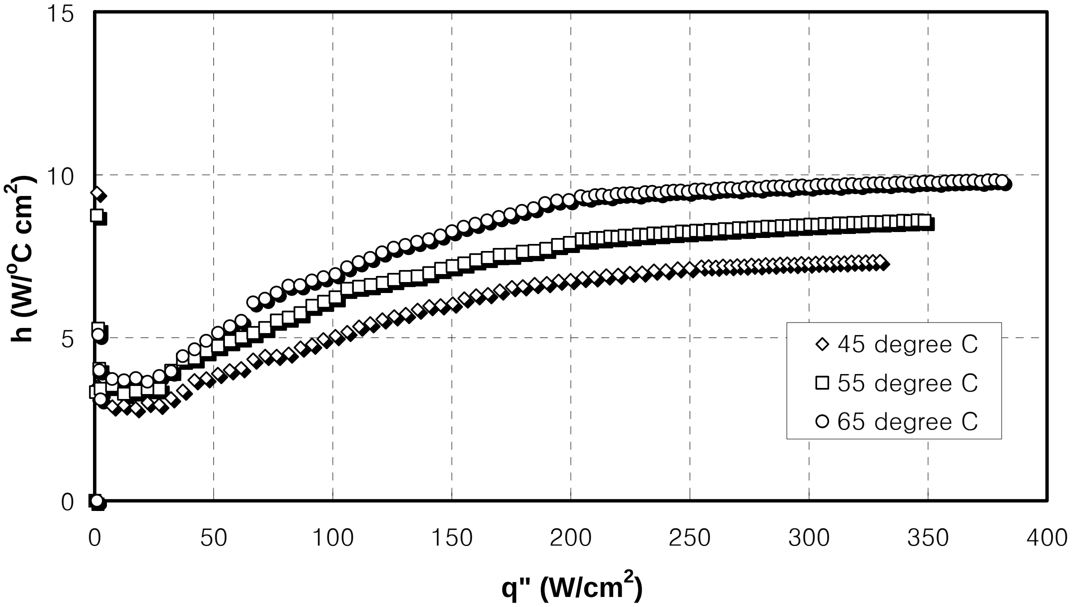

Figure A.57 Boiling coefficient of MTSP coating with spreader (t = 5.5 mm) in saturated water at different temperatures (45, 55, and 65 °C)

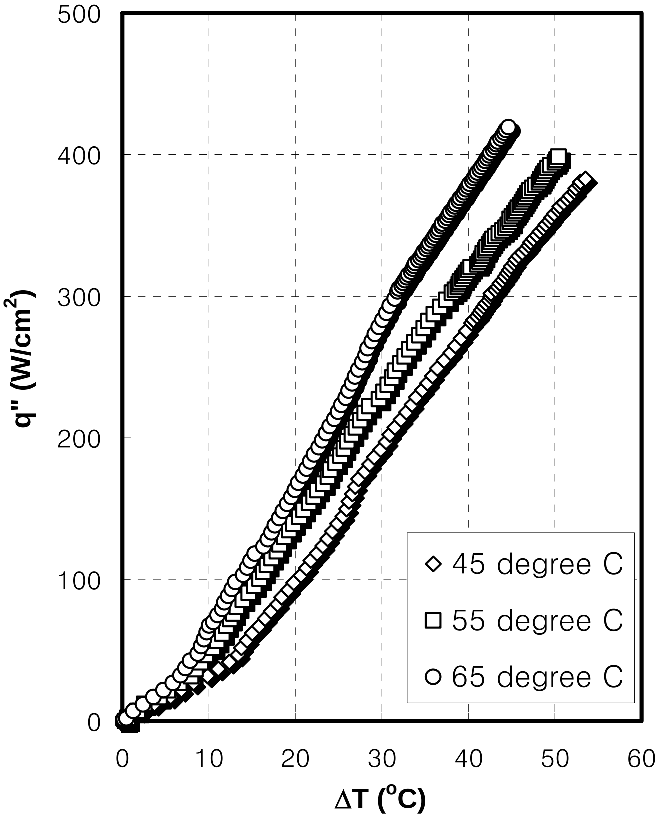

Figure A.58 Boiling curves of MTSP coating with spreader (t = 6.5 mm) in saturated water at different temperatures (45, 55, and 65 °C)

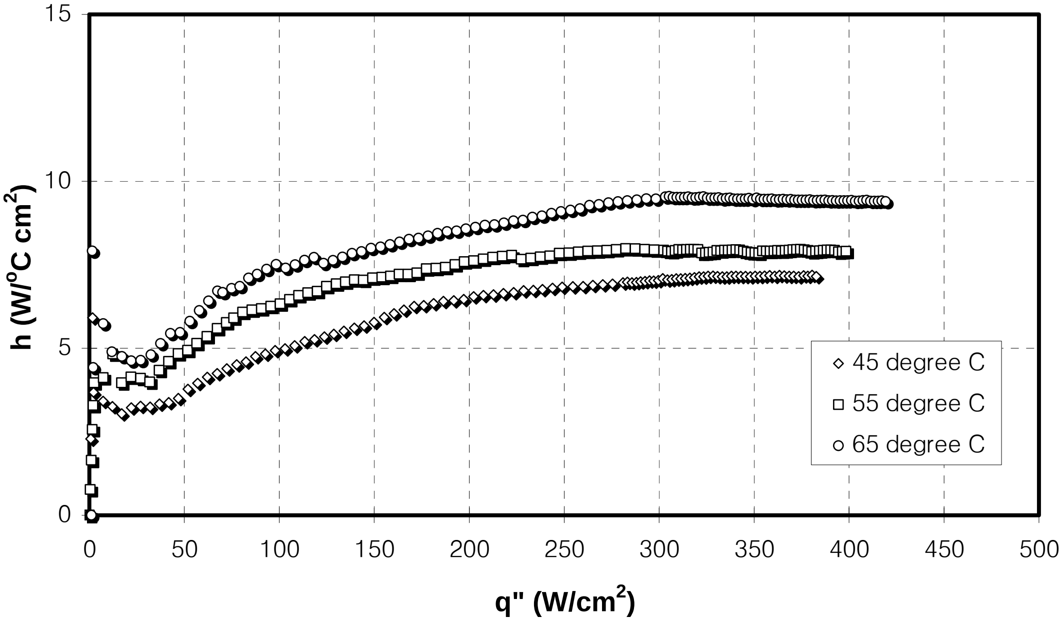

Figure A.59 Boiling coefficient of MTSP coating with spreader (t = 6.5 mm) in saturated water at different temperatures (45, 55, and 65 °C)

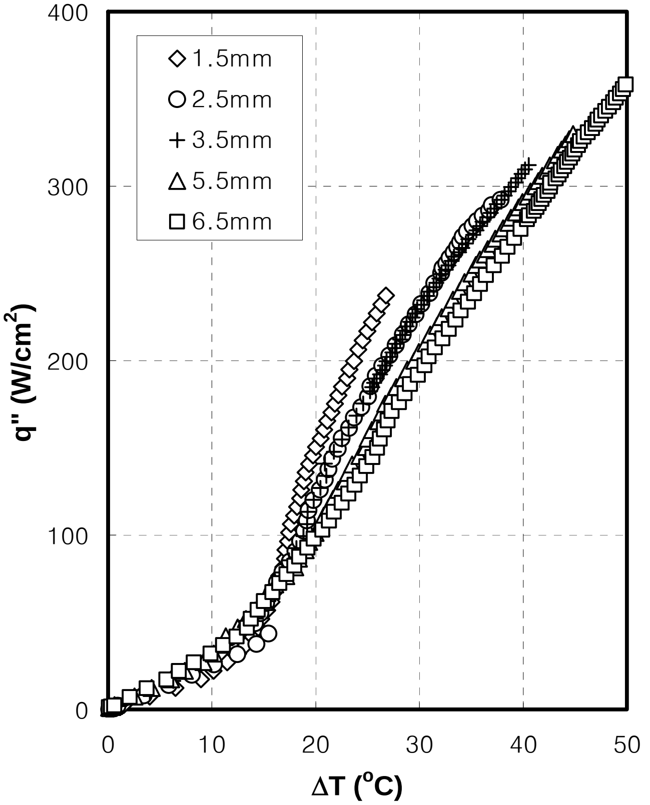

Figure A.60 Boiling curves of MTSP coating with spreaders in saturated water at 45°C

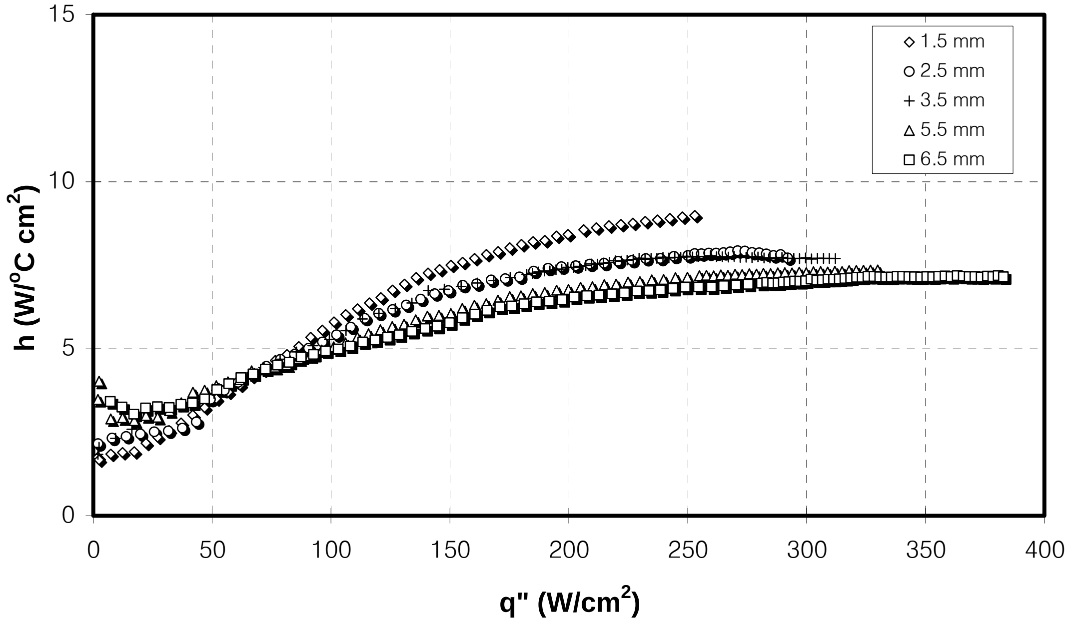

Figure A.61 Boiling coefficient of MTSP coating with spreaders in saturated water at 45°C

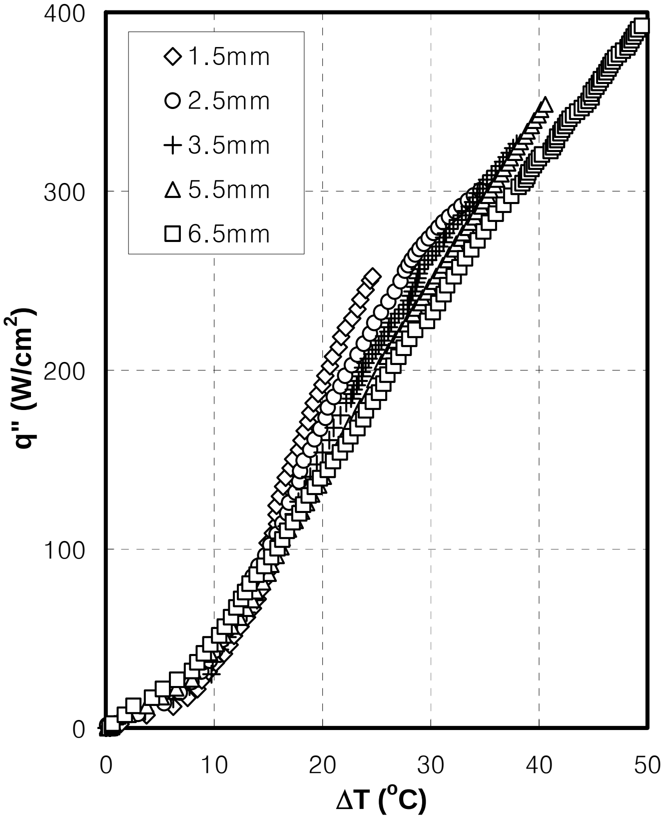

Figure A.62 Boiling curves of MTSP coating with spreaders in saturated water at 55°C

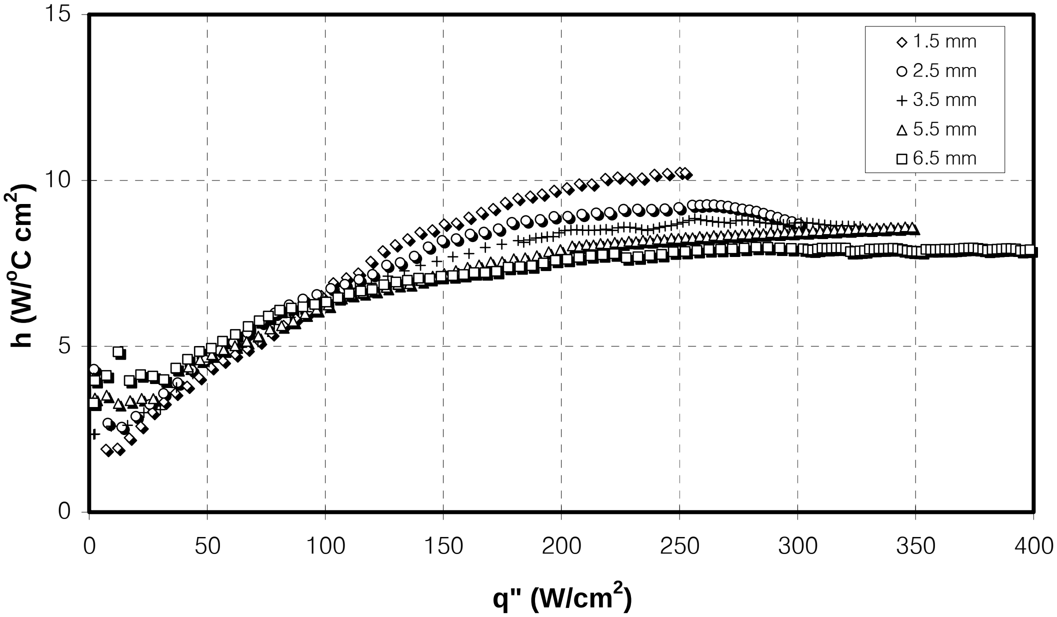

Figure A.63 Boiling coefficient of MTSP coating with spreaders in saturated water at 55°C

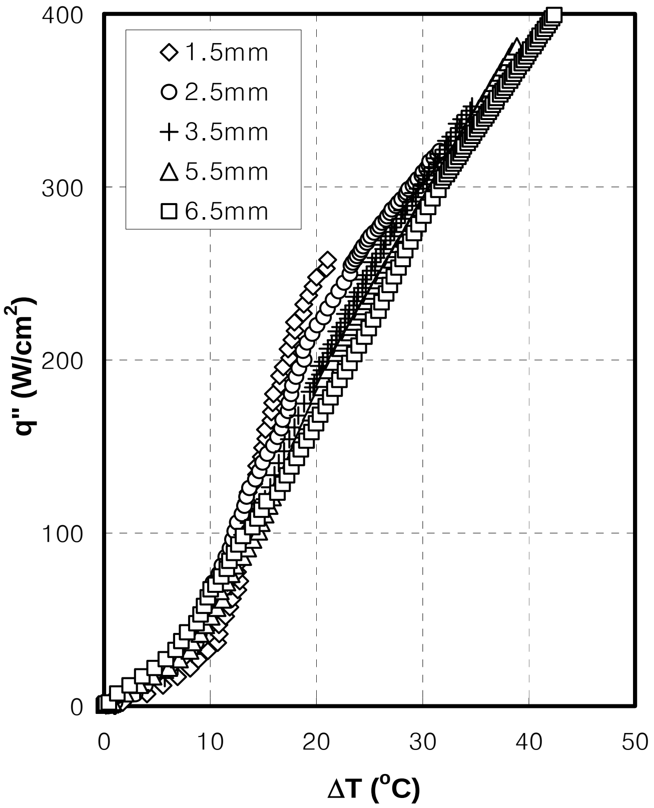

Figure A.64 Boiling curves of MTSP coating with spreaders in saturated water at 65°C

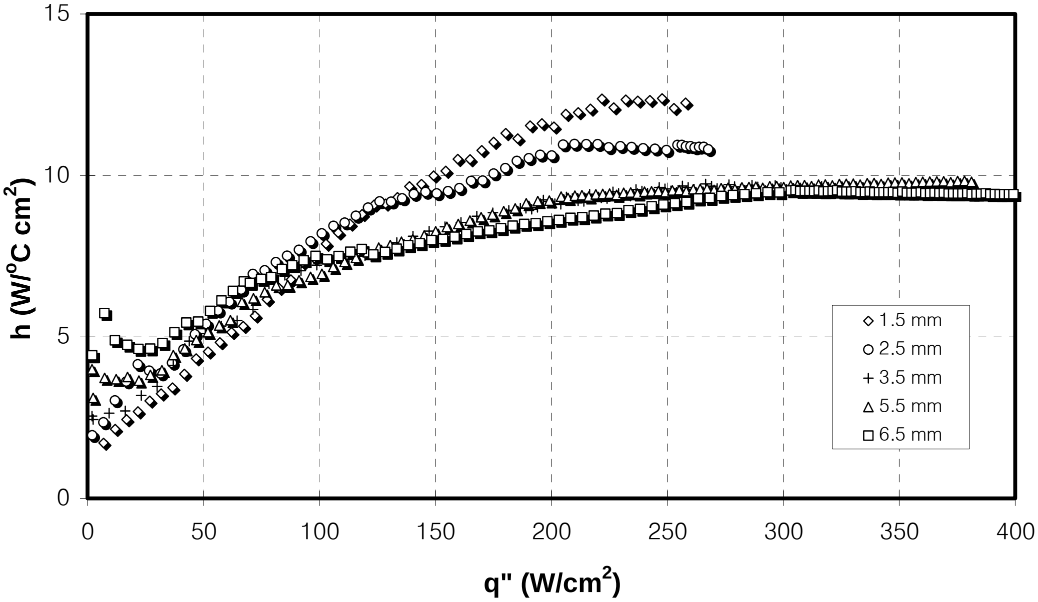

Figure A.65 Boiling coefficient of MTSP coating with spreaders in saturated water at 65°C

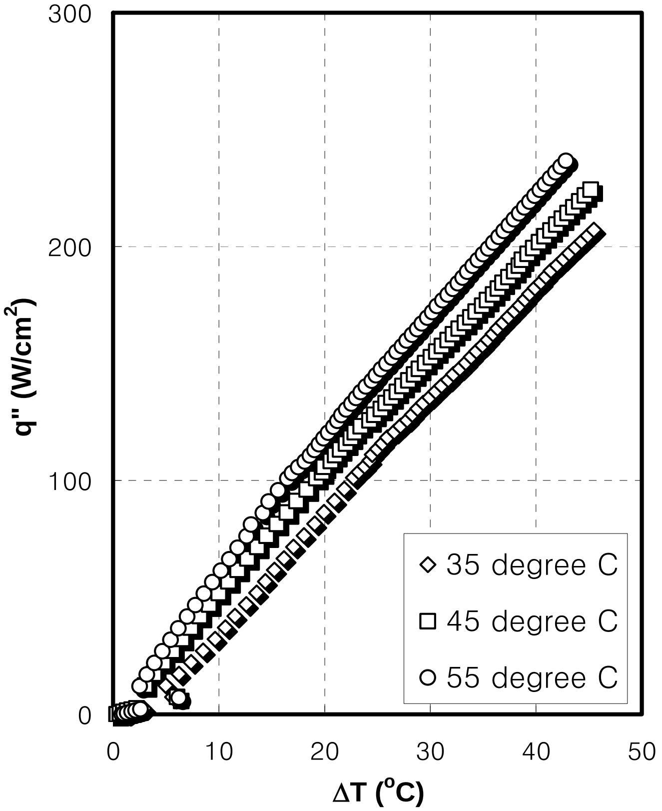

Figure A.66 Boiling curves of MTSP coating with spreader (t = 1.5 mm) in saturated FC-72 at different temperatures (35, 45, and 55 °C)

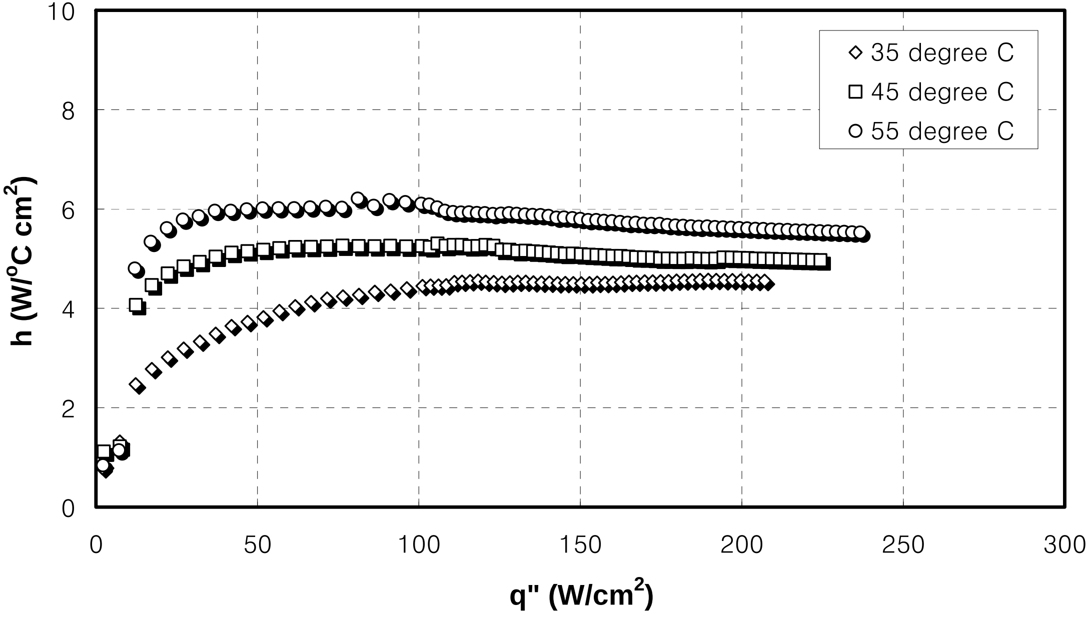

Figure A.67 Boiling coefficient of MTSP coating with spreader (t = 1.5 mm) in saturated FC-72 at different temperatures (35, 45, and 55 °C)

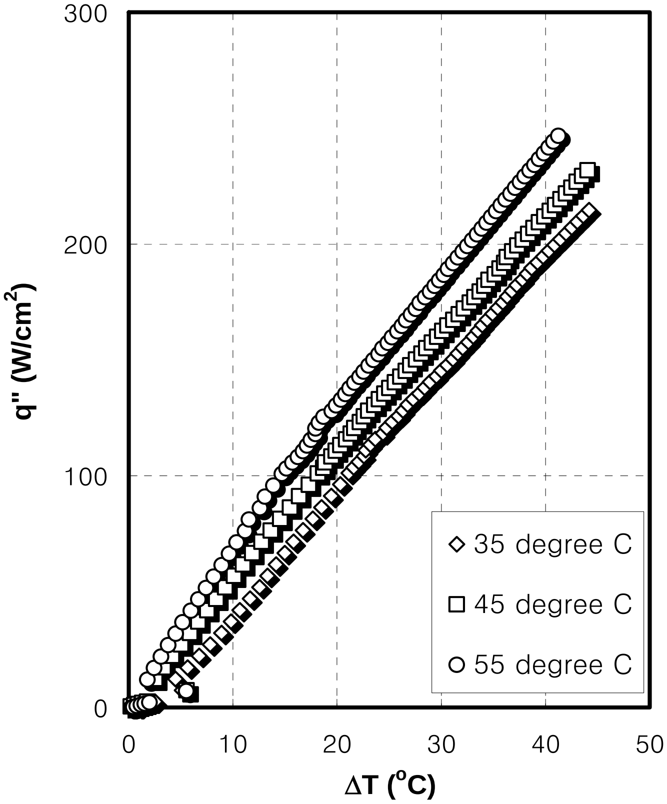

Figure A.68 Boiling curves of MTSP coating with spreader (t = 2.5 mm) in saturated FC-72 at different temperatures (35, 45, and 55 °C)

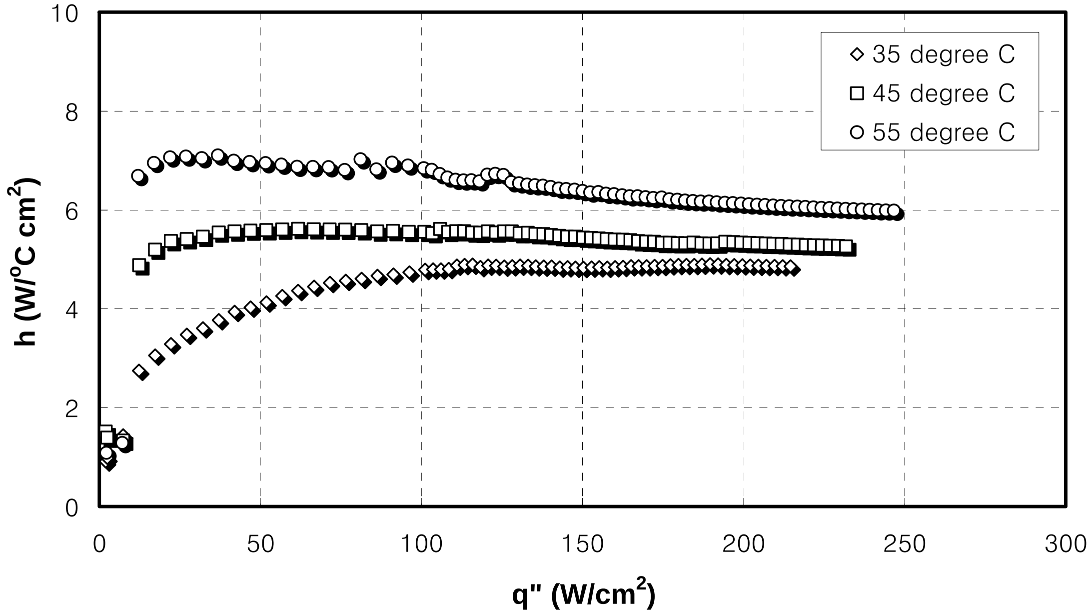

Figure A.69 Boiling coefficient of MTSP coating with spreader (t = 2.5 mm) in saturated FC-72 at different temperatures (35, 45, and 55 °C)

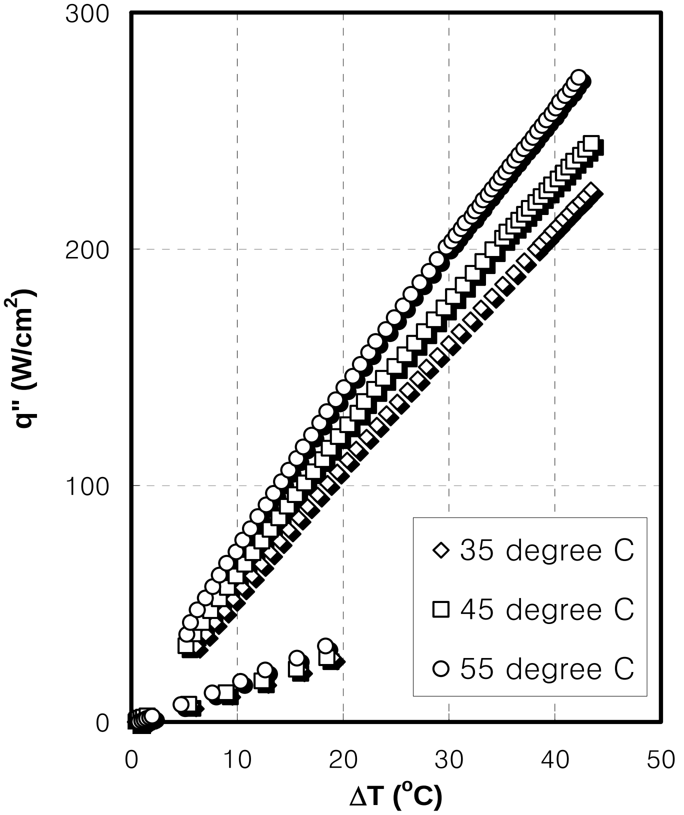

Figure A.70 Boiling curves of MTSP coating with spreader (t = 3.5 mm) in saturated FC-72 at different temperatures (35, 45, and 55 °C)

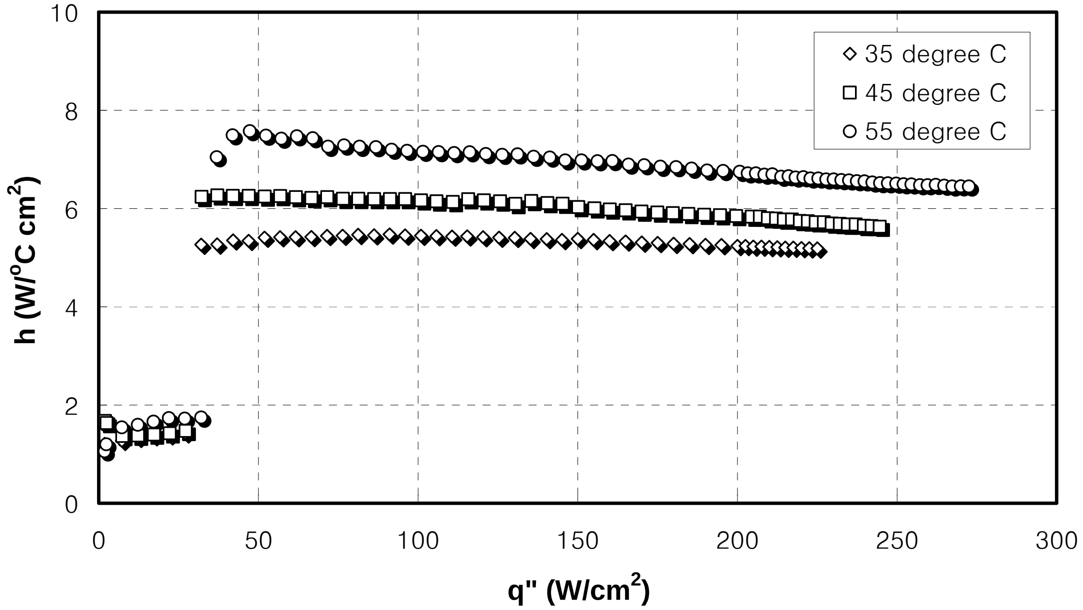

Figure A.71 Boiling coefficient of MTSP coating with spreader (t = 3.5 mm) in saturated FC-72 at different temperatures (35, 45, and 55 °C)

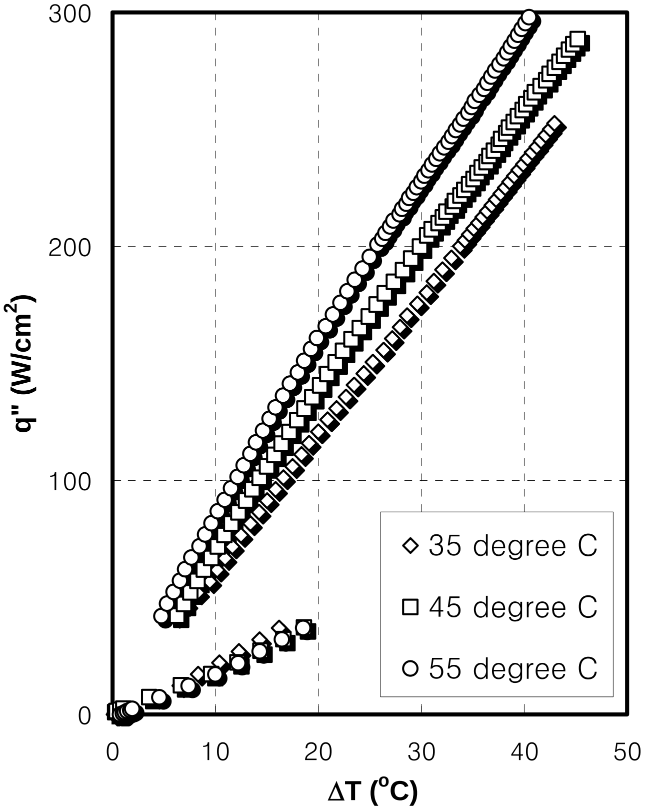

Figure A.72 Boiling curves of MTSP coating with spreader (t = 5.5 mm) in saturated FC-72 at different temperatures (35, 45, and 55 °C)

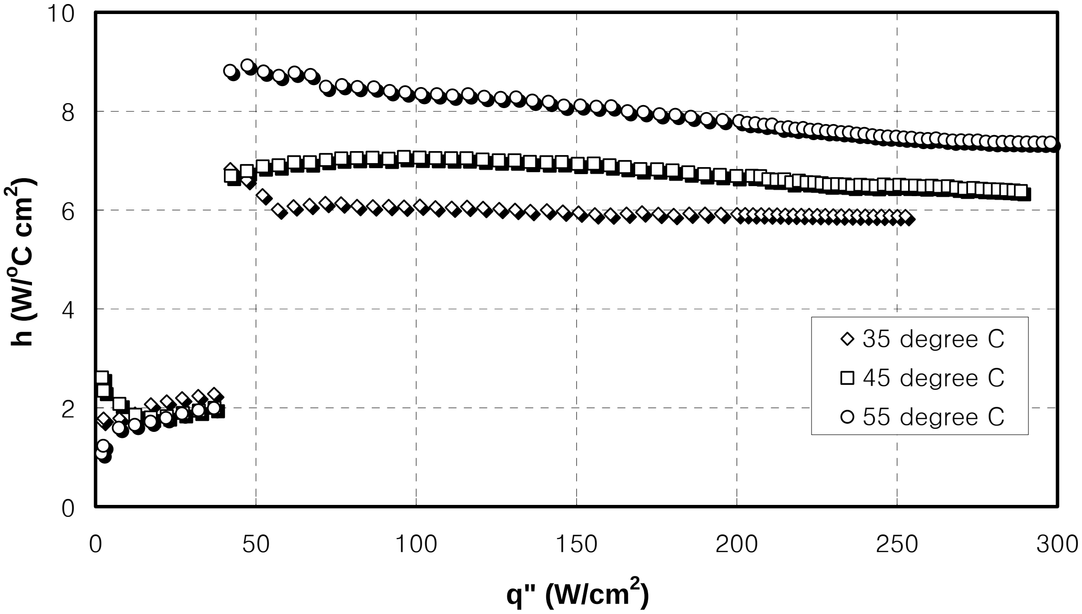

Figure A.73 Boiling coefficient of MTSP coating with spreader (t = 5.5 mm) in saturated FC-72 at different temperatures (35, 45, and 55 °C)

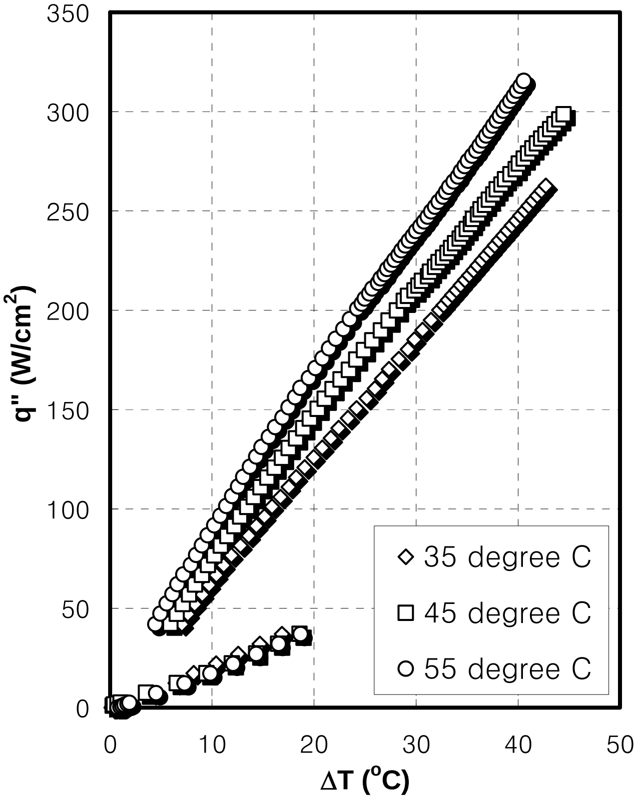

Figure A.74 Boiling curves of MTSP coating with spreader (t = 6.5 mm) in saturated FC-72 at different temperatures (35, 45, and 55 °C)

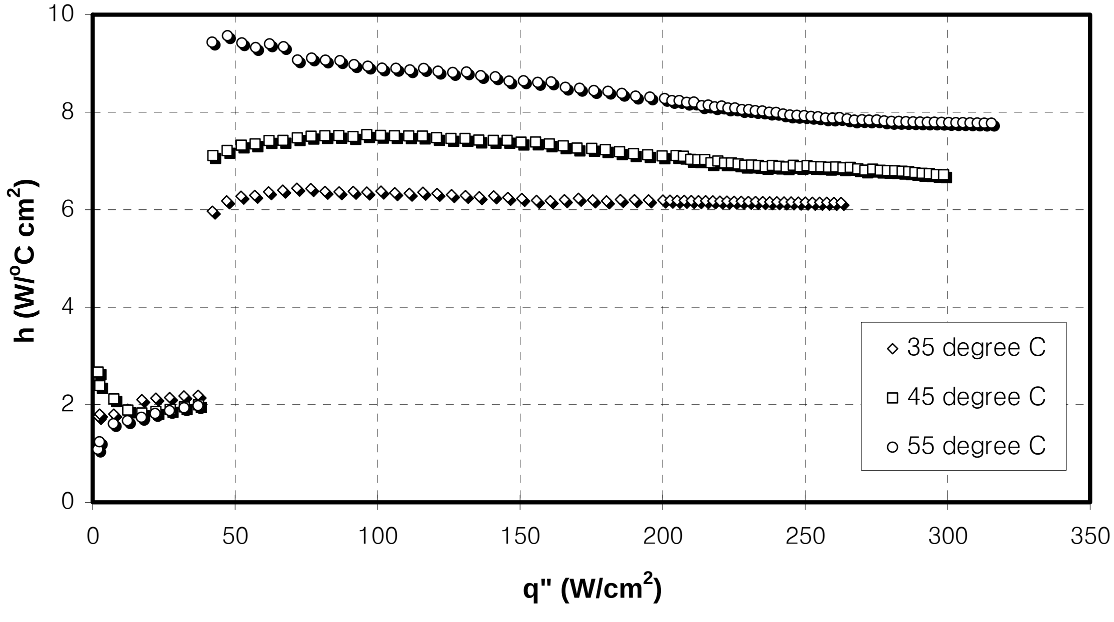

Figure A.75 Boiling coefficient of MTSP coating with spreader (t = 6.5 mm) in saturated FC-72 at different temperatures (35, 45, and 55 °C)

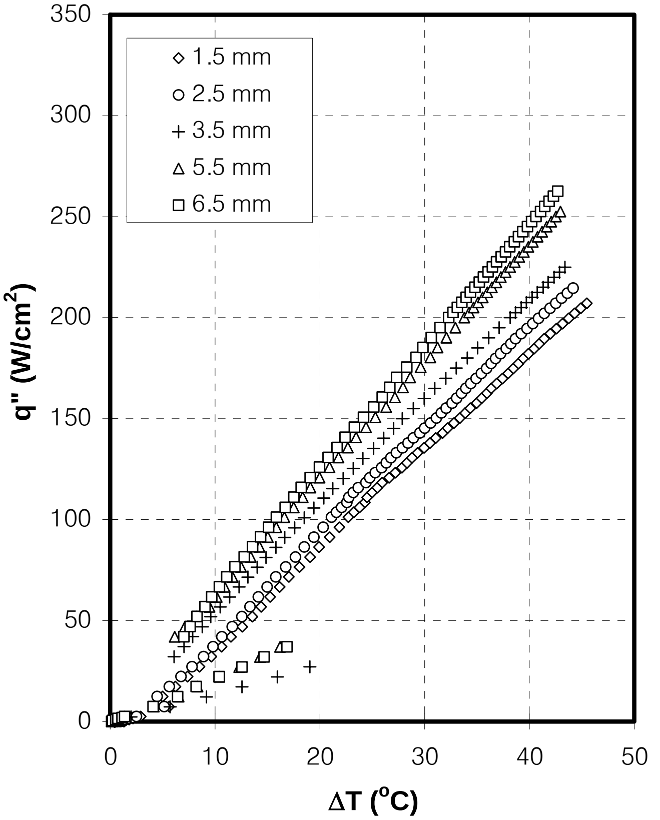

Figure A.76 Boiling curves of MTSP coating with spreaders in saturated FC-72 at 35°C

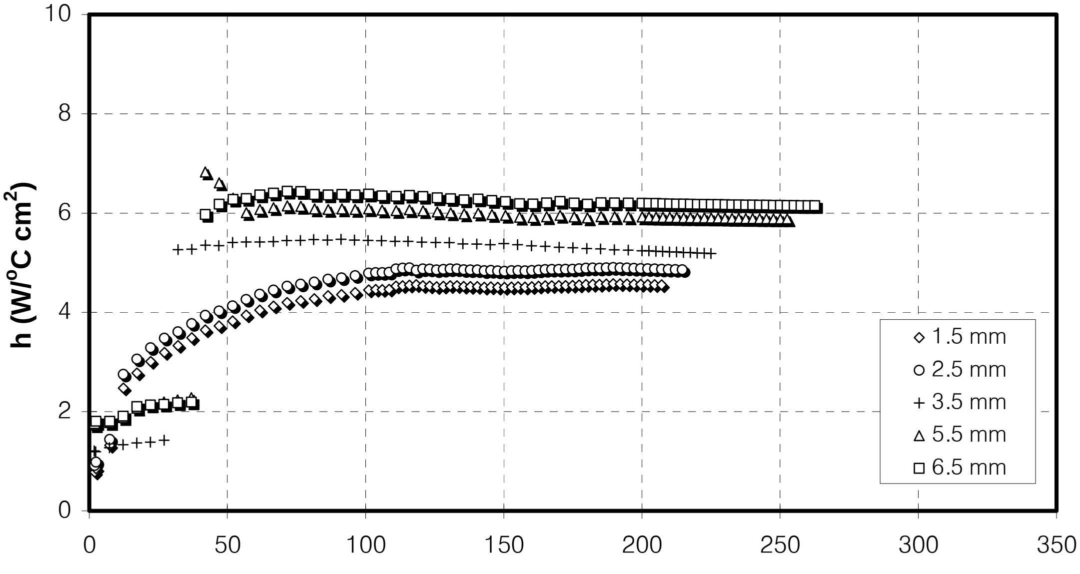

Figure A.77 Boiling coefficient of MTSP coating with spreaders in saturated FC-72 at 35°C

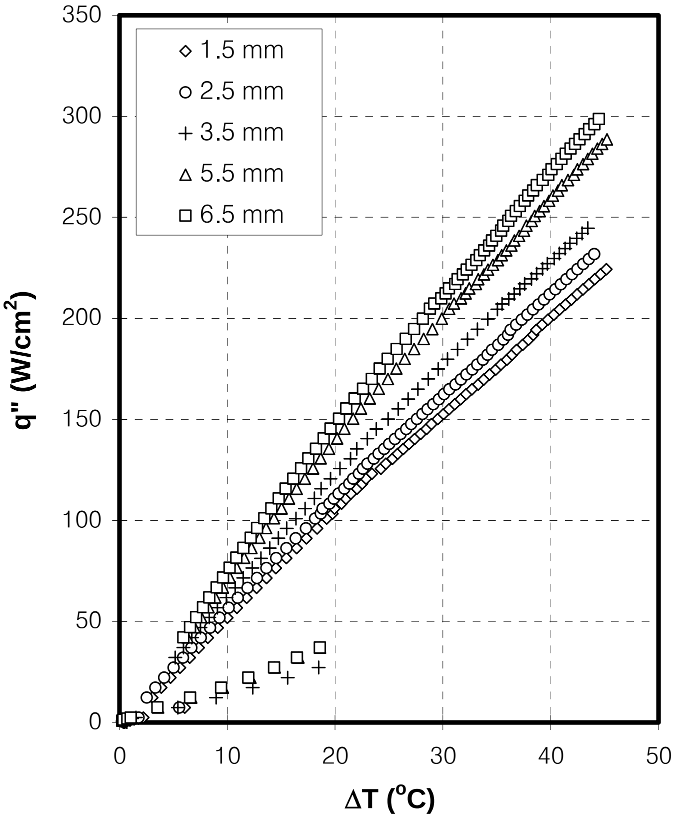

Figure A.78 Boiling curves of MTSP coating with spreaders in saturated FC-72 at 45°C

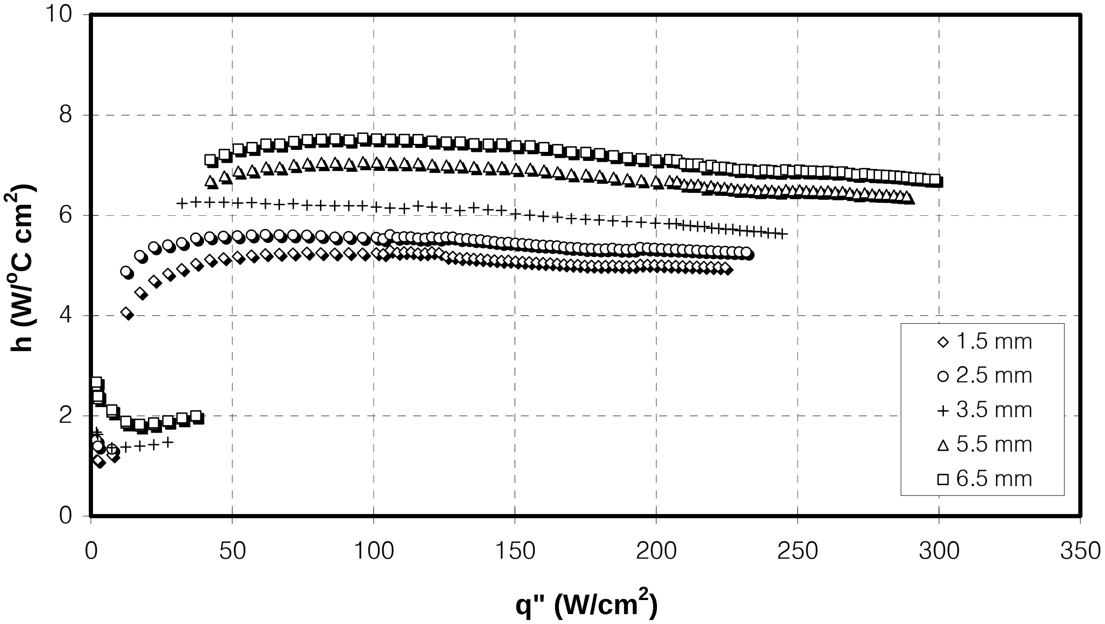

Figure A.79 Boiling coefficient of MTSP coating with spreaders in saturated FC-72 at 45°C

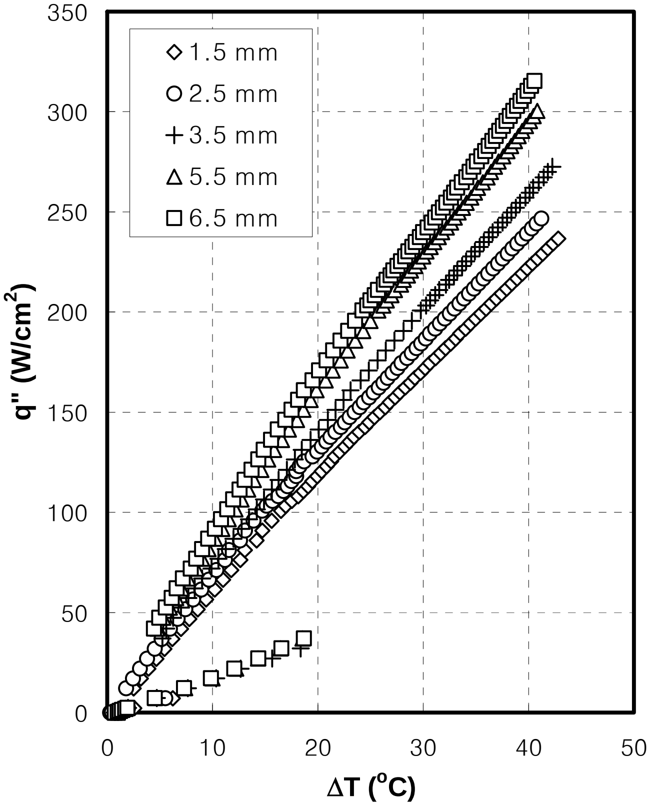

Figure A.80 Boiling curves of MTSP coating with spreaders in saturated FC-72 at 55°C

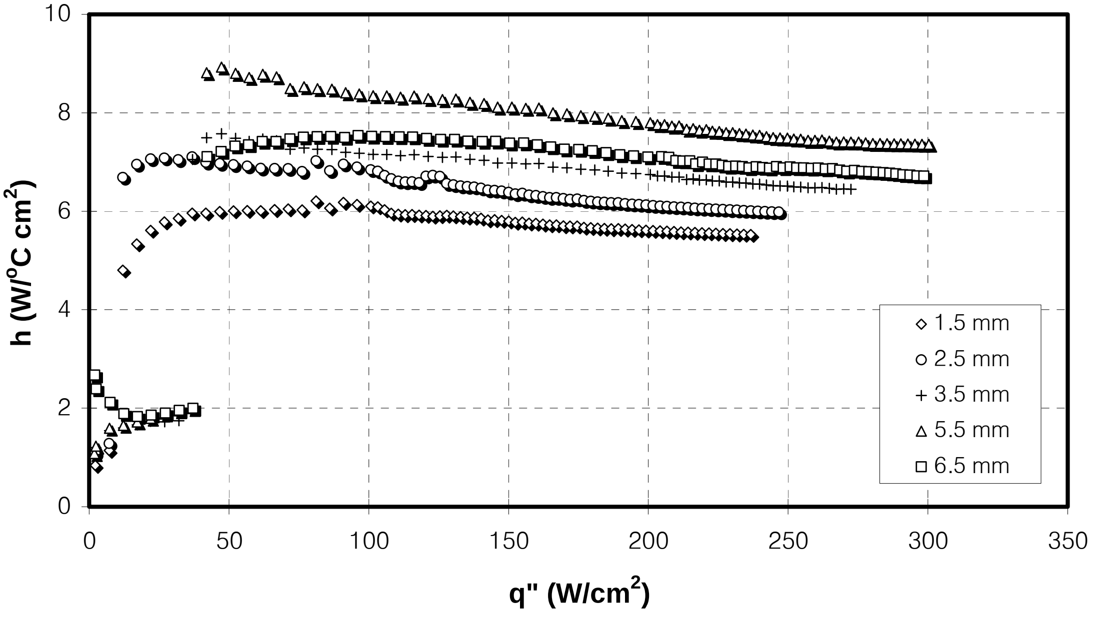

Figure A.81 Boiling coefficient of MTSP coating with spreaders in saturated FC-72 at 55°C

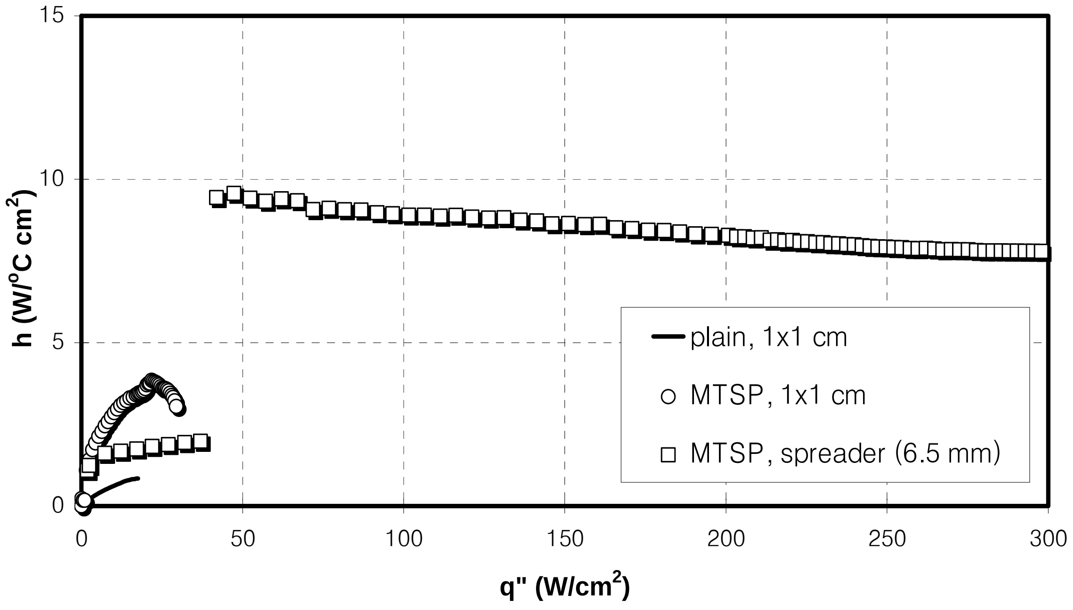

Figure A.82 Boiling coefficient comparison of MTSP in saturated water at 60˚C

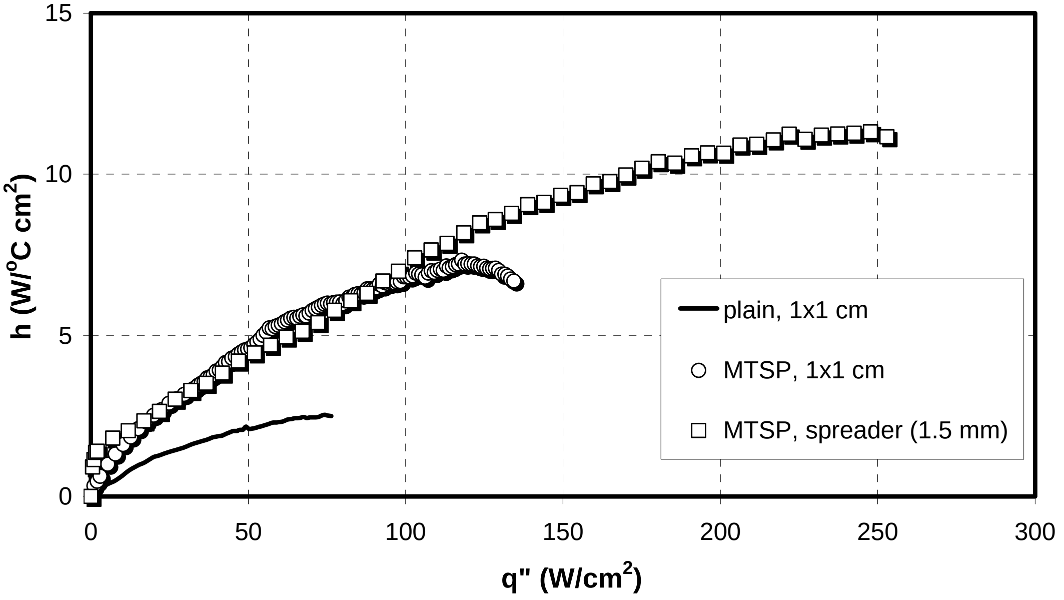

Figure A.83 Boiling coefficient comparison of MTSP in saturated FC-72 at 55˚C

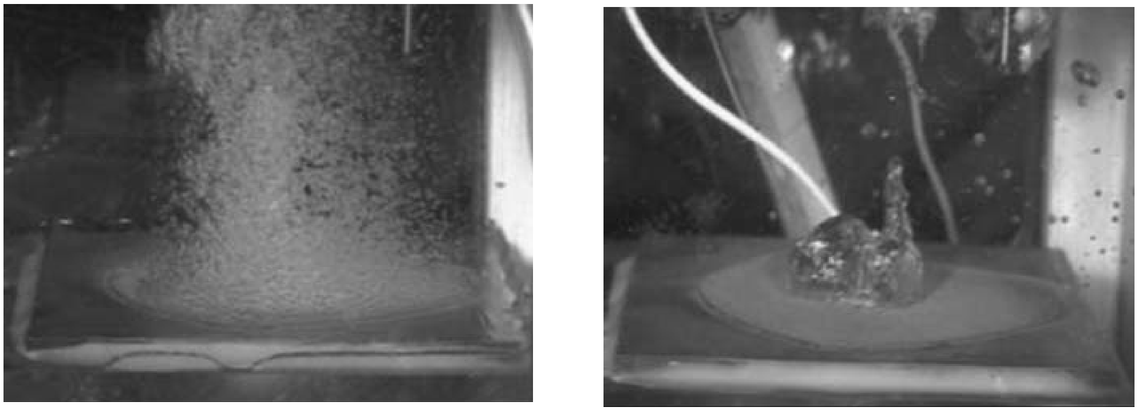

FC-72 Water

Figure A.84 Sample pictures of boiling from 2.5mm thickness spreader in saturated FC-72 and water at 55 °C (q” =150 W/cm^2)

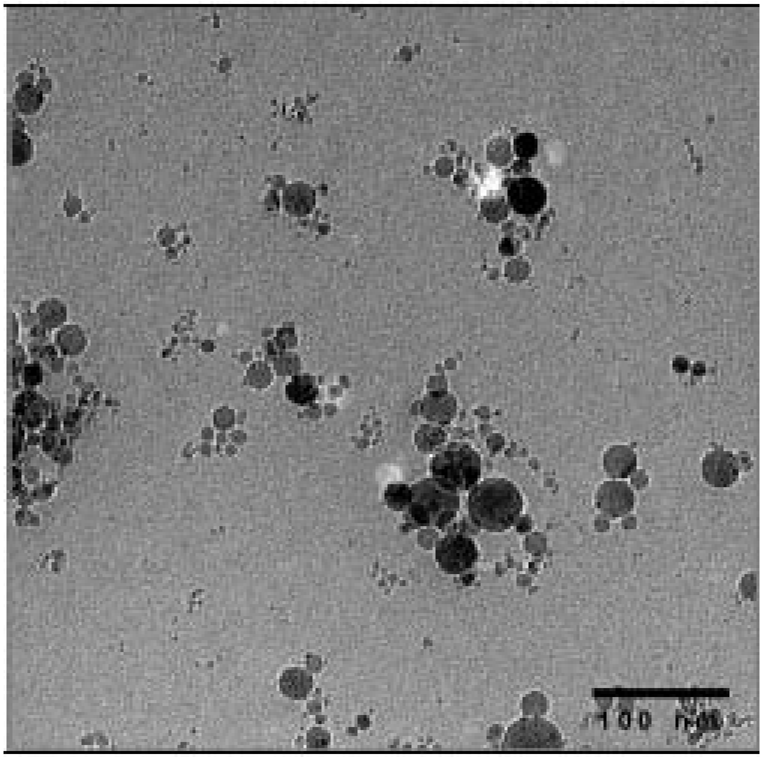

Courtesy of nanoComposix Inc.

Figure A.85 Nano-scale image of nanofluids

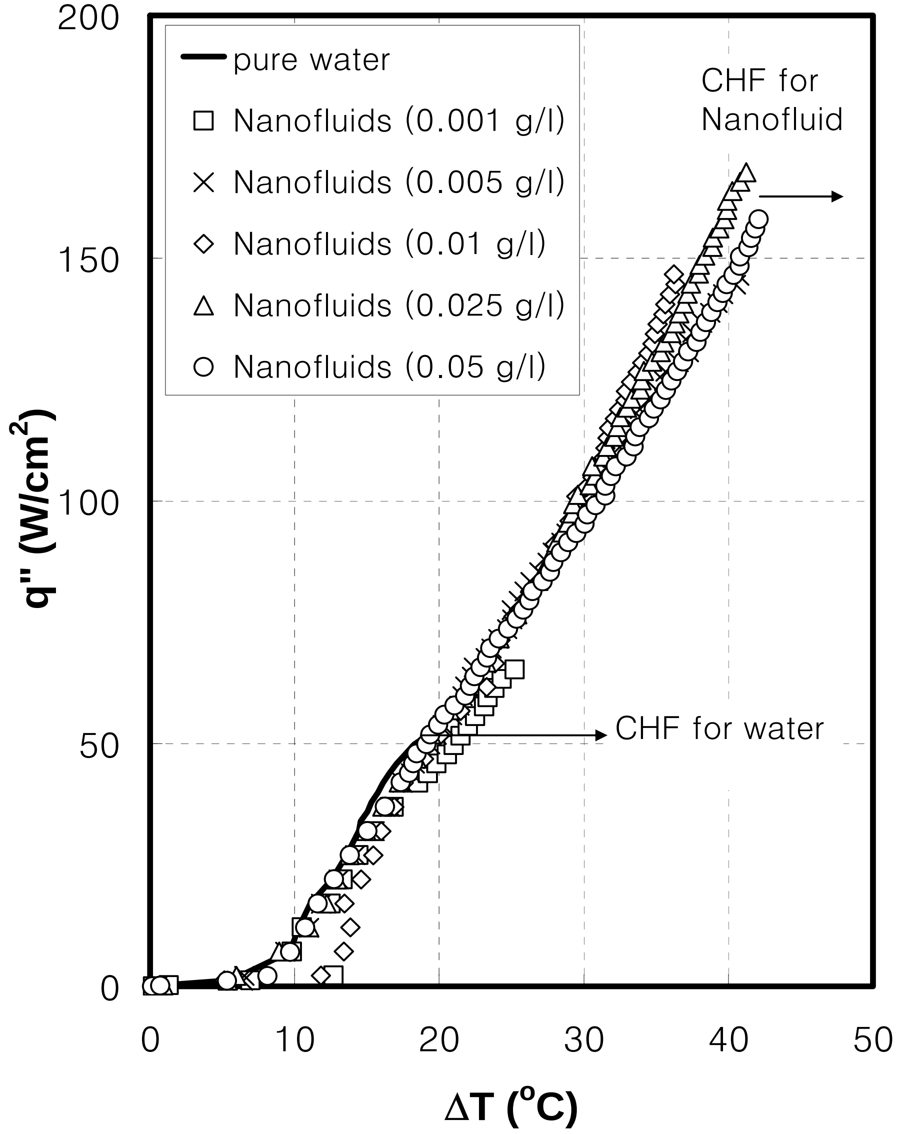

Figure A.86 Boiling curves of different concentrations nanofluids at 60°C saturation

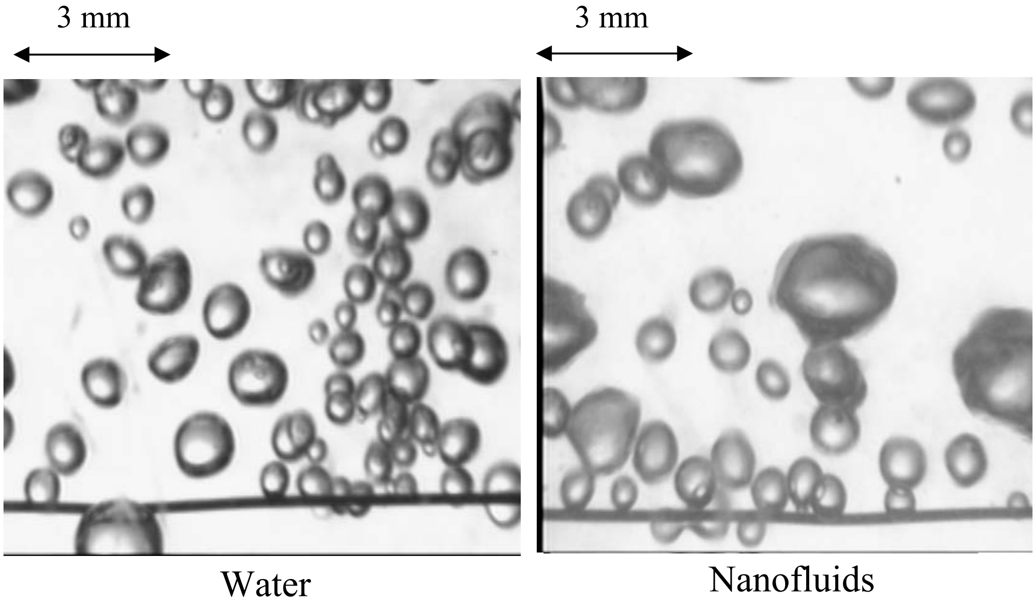

Figure A.87 Sample picture of bubbles in water and nanofluids at heat flux of 20 W/cm^2

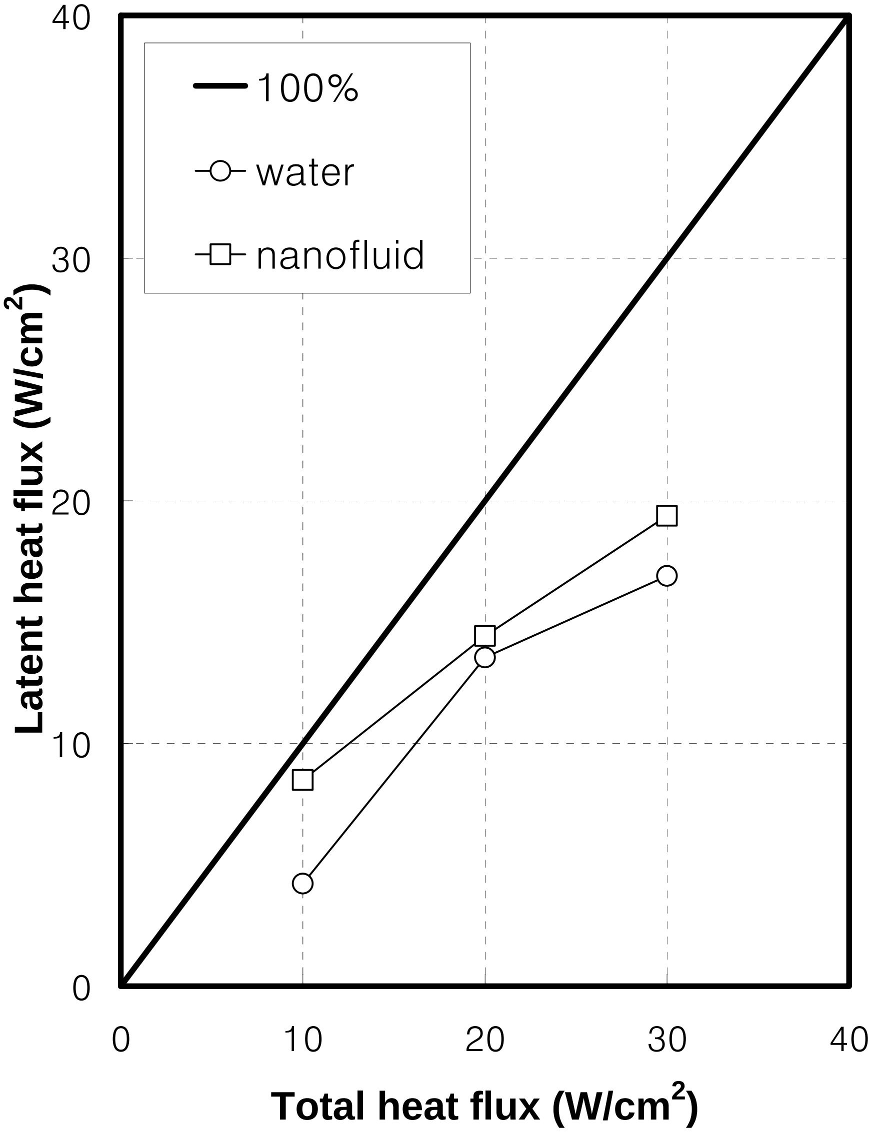

Figure A.88 Latent heat contribution comparison for water and nanofluids

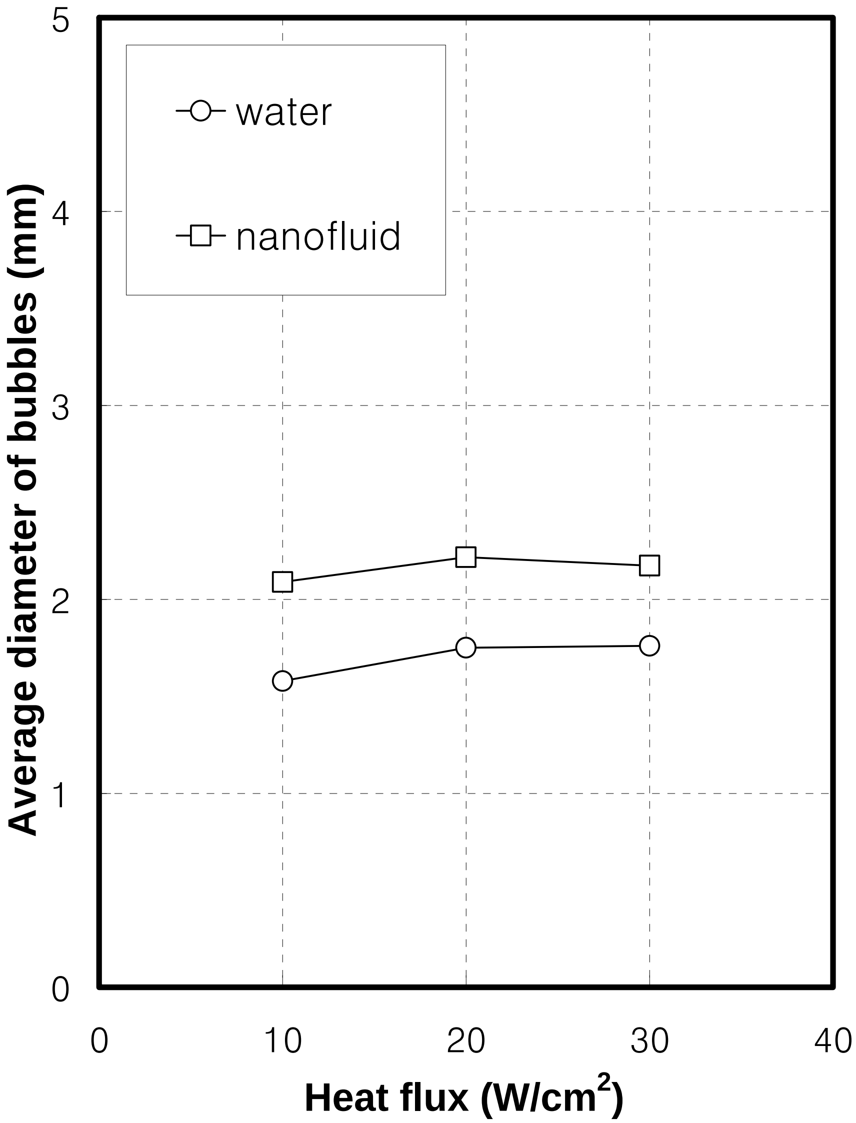

Figure A.89 Bubble sizes comparison for water and nanofluids

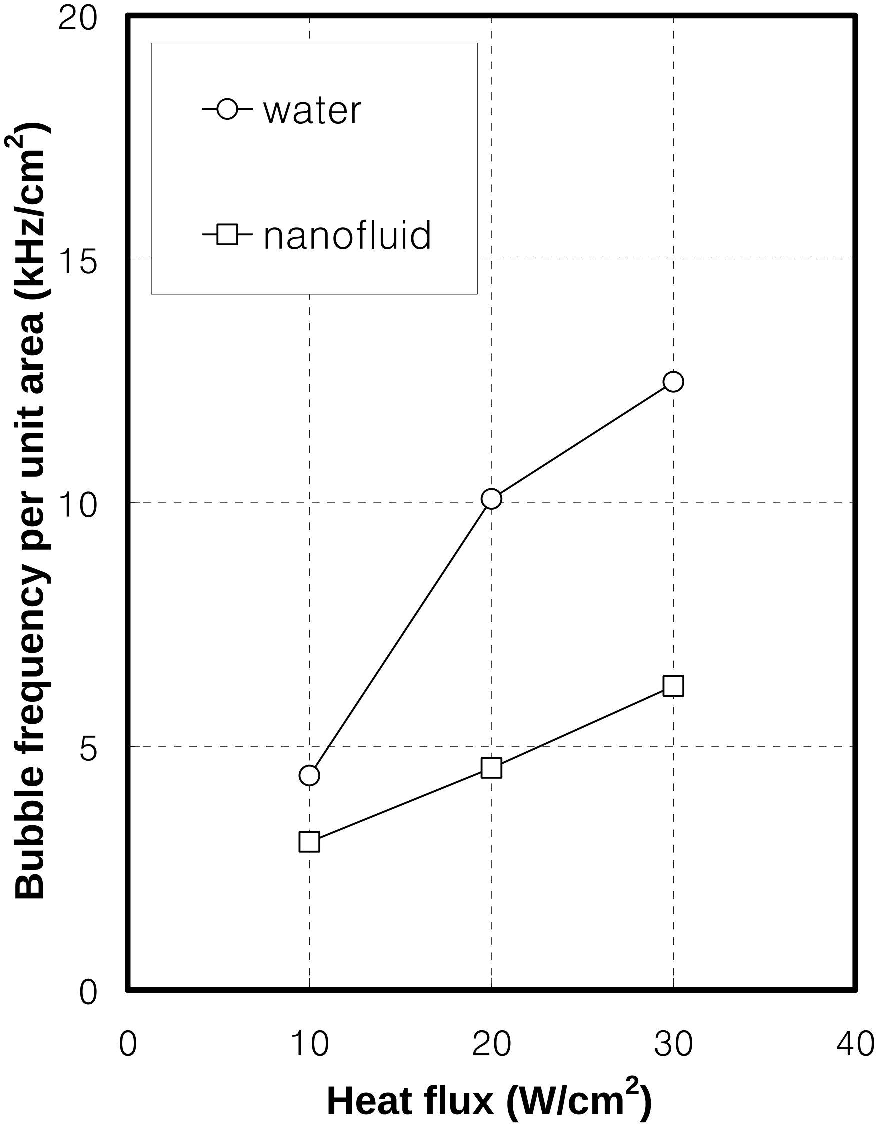

Figure A.90 Bubble departure frequency for water and nanofluids

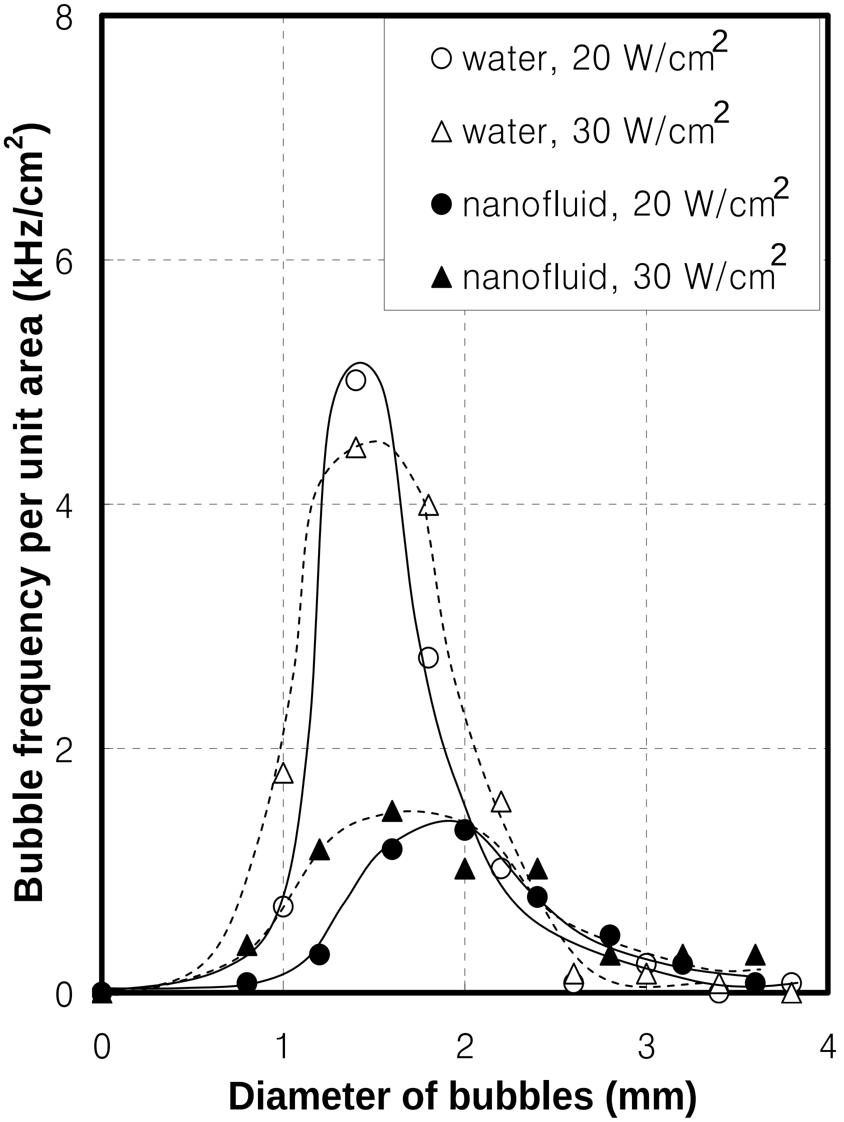

Figure A.91 Bubble departure frequency over bubble size distribution for water and nanofluids

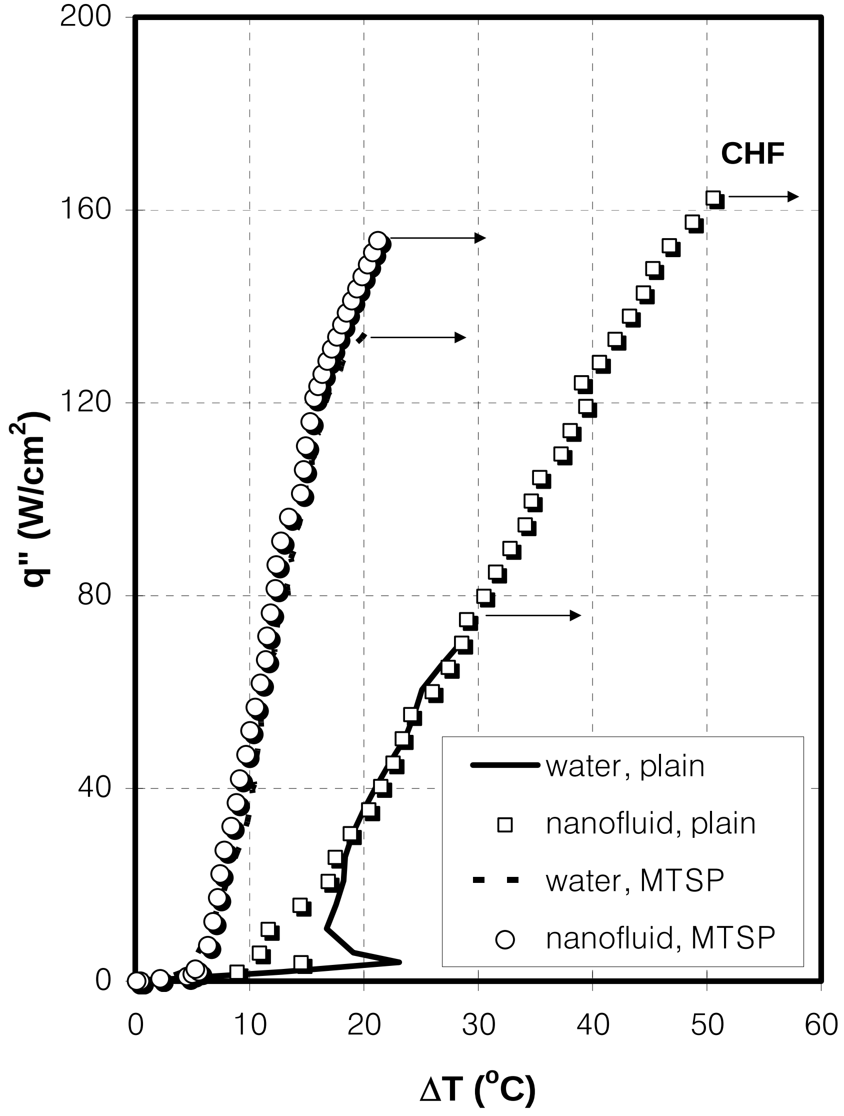

Figure A.92 Boiling curves of MTSP coating in nanofluids

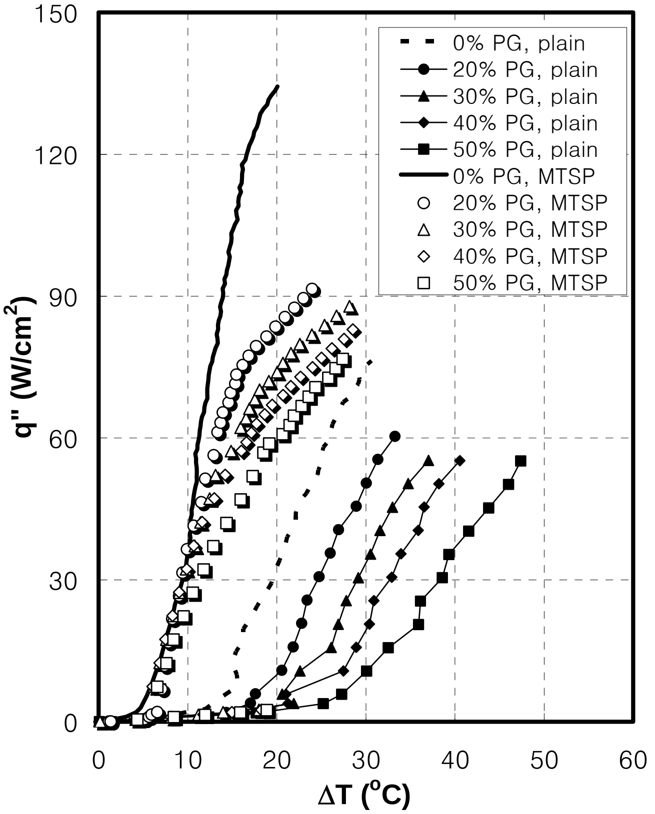

Figure A.93 Boiling curves of MTSP coating in anti-freeze at 60°C saturation

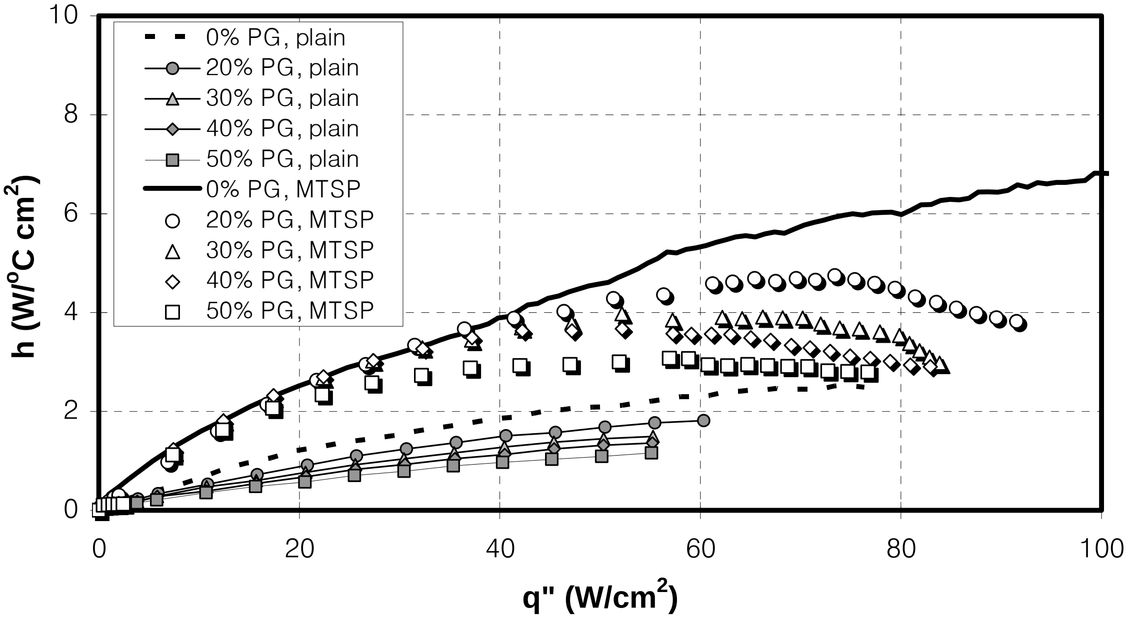

Figure A.94 Boiling coefficient of MTSP coating in anti-freeze at 60°C saturation

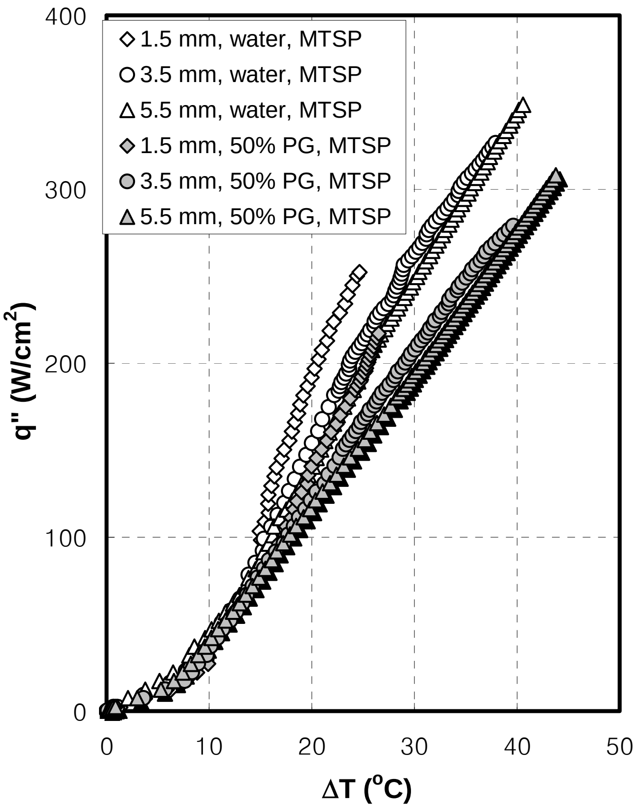

Figure A.95 Boiling curves of MTSP coating with spreaders in anti-freeze at 55°C saturation

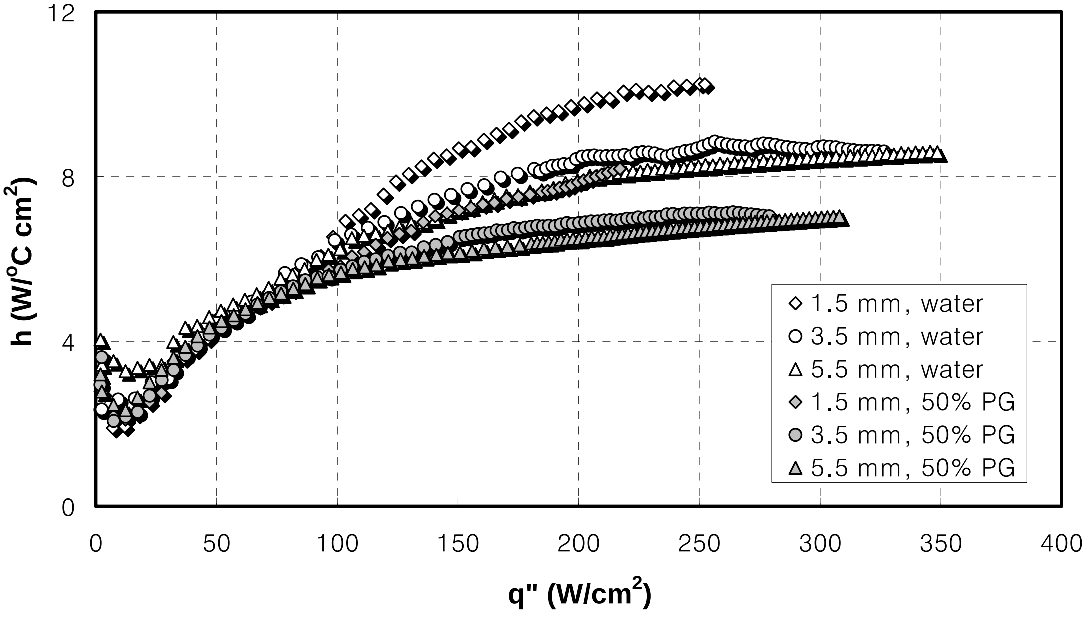

Figure A.96 Boiling coefficient comparison of MTSP coating with spreaders for water and anti-freeze at 55°C saturation

APPENDIX B

TABLES

Properties	R-123
Chemical formula	$CHCl_2CF_3$
Boiling point [°C]	27.8
Density – liquid [kg/m^3]	1463
Density – vapor [kg/m^3]	6.47
Specific heat – liquid [J/kg·K]	965
Latent heat [J/kg]	1.70E+05
Thermal conductivity – liquid [W/m·K]	0.081
Surface tension [N/m]	0.0157

Table B.1 Selected thermal properties of saturated R-123 at 1 atm

Properties	FC-72
Chemical formula	C_6F_{14}
Boiling point [°C]	56.5
Density – liquid [kg/m^3]	1598.9
Density – vapor [kg/m^3]	13.37
Specific heat – liquid [J/kg·K]	1121
Latent heat [J/kg]	9.43E+04
Thermal conductivity – liquid [W/m·K]	0.0545
Surface tension [N/m]	0.0081

Table B.2 Selected thermal properties of saturated FC-72 at 1 atm

Properties	methanol
Chemical formula	CH_3OH
Boiling point [°C]	65.5
Density – liquid [kg/m^3]	748.8
Density – vapor [kg/m^3]	1.22
Specific heat – liquid [J/kg·K]	2528
Latent heat [J/kg]	1.17E+06
Thermal conductivity – liquid [W/m·K]	0.207
Surface tension [N/m]	0.0215

Table B.3 Selected thermal properties of saturated methanol at 1 atm

Properties	water
Chemical formula	H_2O
Boiling point [°C]	100
Density – liquid [kg/m^3]	958.4
Density – vapor [kg/m^3]	0.597
Specific heat – liquid [J/kg·K]	4276
Latent heat [J/kg]	2.26E+06
Thermal conductivity – liquid [W/m·K]	0.68
Surface tension [N/m]	0.0589

Table B.4 Selected thermal properties of saturated water at 1 atm

Concentration by % volume	**Pressure at Tsat=60°C (psi)**	**Freezing Point of PG Mixture (°C)**
0	2.9	0
20	2.7	-8
30	2.6	-14
40	2.5	-22
50	2.4	-34

Table B.5 System pressures of anti-freeze (20-50%) at 60°C saturation

APPENDIX C

POOL BOILING DAQ PROGRAM

```
10    !================================================================
20    !
30    !      FLAT SURFACE BOILING CURVE MEASUREMENT
40    !
50    !      WRITTEN BY JE-YOUNG CHANG 9/16/97
60    !      MODIFIED BY JOO HAN KIM 05/03/02
70    !
80    !================================================================
90    !
91    DIM Names$(1:2,1:3)[8]
92    INTEGER H,Numh,Numr
94    !
95    ! WARNING:
97    ! Power 1 uses 110 and 111 T/C channels
98    ! Power 2 uses 112 and 113 T/C channels
99    Numh=2                            ! Number of heaters to test (1 or 2)
100   Pch=1                             ! If Numh=1, which power channel? (1 or 2)
102   Numr=2                            ! Number of runs per heater (1-3)
105   T=0                               ! Time between runs (hours)
106   Dgt=1.5                           ! Time to degass prior to testing (hours)
108   !
109   ! Names for heater on Power 1 channel
110   Names$(1,1)="H94_1"
111   Names$(1,2)="H94_2"
112   Names$(1,3)="H94_0"
113   ! Names for heater on Power 2 channel
114   Names$(2,1)="H95_1"
115   Names$(2,2)="H95_2"
116   Names$(2,3)="H95_0"
117   !
120   CALL Bulk_stability
121   IF Dgt>0 THEN
122     DISP "DEGASSING FOR",Dgt,"HOURS"
123     OUTPUT 709;"CLOSE 300,304-306"
124     WAIT INT(Dgt*3600)
126     OUTPUT 709;"OPEN 300"
127   END IF
128   !
129   SELECT Numh
130   CASE 1
131     J1=Pch
132     J2=Pch
133   CASE 2
134     J1=1
135     J2=2
136   END SELECT
137   !
139   FOR I=1 TO Numr
140     FOR J=J1 TO J2
141       OUTPUT 709;"CLOSE 300,304-306"
142       DISP "Stirring fluid for 2 minutes"
144       WAIT 120
145       IF I=1 AND J=1 THEN GOTO 149
146       DISP "Waiting",T,"hours before Test#",I,"for Heater#",J
147       WAIT INT(T*3600)-120
149       OUTPUT 709;"OPEN 300"
150   !
151       DISP "Beginning Test#",I,"of Heater#",J
152       BEEP
153       BEEP
154       WAIT 15
155   !
156       CALL Main(Names$(J,I),J)
157     NEXT J
158   NEXT I
187   DISP "End of Testing"
188   MASS STORAGE IS "\USERS\JOO"
```

```
189   !
236   STOP
237   END
2350  !
2360  !--------------- END OF MAIN PROGRAM ----------------------------------!
2370  !
2380  SUB Cal_heatflux(Area,Vh(*),Current(*),Qq(*),K)
2390    Qq(K)=Current(K)*Vh(K)/Area
2400  SUBEND
2410  !
2420  !
2430  SUB Meas_volt(Vh(*),K,Hsw)
2431    OUTPUT 709;"USE 000"
2432    OUTPUT 709;"CONF DCV"
2433    OUTPUT 709;"NPLC 1"
2434    OUTPUT 709;"RANGE AUTO"
2435    OUTPUT 709;"NRDGS 1"
2436    OUTPUT 709;"DELAY 0.01"
2437    SELECT Hsw
2438    CASE 1
2440      OUTPUT 709;"MEAS DCV,201"
2450    CASE 2
2460      OUTPUT 709;"MEAS DCV,202"
2461    END SELECT
2470    ENTER 709;Volth
2490    Vh(K)=ABS(Volth)
2500  SUBEND
2510  !
2520  !
2530  SUB Meas_current(Current(*),K)
2550    OUTPUT 709;"USE 000"
2551    OUTPUT 709;"CONF DCV"
2552    OUTPUT 709;"NPLC 1"
2553    OUTPUT 709;"RANGE AUTO"
2554    OUTPUT 709;"NRDGS 1"
2555    OUTPUT 709;"DELAY 0.01"
2556    OUTPUT 709;"MEAS DCV,200"
2620    ENTER 709;Vshunt
2640    Curr=Vshunt/.01
2650    Current(K)=ABS(Curr)
2660  SUBEND
2670  !
2680  !
2690  SUB
Store_data1(Qq(*),Tbr2(*),Tsr2(*),Tbulk1(*),Tbulk2(*),Press(*),Area,Chf,K,Data1$,Tetime)
2691  !
2692  ! ~.DAT
2693  ! This file cotains all of the raw steady-state data.
2694  !
2700    MASS STORAGE IS "\USERS\JOO\OUTPUT"
2710    CREATE Data1$,200
2720    ASSIGN @File TO Data1$;FORMAT ON
2730  !
2740    OUTPUT @File USING """File Name,"",17A";Data1$
2750    OUTPUT @File USING """Heater Area [cm^2),"",4D.4D";Area
2760    OUTPUT @File USING """Total Elapsed Time [min],"",7D.3D";Tetime
2770    OUTPUT @File USING """CHF [W/cm^2],"",4D.4D";Chf
2780  !
2790    FOR P=2 TO K-1
2800    OUTPUT @File USING
"4D.2D,"","",4D.2D,"","",4D.2D,"","",4D.2D,"","",4D.2D,"","",4D.4D";Qq(P),Tbr2(P),Tsr2(P
),Tbulk1(P),Tbulk2(P),Press(P)
2810    NEXT P
2820  !
2830    ASSIGN @File TO *
2840  SUBEND
2850  !
```

```
2860  !
2870  SUB
Cal_vinput(Qq(*),Vh(*),Current(*),K,Area,Vinput,Qin,Qin_nat,Qin_80,Qin_chf,Q_nat,Q_80)
2880      Qin=Qin_nat
2890    IF Qq(K)>Q_nat THEN
2900      Qin=Qin_80
2910    END IF
2920    IF Qq(K)>Q_80 THEN
2930      Qin=Qin_chf
2940    END IF
2950    OUTPUT 705;"VOUT ?"
2960    ENTER 705;Vout
2970    Vout=ABS(Vout)
2980    Vinput=SQR((Qq(K)+Qin)*Area*(Vh(K)/Current(K)))+(Vout-Vh(K))
2990  SUBEND
3000  !
3010  !
3020  SUB Graph_frame(Xu,Yu,Xt,Yt)
3030  CLEAR SCREEN
3040  X$="Superheat [Deg C]"
3050  Y$="Heat Flux [W/cm^2]"
3060  Xl=0
3070  Yl=0
3080  Xn=5
3090  Yn=5
3100  GINIT
3110  GRAPHICS ON
3120  PEN 5
3130  CSIZE 5
3140  MOVE 15,92
3150  LABEL "BOILING CURVE OF HEATER"
3160  PEN 1
3170  DEG
3180  LDIR 90
3190  MOVE 15,35
3200  LABEL Y$
3210  LDIR 0
3220  MOVE 47,20
3230  LABEL X$
3240  CSIZE 3
3250  MOVE 19,29
3260  LABEL "0.0"
3270  MOVE 17,58
3280  LABEL Yu/2
3290  MOVE 18,88
3300  LABEL Yu
3310  MOVE 23,26
3320  LABEL "0.0"
3330  MOVE 67,26
3340  LABEL Xu/2
3350  MOVE 112,26
3360  LABEL Xu
3370  VIEWPORT 25,115,30,90
3380  FRAME
3390  WINDOW Xl,Xu,Yl,Yu
3400  AXES Xt,Yt,Xl,Yl,Xn,Yn,5
3410  SUBEND
3420  !
3430  !
3440  SUB Bulk_temp(Tbulk1(*),Tbulk2(*),K)
3460    OUTPUT 709;"USE 000"
3470    OUTPUT 709;"CONF TEMPT"
3480    OUTPUT 709;"NPLC 1"
3490    OUTPUT 709;"NRDGS 1"
3500    OUTPUT 709;"DELAY 0.01"
3510    OUTPUT 709;"MEAS TEMPT,114,117"
3520    ENTER 709;Temp1,Temp2
```

```
3530   Tbulk1(K)=Temp1
3540   Tbulk2(K)=Temp2
3550 SUBEND
3560 !
3570 !
3580 SUB Chf_check(Tbr(*),Tsr(*),J,Tbr2(*),Tsr2(*),Qq(*),K,Delt,Q_80,Chf,Flag1$)
3590   IF Qq(K-1)<Q_80 THEN
3600      GOTO 3740
3610   END IF
3620   H=K-1
3630   IF (Tsr(J)-Tsr2(H))>Delt OR (Tbr(J)-Tbr2(H))>Delt THEN
3640      OUTPUT 705;"CLR"
3650         Chf=Qq(K-1)+(Qq(K-1)-Qq(K-2))/2.0
3660      Flag1$="RED"
3670      BEEP
3680      BEEP
3690      BEEP
3700      BEEP
3710      BEEP
3720      PRINT "!!!!!   CHF   !!!!!"
3730   END IF
3740 SUBEND
3750 !
3760 !
3770 SUB Store_data2(Tbr(*),Tsr(*),Vh(*),Current(*),Data2$,K,J)
3771 !
3772 ! ~.TRS
3773 ! This file contains the last instantaneous heater temperatures
3774 ! at CHF as well as steady-state voltage and resistance data.
3776 !
3780   MASS STORAGE IS "\USERS\JOO\OUTPUT"
3790   CREATE Data2$,200
3800   ASSIGN @File TO Data2$;FORMAT ON
3810 !
3820   FOR I=1 TO J
3830   OUTPUT @File USING "4D.2D,"","",1X,4D.2D";Tbr(I),Tsr(I)
3840   NEXT I
3850 !
3860   FOR J=2 TO K-1
3870   OUTPUT @File USING "4D.4D,"","",3X,4D.4D";Vh(J),Vh(J)/Current(J)
3880   NEXT J
3890   ASSIGN @File TO *
3900 SUBEND
3910 !
3920 !
3930 SUB Meas_press(Press(*),K)
3950   OUTPUT 709;"USE 000"
3960   OUTPUT 709;"CONF DCV"
3970   OUTPUT 709;"NPLC 1"
3980   OUTPUT 709;"RANGE AUTO"
3990   OUTPUT 709;"NRDGS 1"
4000   OUTPUT 709;"DELAY 0.01"
4010   OUTPUT 709;"MEAS DCV,204,203"
4020   ENTER 709;Volt1,Volt2
4030   Vpress=ABS(Volt1)
4040   Vpower=ABS(Volt2)
4041 ! Line for PX602-200AV (0-200 psia) in kPa absolute
4042 ! Press(K)=Vpress*100/Vpower*200*6.894757
4043 ! Line for Omega PX603-060G5V (0-60 psig) in kPa gauge
4044 ! Press(K)=(Vpress-1)/4*60*6.894757
4045 ! Line for Omega PX302-050AV (0-50 psia) in kPa absolute
4046   Press(K)=Vpress*100/Vpower*50*6.894757
4060 SUBEND
4070 !
4080 !
4090 SUB Bulk_stability
4100  INTEGER I,Btn
```

```
4110   REAL Dstrip(1:5)
4120   DIM P$[40]
4130   ON KEY 6 LABEL "STOP" GOTO Finis
4140   ON ERROR GOTO Finis
4150   !
4160   !  INPUT GRAPH HARD POINTS
4170   !
4180   P$="Enter expected Y-axis lower limit :"
4190   DIALOG "NUMBER",P$,Btn;SET ("TITLE":" BULK TEMP $ PRESS STABILITY"),RETURN
("VALUE":X1)
4200   SELECT Btn
4210   CASE 0
4220     Yori=X1
4230   CASE 1
4240     DISP "Numeric input canceled"
4250     GOTO Finis
4260   END SELECT
4270   !
4280   P$="Enter expected Y-axis height :"
4290   DIALOG "NUMBER",P$,Btn;SET ("TITLE":" BULK TEMP & PRESS STABILITY"),RETURN
("VALUE":X2)
4300   SELECT Btn
4310   CASE 0
4320     Yran=X2
4330   CASE 1
4340     DISP "Numeric input canceled"
4350     GOTO Finis
4360   END SELECT
4370   !
4380   P$="Enter monitoring period [minutes] :"
4390   DIALOG "NUMBER",P$,Btn;SET ("TITLE":" BULK TEMP & PRESS STABILITY"),RETURN
("VALUE":X3)
4400   SELECT Btn
4410   CASE 0
4420     Xran=X3
4430     Xran=Xran*60.
4440   CASE 1
4450     DISP "Numeric input canceled"
4460     GOTO Finis
4470   END SELECT
4480   !
4490   !  GENERATE BAR WIDGET
4500   !
4510   ASSIGN @Bars TO WIDGET "BARS";SET ("VISIBLE":0)
4520   CONTROL @Bars;SET ("SHOW LIMITS":0,"SHOW LABELS":0)
4530   CONTROL @Bars;SET ("TITLE":"TEMPERATURE DISPLAY - PRESS F6 TO STOP")
4540   CONTROL @Bars;SET ("X":200,"Y":400,"HEIGHT":100,"WIDTH":400)
4550   CONTROL @Bars;SET ("SYSTEM MENU":"Quit")
4560   CONTROL @Bars;SET ("BAR COUNT":5)
4570   CONTROL @Bars;SET ("CURRENT BAR":1)
4580   CONTROL @Bars;SET ("BAR LABEL":"HEATER 1")
4590   CONTROL @Bars;SET ("CURRENT BAR":2)
4600   CONTROL @Bars;SET ("BAR LABEL":"HEATER 2")
4610   CONTROL @Bars;SET ("CURRENT BAR":3)
4620   CONTROL @Bars;SET ("BAR LABEL":"BULK 1")
4630   CONTROL @Bars;SET ("CURRENT BAR":4)
4640   CONTROL @Bars;SET ("BAR LABEL":"BULK 2")
4650   CONTROL @Bars;SET ("CURRENT BAR":5)
4660   CONTROL @Bars;SET ("BAR LABEL":"PRESSURE","VISIBLE":1)
4670   CONTROL @Bars;SET ("SYSTEM MENU":"Quit")
4680   ON EVENT @Bars,"SYSTEM MENU" GOTO Finis
4690   !
4700   !  GENERATE STRIP-CHART WIDGET
4710   !
4720   ASSIGN @Graph TO WIDGET "STRIPCHART";SET ("VISIBLE":0)
4730   CONTROL @Graph;SET ("SHOW GRID":1,"GRID PEN":0)
4740   CONTROL @Graph;SET ("TITLE":" BULK TEMPERATURE STABILITY - PRESS F6 TO STOP")
```

```
4750   CONTROL @Graph;SET ("X":0,"Y":3,"WIDTH":792,"HEIGHT":450)
4760   CONTROL @Graph;SET ("CURRENT AXIS":"X","ORIGIN":0,"RANGE":Xran)
4770   CONTROL @Graph;SET ("NUMBER FORMAT":"MINUTES","DIGITS":7)
4780   CONTROL @Graph;SET ("AXIS LABEL":"TIME  [minutes]")
4790   CONTROL @Graph;SET ("CURRENT AXIS":"Y","ORIGIN":Yori)
4800   CONTROL @Graph;SET ("RANGE":Yran)
4810   CONTROL @Graph;SET ("AXIS LABEL":"TEMPERATURE  [deg C]")
4820   CONTROL @Graph;SET ("TRACE COUNT":5)
4830   CONTROL @Graph;SET ("CURRENT TRACE":1)
4840   CONTROL @Graph;SET ("TRACE PEN":7,"TRACE LABEL":"HEATER 1")
4850   CONTROL @Graph;SET ("CURRENT TRACE":2)
4860   CONTROL @Graph;SET ("TRACE PEN":2,"TRACE LABEL":"HEATER 2")
4870   CONTROL @Graph;SET ("CURRENT TRACE":3)
4880   CONTROL @Graph;SET ("TRACE PEN":3,"TRACE LABEL":"BULK 1")
4890   CONTROL @Graph;SET ("CURRENT TRACE":4)
4900   CONTROL @Graph;SET ("TRACE PEN":4,"TRACE LABEL":"BULK 2")
4910   CONTROL @Graph;SET ("CURRENT TRACE":5)
4920   CONTROL @Graph;SET ("TRACE PEN":5,"TRACE LABEL":"PRESSURE")
4930   CONTROL @Graph;SET ("CURRENT TRACE":0,"POINT CAPACITY":0,"VISIBLE":1)
4940   CONTROL @Graph;SET ("SYSTEM MENU":"Quit")
4950   ON EVENT @Graph,"SYSTEM MENU" GOTO Finis
4960   !
4970   !  MEASURE TEMPERATURES
4980   !
4990       OUTPUT 709;"RST"
4991       OUTPUT 709;"DISP OFF"
4992       OUTPUT 709;"USE 000"
4993       OUTPUT 709;"CONF TEMPT"
4994       OUTPUT 709;"NPLC 1"
4995       OUTPUT 709;"NRDGS 1"
4996       OUTPUT 709;"DELAY 0.01"
4997       OUTPUT 709;"CLOSE 300,304-306"
4998  Start=TIMEDATE
4999  !
5000  ! Uncomment these two lines to allow power to heater 1
5001  !OUTPUT 709;"OPEN 302"
5002  !OUTPUT 709;"CLOSE 301"
5003  ! Uncomment these two lines to allow power to heater 2
5004  !OUTPUT 709;"OPEN 301"
5005  !OUTPUT 709;"CLOSE 302"
5006  !
5007  WHILE 1
5008    T=TIMEDATE-Start
5009      OUTPUT 709;"MEAS TEMPT,110,111,114,117"
5010      ENTER 709;Dstrip(1),Dstrip(2),Dstrip(3),Dstrip(4)
5011      OUTPUT 709;"MEAS DCV,204,203"
5012      ENTER 709;Dstrip(5),Vpower
5013  ! Line for PX602-200AV (0-200 psia) in kPa absolute
5014  ! Dstrip(5)=ABS(Dstrip(5))*100/ABS(Vpower)*200*6.894757
5015  ! Line for Omega PX603-060G5V (0-60 psig) in kPa gauge
5016  ! Dstrip(5)=(ABS(Dstrip(5))-1)/4*60*6.894757
5017  ! Line for Omega PX302-050AV (0-50 psia) in kPa absolute
5018    Dstrip(5)=ABS(Dstrip(5))*100/ABS(Vpower)*50*6.894757
5019  !
5020  !  PLOT AND DISPLAY THE MEASURED TEMPERATURES AND PRESSURE
5021  !
5022    CONTROL @Graph;SET ("POINT LOCATION":T,"VALUES":Dstrip(*))
5023    CONTROL @Bars;SET ("VALUES":Dstrip(*))
5024  !
5031  END WHILE
5280 Finis:  !
5300  P$="Do you want to exit to main program ?"
5310  DIALOG "QUESTION",P$,Btn
5320  IF Btn=0 THEN GOTO 5340
5330  IF Btn=1 THEN GOTO 5008
5340  ASSIGN @Graph TO *  ! Delete STRIPCHART widget
5350  ASSIGN @Bars TO * ! Delete BARS widget
```

```
5360  OUTPUT 709;"RST"
5370  SUBEND
5380  !
5390  !
5400  SUB Store_data3(Qq(*),Tbr2(*),Tsr2(*),Tbulk1(*),Tbulk2(*),K,Pre$,Dx,Cond)
5401  !
5402  ! ~.-
5404  ! This data file contains heat flux and corrected Twall-Tbulk data for plotting
5410  !
5420    MASS STORAGE IS "\USERS\JOO\OUTPUT"
5430    CREATE Pre$,200
5440    ASSIGN @File TO Pre$;FORMAT ON
5450  !
5470    Dx=Dx/1000
5480    FOR P=2 TO K-1
5490      Tbul=Tbulk1(P)+Qq(P)*10000/Cond*Dx
5491      T1=Tbr2(P)-Tbul
5492      T2=Tsr2(P)-Tbul
5493      Tavg=(T1+T2)/2
5500      OUTPUT @File USING "3D.3D,3("","",3D.2D)";Qq(P),T1,T2,Tavg
5510    NEXT P
5520  !
5530    ASSIGN @File TO *
5540  SUBEND
5550  !
5560  !
5570  SUB Store_data4(Ttime(*),Tbr1(*),Tsr1(*),N,Data3$)
5571  !
5572  ! ~.HIS
5574  ! This file contains the raw steady-state heater temperatures and elapsed time
5580  !
5590    MASS STORAGE IS "\USERS\JOO\OUTPUT"
5600    CREATE Data3$,200
5610    ASSIGN @File TO Data3$;FORMAT ON
5620  !
5630    FOR P=1 TO N
5640    OUTPUT @File USING "8D.2D,"","",4D.2D,"","",4D.2D";Ttime(P),Tbr1(P),Tsr1(P)
5650    NEXT P
5660  !
5670    ASSIGN @File TO *
5680  SUBEND
5690  !
5700  SUB Main(Pre$,Hsw)
5711  !
5717  !--------------- INPUT LIST ---------------------------------!
5727  !
5737    Area=1.0              ! Heating Area [cm^2]
5738    Dx=1.0                ! Distance from T/C to surface [mm]
5739    Cond=400              ! Therm. Cond. of heater [W/m-K]
5747    Tinterval=0.          ! Interval Waiting Time [sec]
5757    Nm1=125.              ! Number of Measurement
5767    Nm2=125.
5777    Delt=20.              ! CHF Check For Temp. Jump
5787    Tol_nat=.2            ! Check at Natural Conv.
5797    Tol_chf=.2            ! Check at Boiling Region
5807    Vinput=.1             ! Initial Voltage
5817    Q_nat=3.0             ! Natural Convection Criterion
5827    Q_80=60.              ! 80% of CHF
5837    Q_90=70.              ! 90% of CHF
5847    Ngo_80=2
5857    Ngo_90=4
5867    Ngo_chf=4
5877    Qin_nat=.3            ! Heat Flux Increment at Q < Qnat
5887    Qin_80=2.             ! Qnat < Q < Qchk
5897    Qin_chf=1.5           ! Qchk < Q
5898    Tmax1=110             ! Maximum instantaneous heater temperature
5899    Tmax2=100             ! Maximum steady-state heater temperature
```

```
5907    Chf=0.
5917    Xu=50.                ! Maximum Temp. Value at X-Axis
5927    Yu=15.                ! Maximum Q Value at Y-Axis
5937    Xt=5
5947    Yt=1
5957    F1$=".DAT"
5967    F2$=".TRS"
5977    F3$=".HIS"
5987  ! INPUT "ENTER OUTPUT FILE NAME ? ",Pre$
5997    Data1$=Pre$&F1$       ! Output Data File Name
6007    Data2$=Pre$&F2$       ! Transient Data at CHF
6017    Data3$=Pre$&F3$       ! Whole Transient Data
6027  !
6037  !------------ END OF INPUT -----------------------------------!
6047  !
6057  Tcount1=TIMEDATE
6067  !
6077    CALL Graph_frame(Xu,Yu,Xt,Yt)
6087  !
6097    DIM Qq(1:500),Tbulk1(1:500),Tbulk2(1:500)
6107    DIM Tbr(1:500),Tsr(1:500),Tur(1:500),Tbr2(1:500),Tsr2(1:500),Tur2(1:500)
6117    DIM Vh(1:500),Current(1:500),Press(1:500),Time_temp(1:500)
6127    DIM Tbr1(1:3000),Tsr1(1:3000),Ttime(1:3000)
6137    DIM Tbi(1:500),Tsi(1:500),Tui(1:500)
6147  !
6157    PRINT "PRESS F1 TO SHUT OFF THE POWER"
6167    ON KEY 1 GOTO Exit
6177    ON ERROR GOTO Exit
6187  !
6197    OUTPUT 709;"RST"
6207    OUTPUT 709;"DISP OFF"
6217    OUTPUT 709;"CLOSE 304-306"
6237    OUTPUT 705;"CLR"
6238  !
6247  ! Open/Close appropriate power lines depending on which heater is tested
6248      SELECT Hsw
6249      CASE 1
6250        OUTPUT 709;"OPEN 303"
6251        OUTPUT 709;"CLOSE 302"
6252  !     Q_80=18.
6253  !     Q_90=20.
6254  !     Dx=1.0
6256  !     Qin_nat=.2
6257  !     Qin_80=1.
6258  !     Qin_90=.5
6259      CASE 2
6260        OUTPUT 709;"OPEN 302"
6261        OUTPUT 709;"CLOSE 303"
6262  !     Q_80=45.
6263  !     Q_90=50.
6264  !     Dx=.75
6266  !     Qin_nat=.3
6267  !     Qin_80=2.
6268  !     Qin_90=1.
6269      END SELECT
6270  !
6271    WAIT 3
6272  !
6277    X1=0.
6287    Y1=0.
6297    Z1=0.
6307    W1=0.
6317    A1=0.
6327    B1=0.
6337    C1=0.
6347    N=0
6357  !----------------------------------------------!
```

```
6367  !      START MEASUREMENT
6377  !----------------------------------------------!
6387  Timeswitch1=TIMEDATE
6397    FOR K=2 TO 500
6407    OUTPUT 705;"ISET 7.0"
6417    OUTPUT 705;"VSET";Vinput
6427  !
6437    Ngo=1
6447    Ngochk=Ngo_80
6457    IF Qq(K-1)>Q_80 THEN
6467      Ngochk=Ngo_90
6477    END IF
6487    IF Qq(K-1)>Q_90 THEN
6497      Ngochk=Ngo_chf
6507    END IF
6517  !
6547      OUTPUT 709;"USE 000"
6557      OUTPUT 709;"CONF TEMPT"
6567      OUTPUT 709;"NPLC 0.1"
6577      OUTPUT 709;"NRDGS 1"
6587      OUTPUT 709;"DELAY 0.01"
6597 !
6607    FOR J=1 TO Nm1
6608      SELECT Hsw
6609      CASE 1
6610        OUTPUT 709;"MEAS TEMPT,110,111"
6611      CASE 2
6612        OUTPUT 709;"MEAS TEMPT,112,113"
6613      END SELECT
6627      ENTER 709;Tbr(J),Tsr(J)
6637 ! Check for CHF
6710      IF Qq(K-1)>Q_80 THEN
6712        IF (Tbr(J)-Tbr2(K-1))>Delt OR (Tsr(J)-Tsr2(K-1))>Delt THEN
6713          OUTPUT 705;"CLR"
6714          Chf=Qq(K-1)+(Qq(K-1)-Qq(K-2))/2.0
6715          GOTO Exit
6716        END IF
6717      ELSE
6719        IF Tbr(J)>Tmax1 OR Tsr(J)>Tmax1 THEN
6720          OUTPUT 705;"CLR"
6721          Chf=0
6722          PRINT "Test aborted because of premature CHF"
6723          GOTO Exit
6724        END IF
6726      END IF
6727    NEXT J
6728  Timeswitch2=TIMEDATE
6737  !
6747    N=N+1
6757    Tbr1(N)=SUM(Tbr)/Nm1
6767    Tsr1(N)=SUM(Tsr)/Nm1
6777    Taverage1=(Tbr1(N)+Tsr1(N))/2.0
6787    Ttime(N)=Timeswitch2-Timeswitch1
6797  !
6807       WAIT Tinterval
6817  !
6827    FOR J=1 TO Nm1
6837      SELECT Hsw
6838      CASE 1
6839        OUTPUT 709;"MEAS TEMPT,110,111"
6840      CASE 2
6841        OUTPUT 709;"MEAS TEMPT,112,113"
6842      END SELECT
6847      ENTER 709;Tbr(J),Tsr(J)
6863 ! Check for CHF
6864      IF Qq(K-1)>Q_80 THEN
6865        IF (Tbr(J)-Tbr2(K-1))>Delt OR (Tsr(J)-Tsr2(K-1))>Delt THEN
```

```
6866          OUTPUT 705;"CLR"
6867          Chf=Qq(K-1)+(Qq(K-1)-Qq(K-2))/2.0
6868          GOTO Exit
6869        END IF
6870      ELSE
6872        IF Tbr(J)>Tmax1 OR Tsr(J)>Tmax1 THEN
6873          OUTPUT 705;"CLR"
6874          Chf=0
6875          PRINT "Test aborted because of premature CHF"
6876          GOTO Exit
6877        END IF
6879      END IF
6937    NEXT J
6947  Timeswitch3=TIMEDATE
6957  !
6967    N=N+1
6977    Tbr1(N)=SUM(Tbr)/Nm1
6987    Tsr1(N)=SUM(Tsr)/Nm1
6997    Taverage2=(Tbr1(N)+Tsr1(N))/2.0
7007    Ttime(N)=Timeswitch3-Timeswitch1
7017  !
7027  !--- CONVERGENCE CHECK -----------------------!
7037      Tolerance=Tol_nat
7047    IF Qq(K-1)>Q_nat THEN
7057      Tolerance=Tol_chf
7067    END IF
7077  !
7087    Ngo=Ngo+1
7097    IF Ngo>Ngochk THEN
7107        GOTO 7167
7117    ELSE
7127        Taverage1=Taverage2
7137        GOTO 6807
7147    END IF
7157  !
7167    IF ABS(Taverage1-Taverage2)>Tolerance THEN
7177        Taverage1=Taverage2
7187        GOTO 6807
7197    ELSE
7207        GOTO 7227
7217    END IF
7227    Tbr2(K)=Tbr1(N)
7237    Tsr2(K)=Tsr1(N)
7247  !--- MEASURE BULK TEMP., PRESSURE & HEAT FLUX ----------!
7257    CALL Bulk_temp(Tbulk1(*),Tbulk2(*),K)
7267    CALL Meas_press(Press(*),K)
7277    CALL Meas_volt(Vh(*),K,Hsw)
7287    CALL Meas_current(Current(*),K)
7297    CALL Cal_heatflux(Area,Vh(*),Current(*),Qq(*),K)
7307    Timeswitch3=TIMEDATE
7317    Time_temp(K)=Timeswitch3-Timeswitch1
7327  !
7397    IF Qq(K-1)>Q_80 THEN
7407      Nm1=Nm2
7417      Tinterval=0.
7427      DISP USING "3D.2D,1X,4D.1D,4D.1D,3X,4D.4D";Qq(K),Taverage2,Tbulk1(K),Press(K)
7437      GOTO 7637
7447    END IF
7457  !--- PLOT THE RESULT ------------------------!
7467    Y2=Qq(K)
7477    A2=Tbr2(K)-Tbulk1(K)
7487    B2=Tsr2(K)-Tbulk1(K)
7497    PEN 2
7507    PLOT A1,Y1
7517    PLOT A2,Y2
7527    PENUP
7537    PEN 3
```

```
7547    PLOT B1,Y1
7557    PLOT B2,Y2
7567    PENUP
7577    Y1=Y2
7587    A1=A2
7597    B1=B2
7607  !--- DISPLAY ON SCREEN -------------------------------------!
7617    DISP USING
"3D.2D,1X,4D.1D,4D.1D,4D.1D,3X,3D.4D";Qq(K),Tbr2(K),Tsr2(K),Tbulk1(K),Press(K)
7627  !--- DETERMINE VOLTAGE INPUT AND CHECK VOLTAGE OVERFLOW ----!
7637    CALL
Cal_vinput(Qq(*),Vh(*),Current(*),K,Area,Vinput,Qin,Qin_nat,Qin_80,Qin_chf,Q_nat,Q_80)
7647    IF Vinput>200 THEN
7657      PRINT "!!!!!  NOW, VOLTAGE INPUT EXCEEDS 200 Volts  !!!!! "
7667      GOTO Exit
7677    END IF
7678    IF Vinput<0 THEN
7679      GOTO Exit
7680    END IF
7681  !
7687  ! Check steady-state temperature limit on heater
7688      IF Tbr2(K)>Tmax2 OR Tsr2(K)>Tmax2 THEN
7689        OUTPUT 705;"CLR"
7690        Chf=0
7691        PRINT "Test aborted because heater temperature too high"
7693        GOTO Exit
7694      END IF
7695  !
7697    NEXT K
7707  !------------- END OF THE LOOP ------------------!
7717  !
7727  !
7737  !
7747 Exit:  !
7757  OUTPUT 705;"CLR"
7767  OUTPUT 709;"RST"
7777  !
7787  Tcount2=TIMEDATE
7797  Tetime=(Tcount2-Tcount1)/60.
7807    BEEP
7817    BEEP
7827    BEEP
7837    BEEP
7847    BEEP
7857    PRINT "CRITICAL HEAT FLUX  =  ";Chf
7867    PRINT "TOTAL ELAPSED TIME [MIN]  =  ",Tetime
7877  !
7887  CALL
Store_data1(Qq(*),Tbr2(*),Tsr2(*),Tbulk1(*),Tbulk2(*),Press(*),Area,Chf,K,Data1$,Tetime)
7897  CALL Store_data2(Tbr(*),Tsr(*),Vh(*),Current(*),Data2$,K,J)
7907  CALL Store_data3(Qq(*),Tbr2(*),Tsr2(*),Tbulk1(*),Tbulk2(*),K,Pre$,Dx,Cond)
7917  CALL Store_data4(Ttime(*),Tbr1(*),Tsr1(*),N,Data3$)
7937  SUBEND
7947  !
7957  !
7967  DEF FNTsat(P)
7977    ! This function calculates the saturation temperature for the test fluid
7978    ! T is in deg C, P is in kPa abs.
7987    ! Fluid: FC-72
7997    Tsat=-30.69+23.86*LGT(P)+12.5*LGT(P)^2-5.495*LGT(P)^3+2.736*LGT(P)^4-
.3341*LGT(P)^5
8007    ! Fluid: FC-87
8017    !Tsat=
8027    RETURN Tsat
8037  FNEND
8047  !
8057  !
```

```
8067  DEF FNPsat(T)
8077    ! This function calculates the saturation pressure for the test fluid
8078    ! T is in deg C, P is in kPa abs.
8088    ! Fluid: FC-72
8098    Psat=8.376+.5396*T+8.697E-3*T^2+1.956E-4*T^3-3.106E-7*T^4+4.079E-9*T^5
8108    ! Fluid: FC-87
8118    !Psat=
8128    RETURN Psat
8138  FNEND
```

APPENDIX D

POOL BOILING EXPERIMENTAL DATA

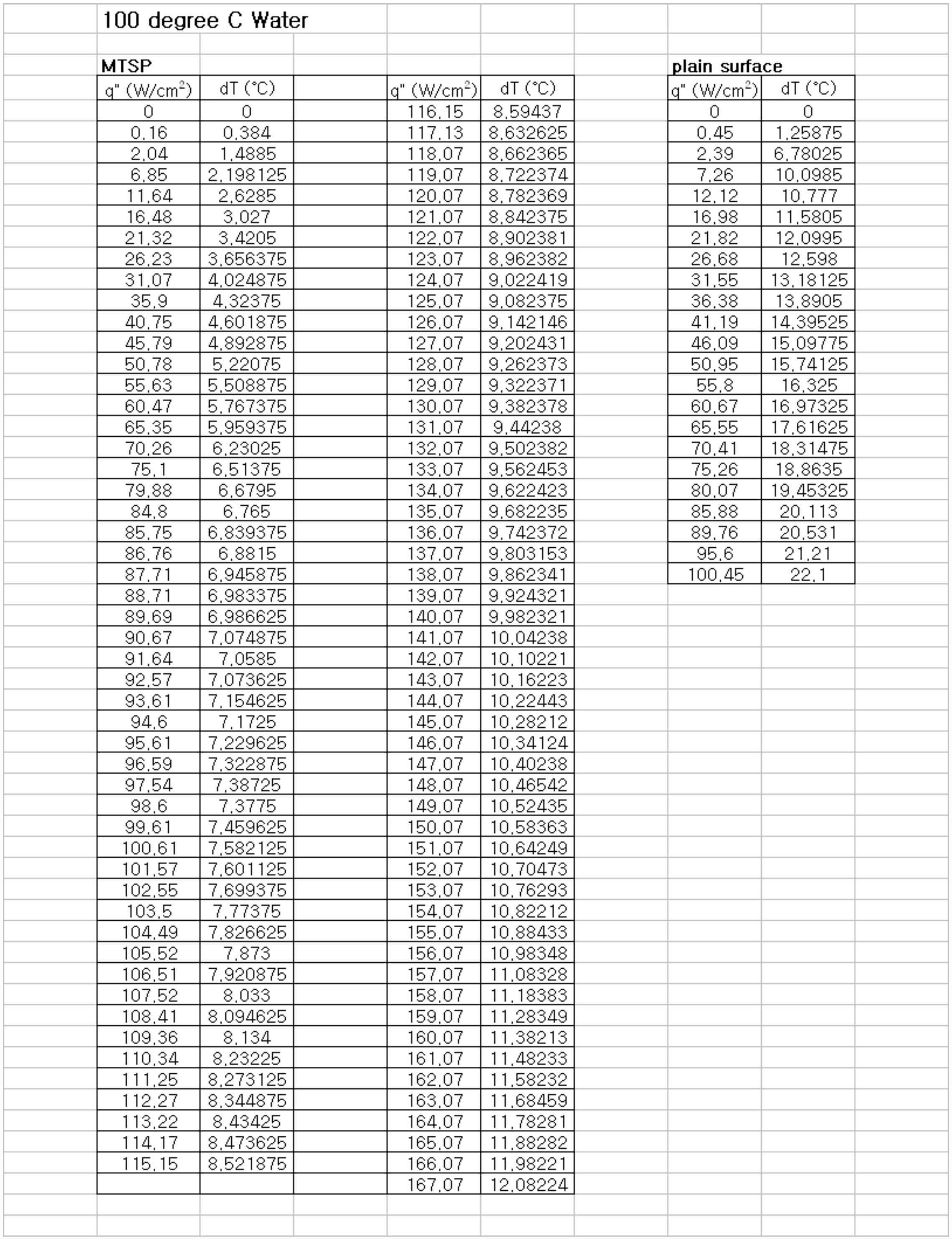

100 degree C Water

MTSP

q" (W/cm^2)	dT (°C)
0	0
0,16	0,384
2,04	1,4885
6,85	2,198125
11,64	2,6285
16,48	3,027
21,32	3,4205
26,23	3,656375
31,07	4,024875
35,9	4,32375
40,75	4,601875
45,79	4,892875
50,78	5,22075
55,63	5,508875
60,47	5,767375
65,35	5,959375
70,26	6,23025
75,1	6,51375
79,88	6,6795
84,8	6,765
85,75	6,839375
86,76	6,8815
87,71	6,945875
88,71	6,983375
89,69	6,986625
90,67	7,074875
91,64	7,0585
92,57	7,073625
93,61	7,154625
94,6	7,1725
95,61	7,229625
96,59	7,322875
97,54	7,38725
98,6	7,3775
99,61	7,459625
100,61	7,582125
101,57	7,601125
102,55	7,699375
103,5	7,77375
104,49	7,826625
105,52	7,873
106,51	7,920875
107,52	8,033
108,41	8,094625
109,36	8,134
110,34	8,23225
111,25	8,273125
112,27	8,344875
113,22	8,43425
114,17	8,473625
115,15	8,521875
116,15	8,59437
117,13	8,632625
118,07	8,662365
119,07	8,722374
120,07	8,782369
121,07	8,842375
122,07	8,902381
123,07	8,962382
124,07	9,022419
125,07	9,082375
126,07	9,142146
127,07	9,202431
128,07	9,262373
129,07	9,322371
130,07	9,382378
131,07	9,44238
132,07	9,502382
133,07	9,562453
134,07	9,622423
135,07	9,682235
136,07	9,742372
137,07	9,803153
138,07	9,862341
139,07	9,924321
140,07	9,982321
141,07	10,04238
142,07	10,10221
143,07	10,16223
144,07	10,22443
145,07	10,28212
146,07	10,34124
147,07	10,40238
148,07	10,46542
149,07	10,52435
150,07	10,58363
151,07	10,64249
152,07	10,70473
153,07	10,76293
154,07	10,82212
155,07	10,88433
156,07	10,98348
157,07	11,08328
158,07	11,18383
159,07	11,28349
160,07	11,38213
161,07	11,48233
162,07	11,58232
163,07	11,68459
164,07	11,78281
165,07	11,88282
166,07	11,98221
167,07	12,08224

plain surface

q" (W/cm^2)	dT (°C)
0	0
0,45	1,25875
2,39	6,78025
7,26	10,0985
12,12	10,777
16,98	11,5805
21,82	12,0995
26,68	12,598
31,55	13,18125
36,38	13,8905
41,19	14,39525
46,09	15,09775
50,95	15,74125
55,8	16,325
60,67	16,97325
65,55	17,61625
70,41	18,31475
75,26	18,8635
80,07	19,45325
85,88	20,113
89,76	20,531
95,6	21,21
100,45	22,1

60 degree C Water

MTSP

q" (W/cm^2)	dT (°C)
0	0
0,02	0,5195
1,01	3,08975
1,99	4,20025
2,96	4,726
5,39	5,39025
7,79	5,91025
10,24	6,369
12,66	6,8685
15,09	7,18275
17,52	7,547
19,94	7,9215
22,36	8,316
24,79	8,58025
27,22	8,9895
29,64	9,364
32,09	9,67775
33,06	9,8135
34,04	9,879
35,03	9,97425
35,99	10,11025
36,95	10,05625
37,93	10,21675
38,86	10,2985
39,81	10,23975
40,83	10,41425
41,77	10,37075
42,79	10,29525
43,79	10,46525
44,79	10,44025
45,88	10,578
46,86	10,6085
47,86	10,6835
48,87	10,75825
49,84	10,894
50,82	11,0145
51,79	11,00525
52,79	11,01525
53,77	11,00575
54,74	10,9515
55,71	10,93725
56,68	10,843
57,63	11,07425
58,57	11,10075
59,57	11,21575
60,55	11,31125
61,54	11,3515
62,52	11,427
63,51	11,48225
64,49	11,61275
65,47	11,84325
66,42	11,8795
67,39	11,97025
68,37	12,20075
69,36	12,196
70,34	12,1915
71,32	12,247
72,31	12,31725
73,31	12,36725
74,25	12,44375
75,19	12,53525
76,16	12,746
77,13	12,82675
78,07	12,95825
79,07	13,11325
80,04	13,379
81,01	13,33475
82	13,265
83	13,42
83,95	13,39625
84,89	13,49775
85,82	13,6645
86,77	13,74075
87,73	13,62675
88,68	13,768
89,67	13,93825
90,65	14,00375
91,61	13,91475
92,62	14,1795
93,63	14,11925
94,55	14,31625
95,48	14,398
96,43	14,53925
97,35	14,62625
98,35	14,74125
99,31	14,55725
100,29	14,71775
101,28	14,873
102,23	14,92425
103,21	14,88975
104,18	15,1055
105,19	15,29525
106,21	15,61475
107,22	15,4645
108,16	15,441
109,11	15,70225
110,04	15,689
111,05	15,73875
112,02	15,9745
112,98	15,7955
113,9	16,0525
114,91	16,10225
115,87	16,10325
116,84	16,194
117,84	16,079
118,84	16,479
119,8	16,59
120,83	16,75925
121,85	16,90375
122,87	17,16825
123,82	17,3495
124,82	17,4745
125,77	17,76075
126,72	17,927
127,67	18,03325
128,58	18,1555
129,58	18,4805
130,52	18,922
131,53	19,07675
132,46	19,3785
133,41	19,78475
134,37	20,08575

plain surface

q" (W/cm^2)	dT (°C)
0	0
0,77	6,08575
2,7	12,0325
5,12	13,752
7,55	15,64125
9,96	15,506
12,4	14,955
14,82	15,4395
17,23	16,22425
19,66	16,2485
22,09	17,17275
24,49	17,80275
26,95	18,65625
29,36	19,421
31,75	19,75125
34,17	20,31075
36,61	20,87475
39,05	21,16375
41,45	21,98875
42,41	22,11975
43,4	22,115
44,41	22,13975
45,37	22,31575
46,35	22,76125
47,32	22,897
48,33	23,32675
49,27	22,73825
50,26	24,0285
51,23	24,32425
52,21	24,58475
53,21	24,66975
54,15	24,87125
55,11	24,96225
56,07	25,06325
57,04	25,114
58,05	25,23375
59,05	25,68875
60,01	26,00475
60,96	26,201
61,94	26,1465
62,92	26,262
63,88	26,523
64,86	26,6735
65,8	27,075
66,68	27,253
67,6	27,435
68,49	28,11775
69,49	28,31275
70,47	28,74325
71,46	29,1635
72,4	29,29
73,43	29,19425
74,37	29,36575
75,34	30,0065
76,35	30,65625

REFERENCES

[1] Nukiyama, S., 1934, "The Maximum and Minimum Values of the Heat Q Transmitted from Metal to Boiling Water under Atmospheric Pressure," *International Journal of Heat and Mass Transfer*, Vol. 9, pp. 1419-1433.

[2] Kutateladze, S. S., 1952, Heat Transfer in Condensation and Boiling, USAEC Rep.

[3] Rohsenow, W. M., 1962, "A Method of Correlating Heat Transfer Data for Surface Boiling of Liquids," *ASME Journal of Heat Transfer*, Vol. 74, pp. 969-975.

[4] Kuehn, T. H. and Goldstein, R. J., 1976, "Correlating Equations for Natural Convection Heat Transfer between Horizontal Circular Cylinders," *International Journal of Heat and Mass Transfer*, Vol. 19, pp. 1127-1134.

[5] Goldstein, R. J., Sparrow, E. M., and Jones, D. C., 1973, "Natural Convection Mass Transfer Adjacent to Horizontal Plates," *International Journal of Heat and Mass Transfer*, Vol. 16, pp. 1025.

[6] Griffith, P. and Wallis, J. D., 1959, "The Role of Surface Conditions in Nucleate Boiling," *Chemical Engr. Progress Symposium Series*, Vol. 56, No. 30, pp. 49-63.

[7] Bar-Cohen, A. and Simon, T. W., 1988, "Wall Superheat Excursions in the Boiling Incipience of Dielectric Fluids," *Heat Transfer Engr*. Vol.9:1, pp. 19-31.

[8] Rohsenow, W. M., 1962, "A Method of Correlating Heat Transfer Data for Surface Boiling of Liquids," *Journal of Heat Transfer*, Vol. 84, pp. 969-975.

[9] Lienhard, J. H., 1981, “A Heat Transfer Textbook,” *Prentice Hall, Inc*., Englewood Cliffs, New Jersey.

[10] Zuber, N., 1959, “Hydrodynamic Aspects of Boiling Heat Transfer,” AEC Report No. AECU-4439, Physics and Mathematics.

[11] Kutateladze, S. S., 1948, “On the Transition to Film Boiling Under Natural Convection,” *Kotloturbostroenie*, No. 3, pp. 10.

[12] Lienhard, J. H. and Dhir, V. K., 1973, “Hydrodynamic Prediction of Peak Pool Boiling Heat Fluxes from Finite Bodies,” *Journal of Heat Transfer*, pp. 152-158.

[13] Kurihara, H. M. and Myers, J. E., 1960, “The Effects of Superheat and Surface Roughness on Boiling Coefficients,” *AIChE Journal*, Vol. 6, No. 1, pp. 83-91.

[14] Berenson, P. J., 1962, “Experiments on Pool-Boiling Heat Transfer,” *International Journal of Heat and Mass Transfer*, Vol. 5, pp. 985-999.

[15] Nishio, S., and Chandratilleke, G. R., 1989, “Steady-State Pool Boiling Heat Transfer to Saturated Liquid Helium at Atmospheric Pressure,” *JSME International Journal. Series II*, Vol. 32, No. 4, pp. 639-645.

[16] Ramilison, J. M., Sadasivan, P., and Lienhard, J. H., 1992, “Surface Factors Influencing Burnout on Flat Heaters,” *Journal of Heat Transfer*, Vol. 114, No. 1, pp. 287-290.

[17] Polezhaev, Y. V., and Kovalev, S. A., 1990, “Modeling Heat Transfer with Boiling on Porous Structures,” *Thermal Engineering*, Vol. 37, No. 12, pp. 617-620.

[18] Tehver, J., 1992, “Influences of Porous Coating on the Boiling Burnout Heat Flux,” *Recent Advances in Heat Transfer*, pp. 231-242.

[19] Griffith, P. and Wallis, J. D., 1960, “The Role of Surface Conditions in Nucleate Boiling,” *Chemical Engineering Progress Symposium Series No. 49*, Vol. 56, pp. 49-63.

[20] Thome, J. R., 1992, “Mechanisms of Enhanced Nucleate Pool Boiling,” *Proceedings of the Engineering Foundation Conference on Pool and External Flow Boiling*, ASME, New York, pp. 337-343.

[21] O'Connor, J. P., and You, S. M., 1995, “A Painting Technique to Enhance Pool Boiling Heat Transfer in FC-72,” *Journal of Heat Transfer*, Vol. 117, No. 2, pp. 387-393.

[22] Chang, J. Y., and You, S. M., 1997, “Boiling Heat Transfer Phenomena From Microporous and Porous Surfaces in Saturated FC-72,” *International Journal of Heat and Mass Transfer*, Vol. 40, No. 18, pp. 4437-4447.

[23] Chang, J. Y., and You, S. M., 1997, “Enhanced Boiling Heat Transfer From Microporous Surfaces: Effects of a Coating Composition and Method,” *International Journal of Heat and Mass Transfer*, Vol. 40, No. 18, pp. 4449-4460.

[24] You, S. M. and O’Connor, J. P., 1998, “Boiling Enhancement Paint,” U. S. Patent #5814392.

[25] Chang, J. Y. and You, S. M., 1997, "Enhanced Boiling Heat Transfer from Micro-Porous Cylindrical Surfaces in Saturated FC-87 and R-123," *Journal of Heat Transfer*, Vol. 119, No. 2, pp. 319-325.

[26] Rainey, K.N. and You, S. M., 2001, "Effects of Heater Orientation on Pool Boiling Heat Transfer from Microporous Coated Surfaces," *International Journal of Heat and Mass Transfer*, Vol. 44, No. 14, pp. 2589-2599.

[27] Kim, J. H., Rainey, K. N., You, S. M., and Park, J. Y., 2002, "Mechanism of Nucleate Boiling Heat Transfer Enhancement From Microporous Surfaces in Saturated FC-72," *Journal of Heat Transfer*, Vol. 124, No. 3, pp. 500-506.

[28] Ammerman, C.N., and You, S.M., 1998, "Consecutive-Photo Method to Measure Vapor Volume Flow Rate During Boiling From a Wire Immersed in Saturated Liquid," *Journal of Heat Transfer*, Vol. 120, pp. 561-567.

[29] Lunde, K. and Perkins, R.J., 1995, "A Method for the Detailed study of Bubble Motion and Deformation," *Proceedings of the 2nd International Conference on Multiphase Flow*, Kyoto, pp. 395–405.

[30] Kline, S.J., and McClintock, F.A., 1953, "Describing Uncertainties in Single-Sample Experiments," *Mechanical Engineering*, Vol. 75, No. 1, pp. 3-8.

[31] Rainey, K. N. and You, S. M., 2000, "Pool Boiling Heat Transfer From Plain and Microporous, Square Pin Finned Surfaces in Saturated FC-72," *Journal of Heat Transfer*, Vol. 122, No. 3, pp. 509-516.

[32] Rainey, K.N., Li, G., and You, S.M., 2001, "Flow Boiling Heat Transfer From Plain and Microporous Coated Surfaces in Subcooled FC-72," ASME Journal of Heat Transfer, 123, No.5, pp. 918-925.

[33] Bliss, F. E., Hsu, S. T., and Crawford, M., 1969, "An Investigation into the Effects of Various Platings on the Film Coefficient During Nucleate Boiling from Horizontal Tubes," *International Journal of Heat and Mass Transfer*, Vol. 1, pp.. 1061-1072.

[34] Albertson, C. E., 1977, "Boiling Heat Transfer Surface and Method," U.S. Patent 4,018,264.

[35] You, S. M., Simon, T. W., and Bar-Cohen, A., 1990, "Experiments on Boiling Incipience with a Highly-Wetting Dielectric Fluid: Effects of Pressure, Subcooling and Dissolved Gas Content," *Heat Transfer, Proceedings of the International Heat Transfer Conference*, Hemisphere, New York, pp. 337-342.

[36] Nishikawa, K., Fujita, Y., Ohta, H., and Hidaka, S., 1982, "Effects of System Pressure and Surface Roughness on Nucleate Boiling Heat Transfer," *Memoirs of the Faculty of Engineering, Kyushu University*, Vol. 42, No. 2, pp. 95-111.

[37] Choi, U.S., Zhang, Z. G.., Yu, W., Lockwood, F. E. and Grulke, E. A., 2001, "Anomalous Thermal Conductivity Enhancement in Nanotube Suspensions," *Applied Physics Letters*, 79, 2252.

[38] Eastman, J., Choi, U.S., Li, S., Yu, W. and Thompson, L. J., 2001, "Anomalously Increased Effective Thermal Conductivities of Ethylene glycol-based nanofluids containing copper nanoparticles", *Applied Physics Letters* , 78, 718.

[39] You, S. M., Kim, J. H. and Kim, K. H., 2003, "Effect of nanoparticles on critical heat flux of water in pool boiling heat transfer," *Applied Physics Letters*, 83, 3374.

[40] Vassallo, P., Kumar, R. and D'Amico, S., 2003, "Pool boiling heat transfer experiments in silica-water nano-fluids," *International Journal of Heat and Mass Transfer*, 47, pp. 407-411.

[41] Frea, W. J., Knapp, R., and Taggart, T. D., 1977, "Flow Boiling and Pool Boiling Critical Heat Flux in Water and Ethylene Glycol Mixtures." *Canadian Journal of Chemical Engineering*, 55(1), 37-42.

[42] Van Weijk, W. R., Vos, A. S., and Van Stralen, S. J. D., 1956, Chemical Engineering Science, 66(5).

BIOGRAPHICAL INFORMATION

Joo Han Kim received his B.S and M.S in Mechanical Engineering at the University of Texas at Arlington, Arlington Texas in May 1998 and August 2001. He has worked as a full time graduate student in the Micro-Scale Heat Transfer Laboratory at the University of Texas at Arlington under Dr. Seung-Mun You since September 1998, focusing on enhancement of pool boiling heat transfer by microporous coating techniques with applications to microelectronics cooling.

Since March of 2001 he has worked as a visiting scholar for Seoul National University for six months, involved in analyzing the mechanism of pool boiling heat transfer and microporous coating design. Then, he started his Ph.D program January 2002 at the University of Texas at Arlington under Dr. Seung Mun You. Mainly involved in boiling heat transfer in electronic cooling applications, his study has a broad range of areas associated with electronic cooling technologies. Joo Han received his Ph.D. on Mechanical Engineering at the University of Texas at Arlington in December 2006.